bcrs-89-24

progress report on the VIERS-1 project part-1: the Delft wind/wave experiment

experiment and first results

D. van Halsema
Ch. Calkoen
B. Jaehne
W.A. Oost
P. Snoeij
S. Waas

bcrs
Netherlands remote sensing board

progress report on the VIERS-1 project
part-1: the Delft wind/wave experiment

experiment and first results

drs. D. van Halsema
— Physics and Electronics Lab. TNO
dr. Ch. Calkoen
— Delft Hydraulics
dr. B. Jaehne
— SCRIPPS Institution of Oceanography
(on leave from Heidelberg University)
dr. W.A. Oost
— Royal Netherlands Meteorological Institute
ir. P. Snoeij
— Delft University of Technology
S. Waas
— Heidelberg University

bcrs report no. 89-24
project progress report AO-1.3

November 1989

This research is being carried out supported by the Netherlands remote sensing board (bcrs)
The cooperation with the Institute for Environmental Physics, Heidelberg University was made possible by a twinning grant from the European Community (contractno. ST2J-0451-C (GDF)

ABSTRACT/EXECUTIVE SUMMARY

This report describes the Delft wind/wave experiment of the VIERS-1 program, conducted in November 1987 and March 1988. After an introduction in chapter 1, chapter 2 pays attention to the equipment and measurement procedures used and the experimental program is discussed. Chapter 3 deals with the processing of the data and a discussion of the first results. Finally chapter 4 deals with the future processing of the data and contains the concluding remarks.

An important practical environmental problem is to obtain operational information on geophysical parameters, such as the wind, from remote sea areas with little or no shipping.

In 1978 the SEASAT satellite was launched; it showed that useful, global information could be obtained on force and direction of marine surface winds by means of a microwave scatterometer which, in the case of SEASAT, measured the microwave backscatter from cells of 50x50 kilometers.

Although the final results of the SEASAT mission indicated that it is in principle possible to measure the wind at sea from space, the spread in the data was rather large and a study of *Woiceshyn et al* [1984] has even shown inconsistencies between colocated wind speeds, obtained near simultaneously with different polarization directions of the radar beam. The cause of these effects has not been established unequivocally, but may be connected with the interaction between long seawaves and the short ones that are primarily responsible for the radar backscatter, with the type of wind parameter used, the sea surface temperature, the presence of surfactants and the calibration of the radar, to name the more generally accepted possibilities.

In 1990 the European Space Agency (ESA) will launch the ERS-1, the first European Remote Sensing satellite. On board the spacecraft is the Active Microwave Instrument package (AMI) which again contains a radar scatterometer. The oncoming launch of this instrument was the driving force to start the research described in this report, which is aimed at deriving an algorithm, based on physical principles, for the interpretation of the ERS-1 wind scatterometer. This aim is reflected in the name of the project: VIERS-1, a Dutch acronym for Preparation

Interpretation ERS-1 data.

Another important environmental problem on which work is being done in the VIERS-1 project is gas exchange through the ocean surface. Recent work at the University of Heidelberg has shown that these processes depend heavily on the mean square slope of the capillary waves (*Jähne* [1985], *Jähne et al* [1987]). It is furthermore well known that the microwave backscatter is related to the small scale wave spectrum. When a relation between microwave backscatter and gas exchange can be established, a big step forward can be made in the modeling of the CO_2 cycle in the atmosphere. Understanding of the CO_2 cycle is a very important issue in the problem of possible changes in the world's climate due to antropogenic influences. The project is therefore not only aimed at acquiring knowledge about the physical processes involved in radar anemometry, but also on those influencing gas exchange across the sea surface.

The objectives of the project can be summarized as follows:

1. Creation of an improved algorithm, based on physical relations, for the determination of wind speed and wind direction from the ERS-1 scatterometer data.
2. Establishment of well based relations between gas exchange processes at the ocean surface, the microwave backscatter and the wind.
3. Obtain increased knowledge of the physics involved in the interaction between microwave signals and the ocean surface.

The final item will also lead to a better understanding of the mechanisms involved in the imaging of ocean waves, bottom topography and internal waves by a Synthetic Aperture Radar (SAR).

These objectives require detailed information on all parameters involved, which is an extremely difficult task in a rough environment like at sea. The experimental programme of VIERS-1 therefore started with experimental studies in wind/wave tanks where it is possible to perform detailed measurements with relatively little effort and conditions can be controlled and precisely reproduced, so that the effect of varying only one parameter at a time can be studied. The disadvantage is that scaling effects may occur. To control these, a phased approach has been taken. The first experimental phase of VIERS-1 is an indoor tank experiment (the Delft wind/wave tank experiment, which

is the subject of this report), then comes an outdoor tank experiment (the Delta tank experiment) and finally an experiment from a platform at sea (the Noordwijk experiment) will be performed. With each step the size of the experimental environment increases. Finally, during the calibration/validation phase of ERS-1 an operational data-set will be interpreted with the new algorithm and the results will be compared with those of the presently available ones.

To improve on our understanding of the physical processes involved in the scattering of radar waves by the wind driven short water waves, the mutual interaction of the large and small water waves and the generation of water waves by the wind, a VIERS-1 modeling group has been created, along with the experimental group. In this group all Dutch institutes, cooperating in VIERS-1, are represented. Research of the above mentioned processes should culminate in the production of two kinds of computer models: a wave model with emphasis on the short (cm) water waves and a radar scattering model. The predictions of these models are to be verified with the experimental data of the VIERS-1 experiments.

The Delft experiment was done in a large indoor wind/wave tank (l x w = 100 x 8 m^2, water depth = 0.8 m), which is excellently suited for this type of experiment; the only important limitation of the facility is that the amplitude of the waves is limited by its water depth. Wind and wave conditions can be carefully controlled. During the experiment special attention was paid to the azimuthal dependence of the radar cross section. Measurements of the microwave cross section and surface extended wave slope measurements were done simultaneously and at the same spot. This allows a careful examination and identification of the scatterers.

The objectives of the Delft wind wave tank experiment can be summarized as follows:

1. Investigation of the microwave backscattering mechanism, especially its dependence on the structure of the water surface (down to centimeter scales), the azimuth angle, the incidence angle and the wind speed.

2. Investigation of the wind/wave interaction (wave generation; dissipation, non-linear interactions).

3. Investigation of the relation between the rate of gas exchange at the water surface, the wind speed, the microwave backscatter and the structure of the water surface.

4. Testing of newly developed wave measurement techniques to be used later in the Delta tank experiment and at the Noordwijk platform.

A listing of the instruments used in the experiment is given in chapter 2.1 of this report.

Some preliminary results of co-located microwave backscatter and wave slope measurements are shown at the end of the report. The combined backscatter/wave measurements show a huge potential for studying the process of microwave backscatter from the water surface.

After the calibration phase is finished the microwave backscatter data will be compared with different wave parameters (slope, height), especially those obtained with the Imaging Slope Gauge, an instrument that produces area extensive recordings of the wave slope. The backscatter mechanisms can then be studied. Furthermore the gas exchange measurements will be related to wave and radar measurements.

SAMENVATTING

Dit rapport beschrijft het experiment dat in november 1987 en maart 1988 in het kader van het VIERS-1 programma is uitgevoerd in de wind/watergoot van het Waterloopkunidig Laboratorium te Delft. Na een inleiding in hoofdstuk 1 wordt in hoofdstuk 2 aandacht besteed aan de gebruikte instrumenten en meettechnieken en wordt het experimentele programma besproken. In hoofdstuk 3 worden de data-verwerking en de eerste resultaten besproken. Hoofdstuk 4 bevat de beschrijving van de verdere data verwerking en enkele slotopmerkingen.

Een belangrijk probleem bij het verkrijgen van operationele geophysische informatie, zoals de wind, wordt gevormd door de zeegebieden met weinig of geen scheepvaartverkeer.

In 1978 werd de SEASAT satelliet gelanceerd. Hiermee werd aangetoond dat het mogelijk is bruikbare waarnemingen van windsnelheid en windrichting op zee van over de gehele wereld te verkrijgen met behulp van een radar scatterometer die de terugstrooiing van microgolven door het zeeoppervlak meet. Bij SEASAT werden op deze wijze metingen verkregen van gebieden van 50 bij 50 km.

Hoewel de SEASAT metingen aantoonden dat het in principe mogelijk is de wind op zee vanuit de ruimte te meten, was de uiteindelijke onnauwkeurigheid van de gegevens toch tamelijk groot en een onderzoek van *Woiceshyn c.s.* [1984] toonde zelfs tegenstrijdigheden aan in metingen die vlak na elkaar van hetzelfde gebied waren gemaakt met verschillende polarisatie richtingen van de radar. De oorzaak hiervan staat niet ondubbelzinnig vast, maar kan gelegen zijn in de wisselwerking tussen lange en korte zeegolven (de laatste bepalen in eerste instantie de radar terugstrooiing), onzekerheid in de hoogte waarop de wind bepaald moet worden, de zeewater oppervlakte temperatuur, de aanwezigheid van stoffen die de oppervlakte spanning van het water beïnvloeden en de ijking van de radar, om enkele van de algemeen geaccepteerde mogelijkheden te noemen.

In 1990 zal het European Space Agency (ESA) de ERS-1 lanceren, de eerste Europese Remote Sensing satelliet. Aan boord bevindt zich dan het Actieve Microgolf Instrumenten pakket (AMI), waarbij zich opnieuw een radar scatterometer bevindt. De aanstaande lancering van dit instrument was de directe aanleiding het onderzoek te beginnen waarvan in dit

rapport het eerste gedeelte wordt beschreven: het ontwikkelen van een rekenprocedure, gebaseerd op fysische principes, voor de interpretatie van de gegevens van de ERS-1 windscatterometer. Dit doel wordt weerspiegeld in de naam van het project: VIERS-1 een half-nederlandse samentrekking voor Voorbereiding Interpretatie ERS-1.

Een ander belangrijk milieu probleem waaraan binnen het VIERS-1 project aandacht wordt besteed is gas uitwisseling door het zeeoppervlak. Uit recent werk aan de Universiteit Heidelberg (BRD) is gebleken dat deze uitwisseling in hoge mate afhankelijk is van de gemiddelde helling van de (korte) capillaire golven (*Jähne* [1985], *Jähne c.s.* [1987]). Verder is bekend dat de terugstrooiing van microgolfstraling nauw verbonden is met het spectrum van de korte golven. Wanneer nu een verband kan worden gevonden tussen de intensiteit van de teruggestrooide microgolfstraling en de uitwisseling van gas, dan betekent dit een grote stap voorwaarts in de mogelijkheden om de CO_2 kringloop te modelleren. Begrip van deze kooldioxide kringloop is van essentiëel belang voor het probleem van de mogelijke menselijke beïnvloeding van het klimaat. Het project is er derhalve niet alleen op gericht kennis te verzamelen omtrent de fysische processen die van belang zijn bij radar anemometrie, maar eveneens op die welke een rol spelen bij het transport van gas door het zeeoppervlak.

De doeleinden van het project kunnen als volgt worden samengevat:

1. Het vinden van een verbeterde rekenprocedure, gebaseerd op fysische principes, voor het bepalen van de windsnelheid en windrichting uit de ERS-1 scatterometer gegevens.
2. Het vinden van goed gefundeerde relaties tussen gas uitwisseling aan het zeeoppervlak, de microgolf terugstrooiing en de wind.
3. Het verkrijgen van meer kennis van de fysische processen die zich afspelen wanneer microgolfstraling het wateroppervlak treft.

Dit laatste zal tevens leiden tot een beter begrip van de wijze waarop lange golven, de structuur van de zeebodem en inwendige golven worden afgebeeld door een Synthetic Aperture Radar (SAR).

Deze doeleinden vereisen een gedetailleerde kennis van alle proces-parameters, hetgeen een buitengewoon moeilijke opgave is in een omgeving als op zee. Het experimentele gedeelte van VIERS-1 begint daarom met experimenteel onderzoek in wind/golf goten, waar het mogelijk is met een betrekkelijk geringe inspanning gedetailleerde metingen uit

te voeren en de gewenste omstandigheden ingesteld en nauwkeurig greproduceerd kunnen worden, zodat het mogelijk is het effect van veranderingen in één afzonderlijke parameter te bestuderen. Het nadeel van deze werkwijze is dat er schalings effecten op kunnen treden. Om deze te kunnen bepalen is een gefaseerde benadering gekozen. Het eerste VIERS-1 experiment vindt plaats in een gesloten goot (het experiment in de wind/golf-goot van het Waterloopkundig Laboratorium te Delft dat het onderwerp vormt van dit rapport), dan volgt een experiment in een open goot (de Delta goot van het WL) en tenslotte een experiment vanaf een platform op zee (de Meetpost Noordwijk van Rijkswaterstaat). Bij elke volgende stap wordt de schaal van het experiment groter. Tenslotte zal gedurende de calibratie/validatie fase van de ERS-1 een hoeveelheid operationele gegevens met de nieuwe rekenprocedure worden bewerkt, waarna de resultaten zullen worden vergeleken met die van de procedures die momenteel beschikbaar zijn.

Om onze theoretische kennis te vergroten van de fysische processen die zich afspelen bij de verstrooiing van microgolfstraling aan de korte, door de wind opgewekte (water)golven en bij het opwekken van deze golven door de wind, is een VIERS-1 model groep opgericht, naast de experimentele groep. In deze groep zijn alle Nederlandse instituten die in VIERS-1 deelnemen vertegenwoordigd. Het onderzoek naar de bovengenoemde processen moet resulteren in twee computermodellen: een model voor de opwekking van de korte (water)golven door de wind, en één voor de radar verstrooiing. De resultaten van deze modellen moeten worden getoetst aan die van de VIERS-1 experimenten.

Het Delftse experiment is uitgevoerd in een grote gesloten wind/golf goot (l x b = 100 x 8 m^2, waterdiepte 80 cm), die bijzonder geschikt is voor dit soort proeven; de enige beperking van belang is de waterdiepte. Windsterkte en golfhoogte kunnen nauwkeurig worden geregeld. Dit experiment was in het bijzonder gericht op het verkrijgen van informatie betreffende de azimuth-variatie van het scatterometersignaal. Gedurende het experiment zijn gelijktijdig de werkzame doorsnede voor microgolfverstrooiing en de structuur van het (water)golfveld gemeten op hetzelfde punt. Daardoor is het mogelijk nauwkeurig de rol van de diverse golfcomponenten op de radar verstrooiing na te gaan.

Het doel van het Delftse experiment kan als volgt worden samengevat:

1. Onderzoek naar het mechanisme van de microgolf verstrooiing, in het bijzonder de afhankelijkheid van de structuur van het wateroppervlak (tot op een schaal van centimeters), van de azimuth richting, van de elevatie hoek en van de windsnelheid.

2. Onderzoek naar de wisselwerking tussen wind en golven en golven onderling (golfopwekking, dissipatie, niet-lineaire wisselwerking).

3. Onderzoek naar het verband tussen de gasuitwisseling aan het wateroppervlak, de wind snelheid, de teruggestrooide microgolf straling en de structuur van het wateroppervlak.

4. Het testen van nieuwe technieken voor het meten van (korte) golven, die later bij de experimenten in de Delta goot en op de Meetpost Noordwijk zullen worden gebruikt.

Een overzicht van de bij het experiment gebruikte instrumenten wordt gegeven in paragraaf 2.1 van dit rapport.

Aan het eind van het rapport worden enkele voorlopige resultaten van op hetzelfde punt en gelijktijdig opgenomen microgolf terugstrooiing - en golfhellingsmetingen gegeven. De meetresultaten blijken zeer interessante mogelijkheden te bieden voor het onderzoek aan het terugstrooiings mechanisme.

Na het voltooien van de calibratie fase zullen de radar gegevens met name worden vergeleken met die van de Imaging Slope Gauge, een instrument dat hellingsgegevens van het wateroppervlak over een bepaald gebied levert. Dit geeft de beste mogelijkheden voor het bestuderen van het terugstrooiings mechanisme. Verder zal het verband tussen de gas uitwisselingsmetingen enerzijds en golf- en radarmetingen anderzijds worden nagegaan.

CONTENTS

CONTENTS (CONT'D)

1. INTRODUCTION.

In November 1987 and February 1988 measurements have been carried out in the wind wave tank of Delft Hydraulics in Delft. The measurements included microwave backscatter measurements, area extended wave measurements, wind measurements and gas exchange measurements. The campaign was the first of a series of experiments planned within the frame work of the VIERS-1 project. The measurements were carried out by the Royal Netherlands Meteorological Institute (KNMI), the Physics and Electronics Laboratory TNO, the Delft University of Technology, Delft Hydraulics and last but not least the University of Heidelberg (FRG). The contribution of the Dutch laboratories was supported by the Netherlands Remote Sensing Board (BCRS), the German contribution has been made possible by a grant of the State Baden Württemberg and the European Community.

For over 20 years now backscattered radar signals have been regarded as a very promising tool for determining ocean wind speeds. The final aim of the research in this field is the implementation of radar derived ocean surface winds into a worldwide meteorological observation system. In this sense satellite observation systems are extremely valuable because of their fast measurement of wind speed or wind stress over large areas. In particular those areas which are not frequently visited by ships, and from which no in situ measurements are available.

In 1990 the European Space Agency (ESA) will launch the ERS-1, the first European Remote Sensing satellite. The most important sensor on board of the ERS-1 is the Active Microwave Instrument (AMI). The AMI consists of a Synthetic Aperture Radar, and a three antenna scatterometer. SAR and scatterometer operate in the C-band (5.6 GHz). The scatterometer is capable of measuring wind speed and wind direction. A nice overview on the different sensors on board of this satellite and its basic modes of operation can be found in *Brooks et al* [1985]. The oncoming launch of this satellite was the driving force behind the research described in this report. This is condensed in the name of the research project VIERS-1 which is a Dutch acronym for Preparation Interpretation ERS-1 data.

In 1978 the SeaSat satellite was launched and operated for approximately 99 days. In this short lifetime it showed that useful, global information could be obtained on marine surface winds by means of its microwave (13.9 GHz) scatterometer. The information on the surface wind speed and wind direction was obtained by measuring the microwave backscatter in cells of 50x50 kilometers under two angles of +45 and -45 degrees with the flight path of the satellite. A lot of research was done on the exact relations between the radar backscatter signals on one side and the wind speed on the other e.g. *Jones et al* [1978[b]], *Guinard et al* [1971], *Schroeder et al* [1982], *De Loor* [1978] etc.. All of these studies were aimed at establishing *empirical* relations between the radar backscatter and the wind speed. Most frequently a relation of the following form was adopted and parameterized:

$$\sigma_o = G(p,f,\Theta,\phi)U^{H(p,f,\Theta,\phi)} \qquad (1.1)$$

The two coefficients G an H are taken to be functions of typical radar parameters: polarization (p), frequency (f), the incidence angle of the beam (Θ) and the angle between the horizontally projected radar look direction and the wind direction (ϕ). There is no real physics underpinning this type of relation. It originates from curve fitting the normalized radar backscatter to the wind speed.

Many different workers have calculated so-called G-H tables, which relate wind speed and radar backscatter for different polarizations and radar frequencies. Figure 1 gives a, far from complete, overview over a number of parameterizations of exponent H in the relation 1.1, for VV polarization and radar frequencies around the Ku band (the SeaSat-A scatterometer frequency band). One can see that the exponent H increases with incidence angles, at least up to incidence angles of 60 degrees. This means that the scatterometer is more sensitive to changes in wind speed at higher incidence angles. One can also see the wide spread in the reported exponents H. This will influence the accuracy of the radar scatterometer as a wind measuring device. The reasons for this wide spread are manifold, and has not been established at the moment. It may have to do with the influence of the long wave spectrum during the measurements, or with the wind parameter used, with the sea surface

temperature, the presence of surfactants or the calibration of the radar, to name a few.

Extracting the wind speed and direction out of Normalized Radar Cross Section (NRCS) measurements means a inversion of 1.1:

$$\bar{U} = U(\Theta, \phi, \sigma_0, p, f) \qquad (1.2)$$

Generally, satellite scatterometers provide only two (SeaSat) or three (ERS-1) measurements of the NRCS per ground cell under different angles ϕ. The incidence angle is constant for all NRCS measurements in that ground cell, also the radar frequency does not change. Finding the wind speed and direction means finding a best fit to a relation like (1.2). Because both, direction *and* wind speed have to be found from only two or three NRCS measurements, the accuracy of the parameterization is very important.

In the case of SeaSat, both VV and HH polarization measurements could be performed for the same ground cell, giving two in principle independent estimates of the wind. These independent measurements of the wind speed and ~direction give an opportunity to compare the results. Recent studies of *Woiceshyn et al* [1984] have shown inconsistencies between the wind speeds derived from the vertically and the horizontally polarized SeaSat scatterometer. This study is based on millions of pairs of observations taken close together in time, under the same environmental conditions. They showed that large differences of more than 2 m/s occur between HH and VV derived wind speeds for low (<5 m/s) and high wind speeds (> 15 m/s). The intermediate wind speeds compare quite well. It should be realized that these differences only tell something about the functioning of the wind extracting algorithm and not about the comparison with the actual surface wind speed. Based on this analysis, *Woiceshyn et al* [1984] propose a new parameterization of the model function (1.1). They divide the function into three regions (2.3::5.3 m/s), (5.3::8.5 m/s) and (8.5::26.5 m/s). This illustrates how difficult it is to find the right parameterization of a relation like 1.1.

Another finding of *Woiceshyn et al* [1984] is that regional biases in the SeaSat derived wind speeds correlate with the sea surface temperature. This would make the algorithm dependant on yet another parameter besides the ones mentioned in (1.1). This is a strong indication that further understanding of the physics involved in radar anemometry is essential to by-pass these effects and to improve the measurement accuracy of the ocean surface winds.

A further point of continuing discussion in the field of radar anemometry is the wind speed to compare the radar-derived wind speed with. Originally the normalized radar cross section σ_o was compared with measurements of the wind speed at a standard height of 10 or 19.5 meters (the standard height of ships anemometers). However, the backscatter of the microwave irradiation is caused by the (small, capillary) ocean waves. Therefore a measure of the wind close to the ocean surface should be a more appropriate quantity to compare the radar wind speeds with. If one examines the literature one can see that many different relations between the normalized radar backscatter and a wind parameter have been found. Many authors relate the NRCS measurements directly to the (neutral) wind at a reference height of 19.5 or 10 meters. However, others like *Jones and Schroeder* [1978] find a better fit with a power law relation between the NRCS and u_*, the friction velocity (see 1.3). Many more people have investigated the relation between the friction velocity and the NRCS. The rationale behind this is, that the friction velocity is a measure for the tangential stress. It is defined as:

$$u_*^2 = -\langle u'w' \rangle = \tau/\rho \qquad (1.3)$$

Here τ is the tangential stress, ρ is the density of the air, u' is the time dependent fluctuation of the wind speed around the mean in the main wind direction: $u'(t) = u(t)-\bar{U}$. Identically, w' is the fluctuation of the wind speed in the vertical direction. Therefore u_* is a measure for the downward flux of momentum from the air into the sea surface. For this reason it was believed to be closer related to the generation of waves and therefore to the radar cross section. Others who tried to relate the NRCS with the friction velocity failed to get a better correlation: *Liu and Large* [1981], *Donelan and Pierson* [1984]. Donelan argues that the energy flux from the wind to the wave components is

dominated by the normal (pressure) stress and not the tangential stress. The energy input from the wind $\partial E/\partial t$ is related to the wind speed and the wave phase speed C by *Al-Zanaidi and Hui* [1984]:

$$\partial E/\partial t \propto \omega \frac{\rho_a}{\rho_w} \left[\frac{\bar{U}(\lambda/2)}{C(\lambda)} - 1 \right]^2 \qquad (1.4)$$

where ω is the radian frequency of the wave component receiving wind input, λ is its wavelength and $\bar{U}(\lambda/2)$ is the wind speed at a reference height $\lambda/2$, ρ_a is the air density and ρ_w is the water density. The wind parameter most directly related to the microwave backscatter will have to be determined. This is one of the objectives of the VIERS-1 programme.

Another facet of radar anemometry still under discussion is the backscattering mechanism. Although the mechanism of Bragg backscattering, see e.g. *Moore, Ulaby and Fung* [1982] seems widely accepted, some investigators have doubts about the validity of some of the basic assumptions of this small perturbation theory. One of these assumptions is, that the significant height of the backscattering waves, the Bragg waves (2-5 cm waves for X-band) is small with respect to the incident electro magnetic wavelength. This condition certainly does not hold in the case of sea waves. In a recent article *Chen and Fung* [1988] have investigated the range of validity of the small perturbation scattering model. They come up with two conditions:

$$k^3\sigma^2 L \ll 1 \qquad \text{and } k\sigma \ll 1 \qquad (1.5)$$

Here $k=2\pi/\lambda_{em}$, the wavenumber of the incident radiation, σ the r.m.s. surface height of the Bragg waves and L the correlation length. The second condition means that errors occur if σ is more than 1/6th of the incident radar wavelength.

At high wind speeds (>15 m/s), it is generally accepted that backscattering is no longer caused by the small Bragg waves. Under these circumstances, backscattering from spilling breakers and wedges (e.g. *Lyzenga et al,* [1983]) becomes important. Sofar only a few attempts have been made to quantify the contribution of these effects to the total

radar cross section of the ocean surface e.g. *Donelan and Pierson* [1987], *Phillips* [1987].

In order to force a breakthrough in the field of radar anemometry, much more knowledge will have to be gained on the actual physical processes involved. This means knowledge of the generation of waves and the transfer of energy between wave components as well as the interaction between the water waves and the electro magnetic waves. Essential to this is knowledge about the structure of the ocean surface. The main problem for studying the mechanism of backscattering from the ocean surface is that very little measurements exist of the waves which are the most important for these processes, the capillaries ones. Some point measurements have been made, but it is dangerous to use these time series, because no conversion can be made from frequency spectra to wave number spectra. The bottle neck here is the lack of a precise dispersion relation in the presence of long waves with their orbital velocities. Knowledge on the wave number spectra is essential for these studies. Only recently the first attempts have been made to measure these waves by means of stereo photography from a platform (*Shemdin,* [1988]). However, no first results are known to the authors at the moment.

Another important aspect of the project is the gas exchange processes at the ocean surface. An effort will be made to correlate the microwave backscatter with the amount of gas exchange at the ocean surface. Recent work at the University of Heidelberg has shown that the gas exchange depends heavily on the mean square slope of the capillary waves e.g. *Jähne* [1985] *Jähne et al* [1987]. On the other hand, it is well known that the microwave backscatter is related to the small scale wave spectrum as well. When a relation between microwave backscatter and gas exchange can be established, a big step forward can be made in the modeling of the CO_2 cycle in the atmosphere. Understanding of the CO_2 cycle is very important in relation to the effect of human activity on the world's climate.

The objectives of the VIERS-1 project can be summarized as follows:

1. Creation of an improved algorithm based on physical relations for the determination of wind speed and wind direction from the ERS-1

scatterometer data.

2. Establishment of well based relations between gas exchange processes at the ocean surface, the microwave backscatter and the wind.

3. Increase knowledge of the physics involved in the interaction between microwave signals and the ocean surface. This leads, among others, to a better understanding of the imaging mechanisms of ocean waves, bottom topography and internal waves by a Synthetic Aperture Radar (SAR).

Studying these physical relations requires obtaining detailed information of all parameters involved. This is extremely difficult to perform in a rough environment like at sea. It is for this reason that the VIERS-1 group decided to 'return to the wind/wave tank'. The wind/wave tank has the large advantage over in situ measurements that detailed measurements can be performed with relatively little effort. Above that, conditions can be controlled and precisely reproduced, so that the effect of varying only one parameter at the time can be studied. The disadvantage is however, that the environment is 'unnatural', scaling effects may occur. In order to control these scaling effects, a phased approach was taken. First an indoor tank experiment (the Delft wind/wave tank experiment), then later an outdoor tank experiment (the Delta tank experiment) and finally an experiment from a platform at sea (the Noordwijk experiment). In each step, the size of the tank/environment increases. This makes the experiment more realistic but at the same time more difficult to perform.

The Delft wind/wave tank experiment, topic of this report, is the first of a series of experiments within the VIERS-1 frame. The experiment was performed in a large indoor wind/wave tank (l x w = 100 x 8 m^2, depth = 0.8 m), excellently suited for this type of experiment. Wind and wave conditions can be controlled carefully, though the amplitude of the waves is of course rather limited. During this experiment special attention was paid to the azimuthal dependence of the radar cross section. Measurements of the microwave cross section were done simultaneous and at the same spot with surface extended wave slope measurements. This allows a careful examination and identification of

the scatterers.

The second experiment is scheduled for March 1989. It will take place in the Delta tank. This is a huge outdoor wave tank: (l x w = 250x5 m^2, depth = 5 m). 80 meters of this tank will be covered with a wind tunnel roof, specially constructed for this experiment. In this tank almost real size waves can be generated with maximal wave heights of up to 2.5 meters. Special attention will be paid to the effect of long waves on the radar backscatter. Also the reflection of spilling breakers will be examined. Wave measurements will be much more difficult to perform. Therefore, special wave measuring equipment has been and will be developed. First tests have been done in the Delft tank with a stereo camera system (see also § 2.1.3). This technique will be further developed so that it can be used in the Delta tank as well as, in the future, at the Noordwijk platform. Funding for this development has been granted by CALSPACE to one of the participants. Besides the stereo system, also other wave measuring equipment will be developed for platform based measurements e.g. the Reflective Slope Gauge (see also §2.1.3).

The final experiment will be conducted in the ocean environment, from the research platform Noordwijk, 9 kilometers off the Dutch coast in 16 meter deep water. Algorithms to be developed during the first two stages of the VIERS-1 project will be tested here. For this purpose again detailed wave measurements will have to be performed together with and close to the radar measurements and the wind measurements. Area extended wave measurements will be done with the stereo camera system, mounted on the meteo boom. Slope statistics will be measured with the reflective slope gauge. Radar measurements will be performed in X-band and Ka-band (35 GHz).

If we want to refine existing algorithms to extract wind velocities from scatterometer data, we need a better understanding of the underlying physical processes: wind driving the short water waves which scatter the radar waves. For this purpose a VIERS-1 modeling group has been created along with the experimental group. All Dutch institutes, cooperating in VIERS-1 are represented in this modeling group. Research

of the above mentioned processes should culminate in the production of two kinds of computer models: a wave model with emphasis on the short (cm) water waves and a radar scattering model. The predictions of these models should be verified with experimental data, accumulated in the VIERS-1 experiments.

This report describes the Delft wind/wave experiment, conducted in November 1987 and March 1988. In chapter 2 attention will be paid to the equipment and measurement procedures used. Also the experimental program will be discussed. Chapter 3 deals with the processing of the data and a discussion of the first results. Finally chapter 4 deals with the future processing of the data and contains the concluding remarks.

2 EXPERIMENT DESCRIPTION.

2.1. INSTRUMENTATION.

The objectives of the Delft wind wave tank experiment can be summarized as follows:

1. Investigation of the microwave backscattering mechanism. Especially its dependence on the structure of the water surface (down to centimeter scales), azimuth angle and incidence angle as well as wind speed.

2. Investigation of the wind/wave interaction (wave generation; dissipation, non-linear interactions).

3. Investigation of the relation between the rate of gas exchange at the water surface, the wind speed, the microwave backscatter and the structure of the water surface.

4. Testing of newly developed wave measurement techniques to be used laterin the Delta tank and at the platform Noordwijk.

As argued in chapter 1, a detailed study of the basic physical relations between wind, waves and electro-magnetic waves can best be performed in a wind wave tank. The Delft wind wave tank was selected because of its excellent features for this type of experiment. Table 1 lists some of its most important characteristics.[1]

The Delft tank is a linear wind wave tank. With its length of 100 meters and its width of 8 meters it is one of the largest in the world. These large dimensions are very useful for a number of reasons. Firstly, the waves generated in this tank are more realistic than those in much smaller facilities. Measurement of the waves confirm this, see §3.1.3.

Table 1. The Delft wind wave tank.

Dimensions (LxWxD)	100x8x0.7 m^3
Wind speed range	0 - 19 m/s
Generated waves	adjustable spectrum
Current	< 1 m^3/s

In the second place, the size reduces the problems with the microwave measurements. Although even in a tank of this size problems are met if one tries to make accurate microwave backscatter measurments, see §2.1.1.

Figure 2 shows a cross section of the tank. The wind generators are located in the air return channel, underneath the tank at the very beginning. The return channel of the wind is located below the water channel. The wind speed range which has been used was 0-15.5 m/s as measured with anemometers in the tank.

A wave generator in the tank can generate waves of a user defined spectrum. The significant wave height is of course rather limited, due to the limited depth of the tank. Only a few measurements were done with mechanically generated waves during this experiment. The influence of long waves will be studied in more detail in the 'de Voorst' tank, where much higher waves of realistic shape can be generated.

A fetch-limiter was used to simulate fetches smaller than 100 m. It consisted of 2 wooden slabs, both connected to an existing small bridge across the flume. The slabs spanned the width of the flume; one was freely suspended from the bridge down to the bottom, the other sloped down from the level of the bridge into the water at an angle of about 30° in the downwind direction. This setup could be moved along the length of the flume and blocked the upwind waves quite effectively.

The most suitable place for the radar measurements turned out to be the end section of the tank, indicated as the 'hammer end'. This choice was mainly determined by the constraints of the radar measurements. In order to achieve a relatively large radar footprint, needed to get sufficient independent scatterers, the distance between the antenna and the footprint had to be as large as possible. Furthermore, the radar antenna (diameter 1.1 meter) had to be outside the main air flow under all experimental conditions. This could only be achieved in the hammer end. The position of the radar footprint is shown in figure 3. This location is approximately 4 meter upwind of the wave absorbing beach. The beach had to be specially adjusted to optimize the absorption of wind generated waves. Only a few percent of the energy of these waves

was reflected.

The hammer end is higher and wider than the rest of the tank. Although this turned out to be a very helpful feature for especially the radar measurements, it had to be investigated what the influence of this widening was on the wind profile. In principle, some disturbance of the wind profile may be expected from such a widening. However it has to be kept in mind that the side sections in the hammer end are closed, so the net air flow through these sections is zero. During the starting of the wind generation, eddies are generated in these side wings. Once the situation stabilizes, very little energy will be absorbed from the main air flow, therefore the influence of the side sections reduces. Detailed measurements have been done on the homogeneity of the wind field in the hammer end, around the experiment location. This will be discussed in §3.1.2.

At the highest incidence angles for the radar, 50 and 60 degrees, it could not be avoided that part of the antenna entered the main air flow in the tank. The disturbances of the antenna, were investigated in detail. A discussion of this can also be found in §3.1.2.

The water in tanks like the one in Delft always contains some pollution. This can be dust, but also oil from pumps etcetera. It forms a film on the water surface, which has a very large influence on the interaction between the wind and the water surface. Sometimes, with a thick film, no waves are generated even at medium (6 m/s) wind speeds. This influences the reproducibility of the measurements and therefore, this film had to be skimmed from the water surface. During our experiments, this was done every day, by collecting the surface film at the end of the tank under low wind conditions (typically 2 m/s) with a specially developed skimmer. It turned out to be a very effective way of cleaning. Even at very low wind speeds (<1.5 m/s) the surface was free of surfactants and waves could be generated and reproduced.

Detailed measurements of the wind, waves and microwave backscatter as well as gas exchange have been performed during the experiments. The following list gives an overview over the sensors used in the experiment. Figure 3 shows the positions of the sensors during the

experiments. Some sensors, e.g. the anemometers have been used on many different places throughout the hammer end. This will be discussed in §3.1.2

Microwave instrumentation.

1. microwave scatterometer, technical details, see §2.1.1.

Wind measuring instrumentation.(technical description, §2.1.2).

2. sonic anemometer.
3. pressure anemometer.
4. array of miniature cup anemometers.
5. two miniature reference anemometers.

Wave measuring instrumentation (technical description: 2.1.3.).

6. Laser Slope Gauge (LSG).
7. Reflective Slope Gauge (RSG)
8. Reflective Stereo Slope Gauge (RSSG)
9. Imaging Slope Gauge (ISG)
10. high frequency wave wire.
11. low frequency, reference wave height sensors.

Gas exchange instrumentation (technical description 2.1.4).

12. He^3 tracer measurements.
13. SF_6 tracer measurements.[2]
14. Controlled Flux Technique (CFT).

Essential in the experiments was the combination of area extended measurement of the water surface by the Imaging Slope Gauge, and the measurement of the microwave backscatter. Both systems were operated simultaneously at approximately the same footprint. The synchronization was correct within 20 ms. Recordings of the water surface have been made during all radar measurements.

The wind measurements could not be done simultaneously with the microwave measurements, because of disturbance of the microwave radiation by the mounting of the anemometers. This was no limitation,

[2]Guest experiment by Dr.R.Wanninkhof, Lamont Doherty Geological Observatory, Columbia University, New York, USA.

however, since the wind conditions reproduced very well. Wind measurements have been done simultaneously with wave measurements during the November '87 campaign.

2.1.1 MICROWAVE INSTRUMENTATION.

Introduction.

The basic principle of a radar or scatterometer is based on two objectives:

- to identify physical features of the scattering object by detecting a radiometric measure of the echo signal, and
- to locate the scattering object by means of ranging, direction and doppler effect.

In the Delft experiment a FM/CW scatterometer has been used. Table 2[3] lists some of the specifications of this scatterometer. The rest of this paragraph deals especially with the modifications necessary for this instrument to operate in the closed surrouding of a wind/wave flume.

Antenna design:

Performing backscatter measurements in a wind/wave tank at short distance from the antenna requires special conditions for the antenna.

3

Type	FM/CW scatterometer
Frequency	9.6 GHz (X-band)
Frequency Modulation	triangular, 50 Hz, 300 MHz
Polarization	HH or VV
Range resolution	50 cm.
Antenna	Parabolic, 1.1 m diameter
Footprint	1×1 m^2
Phase error over footprint	$< 15^{\circ}$
Azimuth angle range	$0\text{-}180^{\circ}$
Incidence angle range	$24.5\text{-}60^{\circ}$

For one, the illuminated spot at the water surface should be large enough to accomodate a collection of independent scatterers. Considering the scatterometer operates at X-band (9.6 GHz, 3 cm wavelenght) this leads to the requirement of an illuminated spot of about one meter diameter. This has large implications on the antenna size and the overall system realization. Due to space limitations in the wind/wave tank, the maximal measurement distance was limited to 4.22 meter.
Because of the fact that the measurements must be extrapolated to larger distances, for comparison with results from other scatterometers based on air- and spaceborne platforms, the curvature of the phase front over the illuminated spot must be limited. Typically the phase error over the footprint should not exceed 1/12 λ, which is only 30 degrees.
So the demands for the antenna are: a flat phase front at the measurement distance and an illuminated spot of 1 meter diameter at 4.22 m. range.
Generally spoken three solutions exist for the choice of the antenna:

- a small antenna (object in the far field)
- a focussed antenna
- a large (reflector) antenna (object in the near field).

Considering the first solution, a small antenna: the far field requirement yields to an antenna diameter of less than 0.12 meter in order to get an illuminated area of one meter diameter at a distance of 4.22 meter. In that case the phase has a deviation from uniform of more than 180 degrees over the one meter footprint. This is unacceptable for this type of experiment as stated above.

The second solution also has a few disadvantages. One: focussing an antenna decreases the footprint size. Therefore the antenna diameter will get impractically large in order to meet the 1 meter footprint criteria. Secondly, the depth of view of an focussed antenna is small. For circumstances as in this experiment, typically a few centimeters, which is too small for the purpose.

So for this experiment the third solution was chosen. In this case the water surface is in the near field of the antenna. In this near field, the radiation is nearly paralel to the antenna axis, so a flat phase front can be expected. However the amplitude distribution shows a large

variation as a function of the distance from the antenna (see fig. 4). The amplitude and phase distributions can be adjusted using different patterns for the feed antenna. A computer program was developed based on the theory of Hansen and Bailin [1959] to calculate the amplitude and phase distributions for different antenna-distance configurations. Based on these computer calculations a 1.1 meter parabolic reflector antenna with an uniform aperture illumination was chosen. In Fig. 5 and Fig. 6 the calculated phase and amplitude distribution are shown for the selected configuration. The first 5 cm. off the antenna axis show a deviation of the average phase of approximately 40 degrees. This deviation accounts however only for about 10% of the total footprint and therefore it is acceptable. Beyond 50 cm, the phase shifts to lower values which is not very important anymore because it is actually outside the footprint. That means this region gets a very small amplitude weighing factor. Figure 6 shows that the effective footprint is about 70 to 80 centimeters wide, which is close to the objectives.

Antenna measurements.

Four different types of antenna measurements have been performed on the antenna system. These are:

- reflection measurements of the feed antenna.
- far field pattern measurements of the feed antenna.
- near field measurements of the antenna system in a flat plane.
- near field measurements of the antenna system in a cilindrical plane.

The first three types of antenna measurements were done at the Delft University of Technology chamber for antenna measurements (DUCAT), the cilindircal antenna system measurements were carried out at the Physics and Electronics Laboratory TNO as a verification of the measurements performed in DUCAT.

- reflection measurements of the feed antenna.
  The feed antenna consists of a waveguide with a square cross-section of 9.5 x 9.5 mm only, filled with a dielectric material. The feed is capable of handling two polarizations.
  The reflection measurements were carried out using an automatic

network analyzer. Both ports (one for horizontal and one for vertical polarization) were measured. The results are shown in fig. 7 and Fig. 8. The ports do not have identical frequency behaviour, so two different operating frequencies were chosen, one for each polarization: 9.67 GHz for vertical and 9.78 GHz for horizontal polarization. The return loss of the feed is rather high. This return loss is an important parameter for this scatterometer, because is uses only a single antenna for transmitting and receiving. A high return loss means that part of the transmitted energy is reflected at the antenna into the receiver. Special care has been taken in hardware as well as processing of the signal afterwards, to avoid saturation of the receiver and insensitivity of the system as a whole.

- far field measurements of the feed.
  In DUCAT it is possible to measure the amplitude of the EM field of an antenna in eight different axis using an automatic measurement setup. In Fig. 9. the results are shown of a H-plane measurement of the feed for two different frequencies (9.45 and 9.75 GHz). It shows a neglectible frequency dependence of the pattern within the frequency band.

- near field phase and amplitude measurements of the antenna system in DUCAT.
  Using a HP8410B network analyser the planar phase and amplitude response of the parabolic reflector with feed antenna were measured in DUCAT. Fig. 10 shows the amplitude response at a distance of 3870 mm, while the phase behaviour is shown in Fig. 11. The measurements are in good agreement with the theoretical calculated amplitude and phase response.

- near field measurements at TNO.
  The measurements were performed in a cilindrical plane. Fig. 12 shows an example of a complete H-plane pattern at a distance of 4500 mm. The spillover lobs are at 110° and -110° and 30 dB below the main lob. These are very reasonable values. The pattern has also been measured over a frequency range of 1 GHz. This is required, because the system is swept in frequency over a range of 300 MHz around the centre frequency. Fig. 13 shows the broadband

behaviour.

Conclusion: the measurements are in good agreement with the theoretical calculations. It has been possible to design and construct an antenna with the required flat amplitude and phase response at the measurement distance of the scatterometer.

The set up in the tank.

The primary demands on the mount of the scatterometer in the tank can be summarized as follows:

1. The mount should allow the radar to view the water surface under a range of incidence angles and azimuth angles, comparable with the range of the ERS-1. The range for incidence angles chosen was: 25-60 degrees. The azimuth range was 0-180 degrees.
2. For all combinations of incidence angle and azimuth angle, the center of the radar footprint should be right above the center of the Imaging Slope Gauge (ISG) illumination system.
3. The measurement distance from the antenna plane to the center of the footprint should be constant with very narrow margins: 4.2 +/- .01 meter.
4. The view of the ISG camera, hanging right above the radar footprint should not be obstructed by the radar, or parts of the mount, for all combinations of incidence and azimuth angles.
5. Also for the large incidence angles, the antenna dish should not disturb the flow of the wind in the tank.
6. The mount had to be very stable indeed, also under conditions with a small part of the antenna dish in the air flow (this could not be avoided for large incidence angles).
7. The antenna and radar had to be easily accessible for a change of theazimuth and incidence angle and some simple radar servicing.

In order to satisfy conditions 1-3 the radar dish had to be moved along certain points of a sphere. with radius 4.2 meters. This could be achieved in the hammer end section of the Delft tank. This hammer end is a widening of the tank in all directions: to the sides as well as in the height. This allowed us to mount the radar and antenna outside the air flow, except for the very large incidence angles ($>50^{o}$). However, at these large incidence angles, the horizontal distance between antenna

and footprint was over 3 meters. Therefore, the disturbance of the wind flow over the footprint was limited (and measured carefully, see §3.1.2).

The radar mount was constructed underneath a walking-bridge, which could be moved across the hammer end section. Thus the radar mount could be moved in the x, y and z-direction in the hammer end (see figure 2.) over a range, large enough to satisfy conditions 1-7. The bridge was stable and easily accessible (cond. 6,7). Changing the azimuth and elevation as well as x,y positioning was done manually. The elevation could be changed remotely.

Data registration.

The reflections from the water surface appeared at beat signal frequency in the radar of about 1100 Hz. For this reason the signal from the radar was band pass filtered between 400 and 1500 Hz. This filtering suppressed many of the strong tank reflections at distances above 8 meters, and so aliasing due to the digitization rate was avoided.

Before and after each measurement a synchronization clock was read out. This clock was also registered on the U-matic video recorder of the camera from the Imaging Slope Gauge (ISG). The precision of the clock was +/-10 ms. Therefore a synchronization between radar and ISG measurement was achieved within approximately 20 ms.

During the upgoing flanks of the triangular modulation, the beat signal was digitized at 12.9 kHz, 12 bits, with a PC-AT based DT2801a A/D board from Data Translation The process of data acquisition is schematically shown in figure 14. The digitization produced 128 samples per flank. These 128 samples were written to the RAM of the host-Olivetti M28 computer by means of Direct Memory Access (DMA). During the down going flank these samples were transferred to the 4.2 MByte RAM extension disk of the Olivetti. On this RAM disk, the data was stored as Integer*2, therefore each sample occupied 2 bytes. This limited the maximal duration of the measurement to 328 seconds, which turned out to be sufficiently long.After the measurement the data was transferred to the hard disk. Finally, after six measurements the data on the hard disk were transferred to a tape streamer unit, the final

storage medium. A complete back up of all data on streamer tape has been made to avoid loss of data due to deterioration of tapes.

Storing the raw data instead of real time data reduction, proved to be very essential during the data processing. Spurious reflections from the tank and internal residue reflection from the radar could be removed by post processing, which increased the sensitivity of the system with about 16 dB. See also paragraph 3.1.1.

Calibration.

Calibration of the radar was done in a few, independent ways. First of all, the main parameter in the calibration, the antenna gain pattern, was calculated as well as measured. The measurements at Delft University (DUCAT) as well as in the near field measurement chamber of TNO proved that the calculations provided accurate results.

During the measurements in the tank, a daily external calibration was performed at the beginning of each day. The calibration object used was a Luneberg Lens, with a well known radar cross section. The Luneberg was mounted on a wooden pole, approximately 30 centimeters above the water surface. Calibration was always done with a completely flat water surface. In this way, almost all radiation incident on the water surface was mirrored away from the receiver. Secondary reflections via the water surface and the walls of the tank could be filtered because of the good range resolution of the radar. Just underneath the Luneberg Lens a plateau of 70x70 centimeter absorbing material was mounted to avoid reflections from the mount and multiple reflections via the water surface and the Luneberg from entering the receiver. The signal returning from the Luneberg was approximately 30 dB higher than the background signal, which is good enough for an accurate calibration.

Beside this absolute, point calibration, the radar backscatter was also measured under 'standard' conditions as often as possible. The standard conditions were: 8 m/s (tunnel wind speed) over 100 meter fetch, radar looking upwind, incidence angle 45 degrees. These signals will be used as a relative area extended calibration in addition to the point calibration with the Luneberg lens.

2.1.2. WIND MEASURING EQUIPMENT.

Introduction.

During the 2 experimental phases of VIERS-1 at the Delft premises of Delft Hydraulics, wind measurements were performed by the Royal Netherlands Meteorological Institute (KNMI). The various places where wind meters were mounted are indicated in figure 15.

During all experimental series two small cup-anemometers were mounted at fixed places in the wind tunnel (cup 6 and cup 7 in fig. 15). These instruments were only intended to monitor the wind speed. They were mounted rather close to the ceiling of the flume to prevent disturbance of the wind field at water level by these instruments.

A number of series of wind measurements were made, either with a vertical array of cup-anemometers or with two fast-responding anemometers - a sonic anemometer and a pressure anemometer - which both measured the three dimensional wind vector. The cup-anemometer array was used to measure the vertical wind profile. The sonic anemometer measured the mean wind vector; the pressure anemometer was used to obtain information about the turbulence characteristics of the flow, especially the roughness length z_0.

Cup anemometers

All cup-anemometers used were of the Ekopower PW-S1 type, which was selected for its small dimensions (86 mm rotor diameter, fig. 16). They were calibrated individually in the KNMI wind tunnel; the results are presented in Appendix B.

The anemometers were mounted on a small mast, designed to give minimal obstruction. The levels of the cups were 30, 40, 70, 120 and 150 cm above the water if the flume was filled with water to the usual 80 cm level; the anemometers were mounted on 50 cm booms on alternating sides of the mast (fig. 17). The booms could be rotated around the mast axis. During the experiments they pointed into the wind under an angle of about 45°; in this way the anemometers were well upwind of the mast and

had sufficient mutual distance not to influence each other.

The rotation velocity of the cups was converted into a pulse train; the frequency of the pulse train was further converted into an analog signal by an EKO 2U-WP unit with electronic threshold-speed compensation.

Pressure anemometer.

The Pressure Anemometer (PA) was developed at KNMI to measure the three-dimensional wind vector low above the sea surface. Its main advantage for the present application is its small sensor volume (fig.18), which allows turbulence measurements at a level well within the boundary layer above the water surface. For a description, see *Oost*, 1983.

The instrument was mounted, together with the sonic anemometer, below a trestle-shaped frame and had a distance to the water surface of 25 cm (fig.19).

A sensor of the PA produces a signal which is approximately proportional to the wind pressure in the direction of the sensor axis and therefore proportional to the square of the wind component in that direction. To get a linear relation with the wind speed the root of each signal is extracted electronically. This value is registered on magnetic tape.

The proportionality between signal and wind speed is only very approximate for this instrument. Therefore a fairly complicated calibration/interpretation procedure must be used, which is described in detail in *Kraan and Oost*, 1988.

Sonic anemometer.

The sonic anemometer (fig. 20) used was a Kayo Denki DAT-300 digital anemometer/thermometer with the conventional 120° sensor array (*Fox*, 1968), mounted below the same frame as the pressure anemometer, but with the center of the sensor array at a level of 97.5 cm. Although the instrument measures the three dimensional wind vector with a repetition frequency of 20 Hz, which would allow analysis of turbulence up to 10

Hz, it was only used for measurements of the mean wind vector, because the distance of 20 cm between the transducers of each component requires mounting the instrument at least 120 cm above the water level for turbulence measurements. This is too high to consider the flow as being determined by the wind speed and the roughness of the water surface only: it also experiences the influence of the flume ceiling.

The output of each component of the sonic anemometer is a DC voltage, approximately proportional to the wind speed in the direction of the axis of that component. A separate unit transforms the signals of the two horizontal components, which include an angle of 120°, into the corresponding signals in an orthogonal frame of reference.

As stated in the last paragraph, the relation between the signal of a component and the wind speed along its axis is again approximately linear. Although the approximation is in fact fairly good in this case, we have nevertheless used the same calibration and interpretation procedure as for the PA.

Data registration.

All wind sensors used produce DC signals, more or less proportional to the wind speed. These data were registered on a Kaiser K 1280 PCM data registration system, which allows various sampling speeds for different channels. The PA and the sonic anemometer were sampled at about 70 Hz per channel (3375/48 Hz, to be precise), the cup-anemometers at 35, 17.6 or 8.8 Hz. The precise sampling frequency was only important for the PA, because only mean values were used from the other instruments. The sonic was sampled at the same - rather high - frequency as the PA only because this allowed the use of an existing computer routine for the interpretation of the sonic data (the routine had been developed for outdoor turbulence measurements with the instrument).

2.1.3. WAVE MEASURING EQUIPMENT.

For a deeper understanding of microwave backscatter, area extended wave measurements resolving the small-scale wave structure are crucial. Different optical instrument have been used allowing both point and area extended measurements during the experiments in the Delft wind-wave facility. The laser slope gauge, and the imaging slope gauge have already successfully been used in other facilities, whereas the reflective slope gauge and the reflective stereo slope gauge are newly developed instruments. For absolute calibration a wire wave gauge, developed by *Lobemeier* (1981) was used.

Laser Slope Gauge (LSG)

This instrument measures time series of the two components of the wave slope (along- and cross-wind) at one point (fig. 21). The light beam of a 5 mW He-Ne laser pierces the water surface vertically from above. The beam is refracted by the slope of the waves. The tilted beam is collected by a submerged receiver. It consists of a Fresnel lens and a diffusor, one focal length f distant from the lens. This arrangement insures that the displacement of the light spot on the diffusor is independent of the wave height. It is only a function of the wave slope. A second lens images the spot on the diffusor onto a dual-axis position sensing photodiode. The amplifier circuit enables the two position signals to be divided by the intensity in order to avoid systematic errors due to intensity variations.

It has been verified that the system allows measurements of the waves up to the highest frequency capillary waves without significant damping. The maximum measurable slope is about 1.2, much higher than in previously designed laser slope gauges *Hughes et al.*, 1977; *Tang and Shemdin*, 1983.

The system is calibrated with a specially designed calibration instrument in which a thin glass plate at the interface between water and air can be tilted to angles up to 45°. Because of the nonlinear refraction law, the signal of the LSG is also slightly nonlinear. Corrections were found from the calibration results.

Reflective Slope Gauge (RSG).

In contrast to the LSG, the RSG is based on light reflection. This offers the advantage that no part of the instrument has to be submerged. Therefore, in the third phase of the VIERS-1 programme, this instrument
can also be used from the Noordwijk platform. The illumination, a monochromatic low pressure Na-vapor lamp, and the sensor, a CCD-video camera, are placed close to each other at about 2 m above the water level. This instrument measures the specular reflections from the water surface. Each time the water surface is perpendicular to the light beam, a reflex is observed. The place where the reflex occurs in the image is directly related to the two-dimensional slope of the reflecting facets. The CCD-camera operates with a wide angle lens (f = 5.5 mm) that allows to measure slopes up to +-0.78 along-wind and +-0.52 cross-wind on an area at the water surface of 3.11 x 2.08 m.

The instrument allows a fast determination of the two dimensional probability density function of the wave slope simply by adding up images. This can be done in real time by an image processing system at a rate of 25 frames/s.

Reflective Stereo Slope Gauge (RSSG)

This instrument is an extension of the RSG. Instead of one, two CCD-cameras are observing the water surface. The whole system is mounted on an optical bench 4.2 m above the water surface. The stereo basis was 0.6 m. Also the light source is modified, as shown in fig. 22, to observe the same specular reflexes with both cameras.

In this way, stereo images of the specular reflexes can be taken, from which their height can be extracted. Fig.23 shows that the specular reflexes from the right and left stereo image are, indeed, identical. In contrast to the RSG, this instrument operates with telelenses (f=70 mm) observing only an area of 44 cm x 29 cm at the water surface. Consequently, it observes only a small slope range of +-3.0 degree in along-wind and +- 2.0 degree in cross-wind direction. To observe reflexes of different slopes it can be tilted around two axe. Thus joint slope-height distributions can be measured. A detailed description of this instrument can be found in *Waas,* 1986.

Imaging Slope Gauge (ISG)

This is the most important wave measuring instrument, since it allows the measurement of the spatial-temporal structure of the waves over a spatial range of up to 1 m x 1 m with 25 frames/s. Thus it gives the most complete information about the waves. The system is outlined in fig. 24. As the LSG, it is based on light refraction. A CCD-camera is located at the ceiling in the hammer end of the tunnel, 4.2 m above the water surface.

The submerged illumination system produces a horizontally changing intensity either in the along- or the cross-wind direction. This is achieved by two rows of 6 150 W Osram halogen metal vapor lamps illuminating a 1.4 m x 1.4 m x 0.2 m large glass container filled with small scattering particles either in along-wind direction or cross-wind direction. This intensity change is compensated by an absorption wedge in front of the CCD camera lens. Therefore, a flat water surface is imaged at approximately constant intensity all over the image sector. When the water surface is sloped by waves, the light beam received by the CCD-camera comes from a place of higher or lower intensity than zero slope due to refraction at the water surface (fig. 24). In this way, the intensity is changing with the wave slope. Depending on the direction of the illumination gradient, the gray value in the image is either proportional to the along- or cross-wind wave slope.

The ISG is capable to image steep slopes larger than 1 (45 degrees). Though these slopes occur rarely they may cause spikes in the radar signal, and thus it is important that they are measured.
The ISG can be calibrated using an artificial wave surface made out of a thin Plexiglas foil with a rigid sinusoidal shape, which is put onto the water surface.

2.1.4 GAS EXCHANGE MEASURING EQUIPMENT.

Three tracer were used to investigate the mass transfer across the aqueous boundary layer: He^3, sulfurhexafluorid (SF_6), and heat. The last tracer allows local and instantaneous measurements of the transfer velocity.

He^3 Measurements

A small silicon rubber tube was laid all along the water tank from 5 to 90 m fetch to load the water. About 200 ml of a He^3/N_2 mixture containing 6.4 ppm He^3 diffused through the highly permeable silicon rubber tube into the water. The procedure took only 10 min. In total about 0.001 ml He^3 was dissolved in the 1000 m^3 water of the water channel. Samples were taken at a fetch of 81 m about 10 cm above the bottom using a PVC tube. The end of the tube was placed about 2 m below the water level so that hydrostatic pressure causes a continuous flow through the tubing. Sampling of the water probes was done with the standard copper tubing. The watersamples were extracted and then measured in a dedicated mass spectrometer system for precise isotopic analysis of He.

SF_6 measurements

(Contribution of Dr. Rik Wanninkhof from Lamont Doherty Geological Observatory, Columbia University, New York)

These measurements were done simultaneously with the He^3 gas exchange measurements. The facility was loaded with SF_6 by dropping a saturated solution of SF_6 into the water at several places. Samples were taken all over the facility.

Controlled Flux Technique (CFT).

This newly developed technique is the first one being capable to investigate the transfer process across the aqueous viscous boundary layer locally and instantaneously. Its principle is the inversion of the classical mass balance measuring techniques in which the flux density across the interface is inferred from time changes in the tracer concentration in water and air. In contrast the CFT applies a known and controllable flux density. Then the transfer velocity is given by the concentration difference between the surface and bulk concentration in the water.

The CFT uses heat as a tracer. An infrared radiator with a mechanical chopper applies a periodic infrared radiation onto the water surface (fig. 25). This radiation is absorbed at the water surface within 20 μm. The heat generated in this way at the surface is

transported across the boundary layer in the same way as a gas tracer. The surface temperature, measured by a infrared radiometer, is then directly proportional to the transfer resistance or inversely proportional to the transfer velocity.

Careful comparative measurements showed that, despite the large difference in the Schmidt numbers of heat (about 7) and gas tracer (around 1000), the gas transfer velocity can accurately be extrapolated from the heat transfer measurements *Libner et al.*, 1987, *Jähne et al.*, 1988).

2.2 EXPERIMENTAL PROGRAMME.

This paragraph deals with the description of the experiments carried out in the Delft wind wave tank. The experiments can be split up in 6 different categories. Of each category the main objectives will be pointed out as well as the experimental approach taken.

A list of the most important parameters of each of the measurements can be found in appendix A.

1. Wind measurements.

Objectives:

- o Measurement of the wind field and flux under varying conditions.
- o Study of the homogeneity of the wind field in especially the hammerend.
- o Measurement and study of the disturbances in the air flow caused by the antenna when it is partly in the air flow.

Description:

The homogeneity of the wind field was measured with the sonic anemometer and the pressure anemometer as well as with the array of cup anemometers at 12 positions (see fig. 15) in the hammer end and in the section in front of the hammer end. This was done for 3 different fetches (25,40 and 100m) and 10 different wind speeds between (U_{10}) 1.9 m/s and 18 m/s.

2. Wave measurements.

Objectives:

- o Measurement of the water surface (area extended) under varying conditions.
- o Study of wave growth and dissipation.

Description:

A full set of wave measurements has been done for many different wind/fetch combinations (see appendix A for details). The influence of the antenna dish on the air flow was measured by comparing measurement with and without the dish.

3. Radar backscatter measurements - azimuth dependence.

Objectives:

- o Study the dependence of the radar backscatter on the angle between the look direction of the radar and the wind direction.
- o Direct correlation of radar backscatter and the structure of the water surface at the radar footprint

Description:

The radar backscatter was measured for both HH and VV polarization simultaneously and at the same footprint as the two-dimensional slope spectrum of the water surface under the following circumstances:

Wind speed 11.2 m/s, fetch 100 m.	
Incidence	Azimuth
45	every 10 degrees from 0 to 180.
35	every 30 degrees from 0 to 180.
	(Also for U_{10} = 5.5 m/s

4. Radar backscatter - wind speed dependence.

Objectives:

- o Study the behavior of the radar backscatter under varying wind speed conditions, from very low wind speeds up to very high wind speeds.
- o Study the backscatter mechanisms by simultaneous measurement of

the water surface and the microwave backscatter.

Description:

Measurement of the radar backscatter under VV and HH polarization conditions, for a range of wind speeds. Together and simultaneously with area extended (ISG) measurements of the wave slope at the radar footprint.

Wind speed / fetch combinations:

Wind speed: U_{10} m/s	2.6	3.9	5.5	6.7	8.6	11.2	13.5	18	max
Fetch [m]	100	100	100	100	100	100	100	100	100
	-	-	40	-	-	40	40	-	40
	-	-	25	-	-	25	-	25	-

5. Radar backscatter - incidence angle dependence.

Objective:

- o Study the scattering mechanism by varying the incidence angle of the radar. Determination of the influence of specular reflectance by measuring the area of specular surface by means of the ISG.

Description:

Simultaneous measurement of the radar backscatter and the area extended water slope with the ISG at the radar footprint for a range of incidence angles: 24.5, 30, 35, 40, 45, 50, 55, 60 degrees. For both, HH and VV polarization, Upwind conditions at U_{10}= 11.2 m/s; fetch 100m.

6. Radar backscatter - influence of mechanically generated waves.

Objective:

- o Study the influence of a mechanically generated wave on the microwave backscatter. Used for later comparison with measurements in 'de Voorst'.

Description:

Measurement of the microwave backscatter HH and VV polarization under conditions with a low wind speed and a mechanically generated wave.

Wind speed U_{10}: 5.5; 11.2 m/s (100 m fetch)

Mech. wave: ca. 7 cm ($H_{1/3}$)

Frequency: ca. 0.5 Hz.

7. Gas exchange measurement.

Objective:

- o Determination of the rate of gas exchange under varying wind and wave conditions.
- o Study of the relation of the rate of gas exchange and the microwave backscatter.

Description:

Measurement of the rate of gas exchange with the three available methods for four wind speeds (U_{10}): 3.3, 5.3, 18 and max (maximum wind speed has to be determined yet). Measurement of the microwave backscatter was not done simultaneously, but later, under identical conditions.

3. PROCESSING AND FIRST RESULTS.

3.1 DATA PROCESSING.

3.1.1. MICROWAVE MEASUREMENTS.

An overview over the data processing of the scatterometer data is shown in figure 26. This processing consists of several steps.

In the first step, spurious signals due to reflections from the tank walls and internal reflections in the radar (due to the use of a single antenna for transmission and receiving) have to be subtracted from the overall signal. This is done in the time, domain. The signals from the tank walls and the internal reflections, can be separated from the signals from the water surface, because the phase of these signals is completely stable. Averaging the beat signal of the radar, as digitized, over 100 to 500 flanks, removes all the reflections from the water surface, whereas, the internal reflections and the tank reflections are not affected at all by this. Estimating these signals this way, the spurious reflections can be subtracted. This improves the sensitivity of the radar with about 16 dB. The background was calculated every 500 records (20 seconds). The influence on the radar reflection from the water surface is estimated at <0.1 dB, which is very good. Averaging over 500 records is a good compromise between on one hand maximizing the length to avoid subtraction of water surface signals and on the other hand minimizing the influence of instabilities of the scatterometer.

Care has to be taken in case of bad records during the recording. About 10% of the measurements have a few bad records. The cause of these bad records has not been established yet. This is still under investigation. It has to be avoided that one or more of these bad records enter the calculation of the background signal. This is why at first the bad records are located and recorded, before calculating the background signals.

After subtraction of the spurious signals, the 128 data points on each flank are multiplied with a $\cos^2$ window. This reduces the influence of the ends of the flanks, where distortions may be present from the

sign switch of the triangular frequency modulation.

After this the power spectrum was taken over each flank. In the resulting spectrum, the frequency axis is proportional to the range. Therefore, the backscatter from the water surface can be separated from reflections of the tank via the water surface, which are located at a larger range and therefore at a higher frequency. The information on the water reflection is located in only 5 frequency resolution cells. Therefore a considerable reduction of the data of more than a factor 20 can be achieved by only saving the wave information part of the spectrum. The wave information cells form a time series of the radar reflection. An example of this is shown in figure 27.

Besides the time series, also the spectra over all flanks were averaged out to serve as a quality control of the data. This averaging was done in the linear domain. After that the remaining spectrum was converted to the dB domain. Figure 28 shows an example of such a spectrum. Clearly the remaining reflections from the tank can be seen at frequencies of 2000 Hz and higher. These are reflections of the tank via the water surface. Because of this last feature, these reflections can not be estimated and subtracted in the first step of the processing.

3.1.2 WIND MEASUREMENTS.

The first series of wind measurements were done in July 1987 with the cup-anemometer array of fig.17 beside the two permanently used cup anemometers (cup 6 and cup 7 in fig.15). The main object of these runs was to find out about the homogeneity of the wind field in the tunnel.

In the next set, which was done in November 1987, both the cup-anemometer array and the PA and sonic were used. In the final series in February 1988 only measurements with the PA and sonic were done.

Runs with PA, sonic or cup-anemometer array were only possible when the radar was not functioning, because the wind meters would cause spurious radar reflections.

Cup-anemometer data.

The original intention was to use the data from the cup-anemometer also to measure profiles, from which, assuming neutral stability, the roughness length and other turbulence quantities could be derived. This would give an independent set of turbulence parameters beside the one provided by the PA.

During the analysis of the data it became clear, however, that despite a number of precautions, such as the slender construction of the mast and the positioning of the cup anemometers upstream of it and as wide apart from each other as compatible with spatial resolution requirements, the data still showed a zig-zag pattern: when a straight line is fitted to the data in a ln(z) versus U(z) plot - with z the height above water level and U the wind velocity - the values belonging to successive anemometers lie alternatingly above and below the line (fig.29).

This effect is known from literature and is brought about by the alternate mounting of successive anemometers on both sides of the mast, which is done to reduce their mutual interference in the vertical direction. The rotation of the cups induces vorticity in the flow which interacts with the deviation in the flow due to the upstream influence of the mast.

Another handicap for the use of the cup-anemometer profiles is the influence of the flume ceiling on the flow, which is already very noticeable at the 120 cm level (fig.29). This leaves us with the lowest three anemometers from which to derive a profile. From these three only two are on the same side of the mast to be combined for a profile; and this profile finally is off by an unknown amount (the zig-zag effect need not be symmetrical).

The remaining conclusion was that the cup-anemometer measurements could not be used to derive roughness lengths and other turbulence parameters. They were very useful, though, in providing information about the homogeneity of the flow in the flume.

Figs. 30-32 give examples of the flow pattern at several levels and at several wind speeds.

Pressure anemometer data.

The results of the PA measurements are presented in Appendix C. Data were obtained under various circumstances, which are indicated with a number under the heading "situation". Using the coordinate system of Fig. 15 their meaning is as follows (first the downstream, then the cross-stream position, both in meters):

0: no radar dish

1: radar dish at 100.5, 9, looking cross-stream, elevation 45°

2: radar dish at 105, 4.5, looking upwind, elevation 45°

3: canceled

4: no radar dish, mechanical waves

5: as situation 2.

After conversion of the data into physical quantities (see *Kraan and Oost*, 1988), the mean values of U, the along stream and W, the vertical component of the wind and the correlation <uw> between their instantaneous values were calculated. A tilt correction was applied to <uw> in case of a non-zero W. From the corrected value the turbulent vertical momentum flux <u'w'> was derived with

$$\langle u'w' \rangle = \langle uw \rangle - U\,W, \qquad (3.1)$$

from which the friction velocity $u_* = \sqrt{-\langle u'w' \rangle}$ can be calculated directly.

Because we perform our measurements close to the surface, we can assume neutral stability, so the change of the wind with height obeys a logarithmic law:

$$U(z) = \frac{u_*}{k} \ln\left(\frac{z}{z_o} \right) \qquad (3.2)$$

with U(z) the wind speed at the height z, k the von Kármán constant (about 0.4) and z_o the roughness length. With U(z) measured at 25 cm above the water level with the PA, u_* just derived and k known, z_o can

be determined.

From U(0.25) and z_o U(10) can be determined according to

$$U(z)=\frac{\ln (z / z_o)}{\ln (0.25 / z_o)} U(0.25) \qquad (3.3)$$

Finally, with U(z) known at all levels the drag coefficient at 10 m height, $C_{D,10}$, can be calculated from the definition of the drag coefficient:

$$C_{D,z} = \left(\frac{u_*}{U(z)} \right)^2 \qquad (3.4)$$

In Appendix C the various quantities and their standard deviations are given (the standard deviations are given in the columns with headings starting with a "D", followed by the quantity concerned).

We have arranged the data in several ways to obtain, not only the optimal values of e.g. the roughness length under various circumstances, but also the shifts in these values with position, fetch, wind speed etc.

Runs 42-51 were made at position 8 with a slowly increasing wind speed. The radar dish was not mounted during these runs. The resulting values for the drag coefficient, the roughness length and the friction velocity for these runs as a function of wind speed are shown in fig.33 a,b,c.

From these figures we draw the conclusion that the drag coefficient cannot be approximated with a linear wind speed dependence. For the somewhat higher (> 4 m/s) wind speeds a quadratic relation suffices. Assuming that the data obtained under other circumstances are not fundamentally different from those presented here, we have used this quadratic relationship for all series of drag coefficient versus wind speed. There is not much sense in trying to make a - rather complicated - fit to the low wind speed values, because the PA was only calibrated down to 4 m/s and deviations from the extrapolation of the calibration values which we have used are quite well possibly. On the other hand,

the increase in C_D at low wind speed is as theoretically expected and has been measured only very rarely.

From (2) and (3) one can easily derive that

$$z_o = z \exp\left(\frac{-k}{\sqrt{C_{D,z}}}\right) \qquad (3.5)$$

so that any curve-fitting for z_o should best be done, not to z_o, but to its logarithm. For curve-fitting to z_o we have therefore used a quadratic fit to $\ln(z_o)$ (compare fig. 34).

In fig. 35 the relation between the presence or absence of the radar (in approximately the position 105, 4.5 in fig. 15) and the flow parameters is checked with the PA at position 5 and at position 6. The conclusion is that no systematic influence can be detected: the values lie well within each others scatter (compare Appendix D).

In fig. 36 the change in the flow parameters between position 6 and 8 with a fetch of 100 m is given. Again the differences are too small to be considered significant.

The same information, but now for more positions and for several fetches is given in figs. 37-39.

Fig. 40 presents the fetch dependence of the flow parameters for position 6, the radar footprint. Here we see a systematic decrease of the drag coefficient with increasing fetch at low wind speeds, but no systematic change at higher velocities.

The data have been used to derive the coefficients for quadratic fits to the data, or, in the case of the roughness length, to the ln of the data.

The results of these fits are presented in Appendix D and figs. 41-43, which should be compared to figs. 37-39. The straight lines in these figures resulted in the cases where measurements were done at only two wind speeds. Fig. 44, a fit to the roughness length itself

instead of $\ln(z_o)$, has been added to illustrate the difference with fig. 42.

Conclusions.

The final conclusion with regard to the flow parameters is that there are no rapid changes with position, which gives confidence in the quantities presented in Appendix D The best policy for the use of this table is of course to select the appropriate values for each situation, but e.g. the presence or absence of the radar dish is too slight to give significant changes of the parameters.

A factor which does cause important variations in the flow is the presence of slicks. The analysis of cup-anemometer data for a situation at the beginning of the working day and another one in which the wind had blown the surface layer to the skimmer at the end of the flume indicated a large difference: a roughness length of 2 mm in the first and of 0.6 mm in the second case at a 10 m wind of 12 m/s. Even though these values themselves cannot be trusted, as explained earlier, their difference still indicates that the flow is very sensitive to any surfactants. The skimming procedure as described in §2.1 proved to be a successful remover of the surfactants.

3.1.3 WAVE MEASUREMENTS.

Except for the ISG, almost all measurements have been processed. In this section, an overview is given.

LSG: time series

The signals of the LSG (along- and cross-wind wave slope) were digitized at the sampling rate of 1 kHz in blocks of 4096 or 8192 values. Two typical examples of time series are shown in fig. 45.

Even at windspeeds as low as 2.2 m/s the waves are remarkably nonlinear. The slope decreases faster than it increases, indicating a larger curvature at the wave crests than at wave troughs. Capillary wave trains with frequencies between 30-100 Hz occuronly seldom and then as short bursts with a duration of only about 0.1 s.

The short 2 s section at 8 m/s shows another effect which is dominant at higher wind speeds: the modulation of the small scale waves both in frequency and amplitude by the dominant 1.1 Hz gravity wave. The high frequency and steep capillary waves occur at the windward side of the gravity waves.

These two examples of time series illustrate that even simple point measurements give some insight in the wave- wave interaction. This is related to the fact that the LSG can equally well measure the highest frequency capillary waves as the dominant gravity wave.

LSG: Frequency spectra

From the recorded time series frequency spectra have been calculated. The spectra shown in fig. 46 are ensemble averaged over 20 to 50 records and additionally frequency averaged with a binomial filter. A detailed discussion of these spectra can be found in *Jaehne* (1988). Here two facts are pointed out:

1. The spectra show significant changes from the shorter fetches of 15 m and 30 m to the large fetch of 90 m. The peaks of the dominant waves decrease and become wider, at the lower wind speeds of 2.2 and 4 m/s wind it is rather a broad hump than a peak.
2. The dominant wave lengths are considerably larger at the longer fetches (comp. chapter 2.1). For example, at 8 m/s wind the dominant wave frequency decreases from 2.48 Hz at a fetch of approximately 15 m, 1.7 Hz at fetch. The corresponding wave lengths are according to a linear dispersion relation 0.25 m, 0.54 m, and 1.29 m respectively. This indicates that at the smaller fetches all waves are in the gravity-capillary range and only at the longest fetch the waves can be considered as gravity waves.

Item 2 leads to the conclusion that the measurements in a large facility like the one in Delft are a real step ahead towards a more realistic simulation of oceanic waves in laboratory facility.

RSG: slope probability density functions; mean square slopes

In contrast to the LSG, the RSG yields only statistical information about the wave slope. By direct addition of the individual images of the specular reflexes (fig. 47) the two -dimensional slope distribution is obtained. Fig. 48 shows the uncorrected distributions for 3.1 and 8 m/s from 2048 added reflex images.

The high information density of the area extended measurements yields exceptionally low statistical fluctuations. These data were corrected for the decreasing illumination at higher angles and for the dimensions of the light source using an iterative decorrelation algorithm.

Then a two-dimensional Gauss distribution was fitted to estimate the mean square slope. Fig. 49[a] shows the good agreement between the mean square slope either determined with the LSG or RSG. At the highest wind speeds the LSG has a tendency to yield mean square slopes which are about 20% higher than the RSG values. This was expected, since at high wind speeds the slopes are sometimes so large that the refracted laser does not meet the optical receiver. Then spikes occur in the LSG leading to a shift of the mean square slope towards higher values.

Because of the good statistics of the RSG, detailed comparisons of the slope distributions can be made. Again, a fetch effect can be observed. At 12 m/s the distribution is significantly more skewed at 15 m fetch than at 90 m fetch (see fig. 49[b]).

ISG: wavenumber-frequency spectra

Wave image sequences obtained by the ISG give the full information about the space-time properties of the waves. In principle, it is possible to calculate three-dimensional wavenumber-frequency spectra from the image sequences. Since enormous amounts of data are involved with such a procedure, we sought for a simpler way to analyze the data yet still to get the combined space-time information. This seems especially important to us, since it allows a direct comparison of the instantaneous wave and radar data. First results of such a comparison of radar and wave data can be found in §3.2 and *Halsema et al.* (1988).

2D-Space-time images were formed by taking an along-wind oriented line out of the image and drawing a new image which has the time as a second coordinate and shows the temporal change of the wave field on that line. In such images the information on the wave direction is lost, since only one space dimension (usually the along-wind wavenumber k_1) is used. Spectra were calculated by performing a 2-dimensional Fourier transform on the space-time images and averaging over 8 images. These spectra can be used as an approximation to the real wavenumber-frequency spectra because even in the extreme case of a uniform angular distribution the distortions of the spectra due to the error in the wavenumber are less than 15%.

Two very interesting effects can be observed:

1. At lower wind speeds (fig. 50a and b), strong nonlinearities become apparent. At 1.9 m/s wind (fig. 50a), the spectrum splits up in three parallel bands. The two higher frequency bands constitute the first and second harmonics of the first one, since the peaks of the three bands lie on a line through the origin, which indicates that they are traveling with the same phase speed. At the same wavenumber, there are also free waves with a lower frequency, traveling slower and independent of the fundamentals of the harmonic frequency bands mentioned above. The spectral densities of both components are about the same. Thus the data directly prove that the wave field consists about equally of free waves and harmonics at this condition. This result is not surprising, since the time series of the LSG already showed the strong nonlinearity of the waves (fig. 45).
2. At higher wind speeds, the splitup is blurred by another effect. Now larger dominant waves cause a strong modulation of the phase speed and thus frequency of the smaller waves. Fig. 50c and d nicely show how the modulation related frequency dispersion increases with wind speed.

In conclusion, the set of optical instruments used for the wave measurements allows to get a deep insight into the complicated nonlinear physics of the waves. Already this preliminary analysis shows a number of very interesting effects.

After this first phase of the wave data analysis now the second phase starts with a detailed comparison of the wave and radar data. Since the image sequences of the ISG have been recorded simultaneously with the radar data not only mean spectral and statistical values can be compared but also the instantaneous signals. For a first analysis, see §3.2.

RSSG

Stereo techniques for the measurement of the water surface topography have been used since 1925 [*Schuhmacher*, 1939]. The labor intensive interpretation of stereo images has prevented extensive use of this technique in oceanography up till now. The interest in stereo photography, however, has persisted, because it is an ideal instrument to get 3D -information of the water surface over a large area, but even in a recent publication *Shemdin et al.*, [1988] the stereo correlation was done manually.

Rapid progress of digital image processing both in hard- and software opens up new possibilities. The processing of the RSSG-data is done automatically without human interaction. Using a fast multigrid correspondence algorithm with a coarse to fine estimate of the stereo parallax reduces the calculation time even on a PC-AT with an image processing card to only 10-15 min for one stereo image.

Sequences of 30-60 images are used to extract the height distribution of the waves. As a test case the height distribution at 8 m/s wind and 100 m fetch is shown in fig. 51.

At the moment we are still in the proces of optimizing the stereo correspondence algorithms. It also turned out that the mechanical stability of the system has to be improved in order to avoid drifts in the parallax caused by minor changes of the focal length of the zoom lenses or the angular orientation of the cameras caused by vibrations when the wind is running.

As a consequence, a redesigned RSSG will be used in the next experiments in the Delta tank and at the Noordwijk platform. Still, progress obtained so far is substantial, since it could be proved that

the stereo images can be processed in reasonable time even with a cheap PC-based image processing system. So there is no doubt that with a more powerful computer system the necessary amounts of data (up to several hundreds of images per condition) can be processed.

3.1.4 GAS EXCHANGE MEASUREMENTS.

During the November 1987 campaign, 4 gas exchange measurements were carried out at 2.8, 4.3, 12 and 16 m/s using He^3 and SF_6 as tracers. The CFT with heat as a tracer was used as well in the February campaign. All He^3 and SF_6 samples have been measured and the gas exchange rates have been calculated. All CFT -measurements have also been processed.

Fig. 52 shows that the decrease of the He^3 concentration in water at 12 m/s wind speed fits shows the expected exponential decay. A summary of all transfer velocities is given in fig. 53. The exchange coefficients between the different tracers differ by up to one order of magnitude, mainly due to their different diffusion coefficient or Schmidt numbers (fig. 53a), but otherwise show a consistent strong increase with wind speed.

A more detailed comparison is possible, when all transfer velocities are corrected for the known Schmidt number dependency e.g. *Jaehne et al.*, [1988] (fig. 53b). Then it becomes evident that at the highest wind speed of 15 m/s the two low soluble gases SF_6 and He^3 show about 40% higher transfer rates than heat. This discrepancy is probably caused by bubbles which enhance the transfer of low soluble gases, whereas the CFT is insensitive to this transfer channel.

The He^3 and SF_6 gas exchange rates at the two low wind speeds are not very accurate, since not enough time was available to get a sufficient concentration decrease.

Nevertheless, the few measurements already show the benefits of multitracer studies. Two steps will follow:

1. More data will be made available from the CFT to allow a correlation of the gas exchange rate with radar and wave signals
2. In December 1988, extensive additional gas exchange measurements

will be carried out in a cooperation between B. Jähne (Scripps Institution of Oceanography, R. Wanninkhof (Lamont, Columbia University), L. Bliven (NASA, Wallops Island) and K. Riemer and P. Schlosser (Heidelberg University). Though no direct part of the VIERS-1 programme, these measurements will also be made available to the VIERS-1 group.

3.2 Discussion

A preliminary comparison has been made between the scatterometer data and data from the ISG, recorded simultaneously. In this paragraph some results will be shown to illustrate the potential of the database acquired.

Figure 54^a shows the, for the moment still uncalibrated, microwave backscatter at HH polarization for upwind conditions at an incidence angle of 45 degrees. The friction velocity u_* was 0.37 m/s (U_{10} 11.5 m/s), the fetch was 100 meter. Figure 55 was recorded under similar circumstances at VV polarization. The data has been averaged over 0.2 seconds (10 independent samples), which reduces the inherent Rayleigh speckle to +/- 2 dB (90% boundaries).

The longest wavelength at this windspeed is approximately 1m and hence can just be resolved by the scatterometer. Modulations of the microwave backscatter by these waves in the HH-polarized signals (fig. 54^a) are clearly visible, whereas they are considerable lower in VV polarization. This phenomenon is well known in the literature (e.g. *De Loor* , 1983).

At t=142 and t=146.5 in figure 54^a two spiky returns occur of about +15 dB with respect to the background level. By means of the ISG recordings these could be identified as breaking waves in the footprint (see below).

Figure 54^c shows some results from the ISG, recorded simultaneous with the microwave signals. Although the ISG records time series of two-dimensional images, here only one particular line in the ISG image

is displayed as a function of time for computational reasons. This line was from the center of the image in the along wind direction. Hence, it is in the propagation direction of the dominant waves. The gray values in the images of the ISG are related to the slopes of the waves. A dark gray value means a slope in the propagation direction of the dominant waves, whereas a light gray value means a slope in the opposite direction. Zero slope at the crest or the trough of waves shows up as a intermediate gray levels. The data from the wave slopes presented here have not been calibrated yet. Care should be taken when comparing signals recorded under different circumstances.

As waves travel through the footprint of the ISG, they show up as a dark band followed by a lighter band. A nice group of travelling waves can be observed in the middle of figure 54^{c}. Waves travel from top to bottom in the space domain and from the left to the right in time domain. The finite travelling time through the footprint causes a deviation from the vertical. The angle of this turning is a measure of the phase speed of the wave: the larger the angle the smaller the phase velocity.

Also smaller waves can be observed. Because of their slower phase speed, they show a larger angle to the vertical than the dominant waves. See e.g. the region around t=155. On top of strong dominant waves (e.g. t=150) they are clearly modulated by these waves both in amplitude and phase speed. The modulation of the phase speed shows up in the 'S'-shape bands across these longer waves.

At about t=142 s and t= 146.5 s very steep slopes can be observed (white and black patches, close together). These belong to breaking waves. These are the same breaking waves which showed up in the microwave backscatter signal (fig. 54^{a}). Note the smoother water surface in between the two breaking events.

By calculating the mean square slope over one line of the ISG image, one gets some measure of the surface roughness over that line and therefore over the footprint for that time. Care has to be taken, because one line is not always a good representation for the whole footprint, but as a first indication it is valuable. Figure 54^{b} shows a

time series of the logarithm of the mean square slope, calculated this way.

A lot of short term modulations with the frequency of the dominant wave (1.1 Hz) can be seen. But also long term increases of the mean square (ms) slope occur with a duration of about 5 seconds. Although the ms wave slope parameter is not the best wave parameter to compare with the microwave backscatter measurements, it is very tempting to do so. It is amazing to see how well the long term and also short term variations of the microwave backscatter follows the variations of this mean square slope.

Figure 56[a] shows a time recording of the microwave backscatter with the radar at an incidence angle of 35 degrees, upwind looking at HH polarization. The wind conditions were: u_*=0.15 m/s, (U_{10}=5.8 m/s), full fetch of 100 meter. At first glance it is amazing how spiky the behavior of the backscattered signal is, especially considering the relative low windspeed, where one would not expect much breaking of waves. Increases and drops of the backscattered signal of over 15 dB occur regularly. Also note the duration of the spikes: 1-2 seconds, which is quite long, considering the size of the footprint. Looking at the wave slope recordings, it appears that the regions of increased backscatter are caused by the strongly localized instabilities of the dominant waves (micro scale breaking). Just after the breaking, circular waves are generated (like dropping a stone in a pool), which travel partly against the wind direction. The whole micro-scale breaking event increases the ms slope a great deal (fig. 56[b]). The general trends for the radar backscatter and the ms wave slope fit extremely well.

Because the circular waves are travelling opposing the wind, they stay within the footprint of the radar (and ISG) for a relative long time, before they decay (1-2 s.)

Another interesting comparison between radar and ms wave slope is shown in figure 57. In this case, the wind speed was increased from 0 to 8.6 m/s (U_{10}). Soon after t=33 s. the first waves appear and the radar responds immediately to the increased roughness of the water surface. The whole process of wave growth up to the equilibrium wave spectrum

takes several minutes in this facility. But the microwave backscatter and the ms slope reach an equilibrium with a much smaller time constant of approximately 10 s. A small 'overshoot' occurs at about 6 seconds after the first waves were generated. This phenomenon can not be traced back to the ms slope values. It has not been analyzed yet.

The data processing of the VIERS-1 data has only just started, but already one can say that a unique and very valuable data set has been acquired. Especially the fact that microwave backscatter and area extended wave information were acquired simultaneously, at the same footprint gives this data set a huge potential for studying the microwave backscatter mechanisms.

4. CONCLUDING REMARKS

The VIERS-1 project was outlined. This project is aimed at a better physical understanding of the processes involved in microwave backscattering from the ocean. The main objective is to come to a physical description of these processes and, from that point, to an improvement of the algorithms used for the determination of windspeed and-direction from satellite borne scatterometers. A secondary goal is to study the relation between gas exchange and microwave backscattering. Two wind/wave tank experiments and one ocean based platform experiment have been scheduled.

The first tank experiment took place in November 1987 and in Februari and March 1988 and is described in this paper. Attention was paid to combined wind, wave and microwave backscatter measurements together with gas exchange measurements. Microwave backscatter measurements have been made simultaneously and at the same footprint as area extensive waveslope measurements.

Analysis of the wind measurements show that the Delft wind wave tank is well suited for this type of experiment. The homogeneity of the wind field in the hammer end was carefully examined. It turned out that no rapid changes of the flow parameters with position could be observed.

The influence of the radar antenna on the air flow was examined. Under few circumstances it could not be avoided that part of this antenna entered the air flow. It turned out that the presence of absence of the radar antenna did not give significant changes on the flow parameters at the footprint of the radar.

Measurements in July 1987 showed that a small slick on the water surface causes important variation on the flow parameters (and also on the wind-wave interaction). Therefore a special surface skimmer was constructed to remove contaminations from the surface of the tank. This skimmer proved to be successful.

Performing microwave backscatter measurements in a surrounding as the Delft wind wave tank is not an easy task to perform. Our objective

was to measure the backscatter over an area of about 1 m^2. Over this area the phase and amplitude front of the e.m. radiation had to be nearly uniform. Several alternative ways, known from literature have been examined, but discarded. A new way of measuring close to the near field zone of the antenna was developed. Phase front and amplitude have been measured over the antenna footprint and proved to be in accordance with the calculations. The excursions from uniform phase and amplitude were considered acceptable for the purpose of the measurements.

Microwave backscatter measurements and simultaneous area extended wave slope measurements have successfully been made at the same footprint . The backscattered signals from the water surface could be separated from the spurious signals from the walls of the tank and the internal reflections from the radar. This made the system sensitive enough to measure even very small signals at the lowest wind speeds used.

Preliminary comparisons between radar measurements and area extended wave slope measurements show very high correlations between the microwave backscatter and the mean square wave slope. Also the breaking of waves could be identified in the microwave backscatter signals. A more detailed comparison will be done in the near future.

Gas exchange measurements were done using three different methods: using He^3, SF_6 and heat as tracers. The Controlled Flux Technique, which uses heat as a tracer, proved to be successful. The advantage of this method is that the gas exchange process can be investigated for the first time <u>locally</u> and <u>instantaneously</u>. Many measurements have been made under changing circumstances which permit a comparison with the microwave backscatter and wave measurements.

The CFT proved to be superior to the use of He^3 or SF_6 as tracers, especially at low wind speeds, because under these circumstances the use of gases as tracers requires very long sampling times (in excess of 8 hours), whereas the CFT is an instantaneous measurement.

At high wind speeds the He^3 and SF_6 gas exchange rates are higher than those measured with the CFT. This discrepancy is probably caused by

bubbles, which enhance the transfer of gases of low solubility, whereas the CFT is insensitive to this transfer channel. Comparison of the different techniques provides a tool to estimate the influence of bubbles in the gas exchange process.

Some preliminary results of collinear microwave backscatter measurements and wave slope measurements were shown. The combined backscatter/wave measurements show a huge potential for studying the microwave backscatter from the water surface.

In the near future the data acquired will be analyzed in detail. First, all data will be calibrated. This applies especially for the radar data. In a second stage, the microwave backscatter data will be compared with different wave parameters (slope, height) as obtained by the ISG. The backscatter mechanisms will be studied. Also the gas exchange measurements will be related to wave and radar measurements.

ACKNOWLEDGEMENTS

The contribution of the Dutch laboratories was supported by the Netherlands Remote Sensing Board. The Institute for Environmental Physics, of the University of Heidelberg was supported by a grant of the state Baden-Württemberg and the European Community.

The authors would like to thank Dr. P. Lobemeier for lending to them his high-frequency wave-wire.

Ir. E. Heemskerk is gratefully acknowledged for his assistence with the near field antenna measurements.

The support of Dr.R.Bayer and Dr.P.Schlosser (mass-spectrometric analyses of the He^3-water samples) and of Prof.Dr.K.-O. Münnich (preparation of the He^3-N_2 gas mixture and assistance in acquiring funding) were of crucial importance for the gas exchange experiment.

One of the authors (BJ) would like to thank especially Mrs. D.Wierzimok, Th.Billen, R.Fischer and K.Riemer and Dr.P.Libner, who have greatly contributed to the success of the experiment during various phases of the preparation and the actual measurements.

REFERENCES.

Al-Zanaidi, M.A. and W.H. Hui, Turbulent air flow over water waves-A numerical study, *J. Fluid Mech.*, **148**, 225-246, 1984.

Brooks, S.R., H.Joyce, F.G. Sawyer and D.J.Smith, The ERS-1 Synthetic Aperture Radar and Scatterometer, *GEC J. of Research,* **3, no.2,** p124-135, 1985

Chen, M.F. and A.K. Fung, A numerical study of the regions of validity of the Kirchhoff and small-perturbation rough surface scattering models, *Radio Science*, **23,** 163-170, 1988.

Donelan, M.A. and W.J. Pierson, Does the scatterometer see wind speed or friction velocity?, *NASA conf. Publ.* **CP 2303**, 75-87, 1984.

Donelan, M.A. and W.J. Pierson, Radar Scattering and Equilibrium Ranges in Wind-Generated Waves With Application to Scatterometry, *J. Geophys. Res.*, **92(C5),** 4971-5029, 1987.

Fox, L.H., Continuous wave three-component sonic anemometer, Final report, AFCRL-68-0180, Bolt, Beranek and Newman Inc., 57 pp., 1968.

Guignard, N.W.,J.T. Ransone jr. and J.C. Daley, Variation of the NRCS of the sea with increasing roughness, *J. Geophys. Res.*,**76,** 1525-1538, 1971.

Halsema, D. van, B. Jaehne, W.A.Oost, C. Calkoen, and P. Snoeij, First results of the VIERS-1 experiment, Proc. of Workshop "Modulation of short wind waves in the gravity -capillary range by non-uniform currents", Bergen aan Zee, May 1988, D. Reidel, Hingham, MA, forthcoming.

Hansen, R.C. and L.L. Bailen, A new method of near field analysis, IEEE Trans. on Ant. & Prop., **7, 1959, pp. 458-467.**

Hughes, B.A., H.L. Grant, R.W. Chappell, A fast response surface-wave slope meter and measured wind-wave moments, Deep-Sea Res., **24** 1211-1223, 1977.

Jähne, B., On the transfer processes at a free air-water interface, Thesis, University Heidelberg, 1985.

Jähne, B. et al, On the parameters influencing air/water gas exchange, *J.geophys.Res.* **92,** 1937-1949, (1987)

Jähne, B., Energy balance in small-scale waves: An experimental approach using optical slope measuring technique and image processing, Proc. of Workshop "Modulation of short wind waves in the gravity-capillary range by non-uniform currents", Bergen aan Zee, May 1988, D. Reidel, Hingham, MA, forthcoming.

Jähne, B., P. Libner, R. Fischer, T. Billen, and E.J. Plate, Investigating the transfer process across the free aqueous viscous boundary layer by the controlled flux method, forthcoming in Tellus, 1988.

Jones, W.L., Wentz, F.J., Schroeder L.C., Algorithm for inferring wind stress from SeaSat-A, J.Spacecraft & Rockets, **15**, no. 6, p.368-374, 1978.

Jones W.L. and L.C. Schroeder, Radar backscatter from the ocean: Dependence on surface friction velocity, *Boundary Layer Meteorology* **13,** 133-149, 1978[b].

Kraan, C and W.A. Oost, A new way of anemometer calibration and its application to a sonic anemometer. Submitted to the *J. of Atmosph. and Oceanic Techn.* 1988.

Libner, P., B. Jähne, and E.J. Plate, A new method measuring reaeration locally and fast, Wasserwirtschaft, **77**, 230-235, 1987.

Liu, W.T. and W.G. Large, Determination of surface stress by SEASAT-SASS, *J. Phys. Oceanogr.*, **11**, 1603-1611, 1981.

Loor, G.P. de, Remote Sensing of the Sea by Radar. Analysis of available data and results of NOORDWIJK '77, PHL 1978-53, 1978.

Lyzenga, D.R., A.L. Maffett and R.A. Schuchman, The contribution of wedge scattering to the radar cross section of the ocean surface, *IEEE Trans. Geosci. Rem. Sens.*, **GE-21(4)**, 502-505, 1983.

Moore, R.K., F.W. Ulaby, A.K. Fung, Microwave Remote Sensing II, Addison Wesley Publ. Comp., Reading, Mass. 1982.

Oost, W.A., The pressure anemometer- an instrument for adverse circumstances, *J. Clim. Appl. Met.*, **12**, 2075-2084, 1983.

Phillips, O.M., On radar returns from the sea surface - Bragg scattering and breaking waves, *17th Symp. on Naval Hydrodynamics,* The Hague, 1987.

Phillips,O.M., The Dynamics of the Upper Ocean, New York, Cambridge University Press, 1977.

Schroeder, L.C., D.H.Boggs, G.J. Dome, I.M. Halberstam, W.L. Jones, W.J. Pierson and F.J. Wentz, The relationship between wind vector and normalized radar cross section used to derive SeaSat-A satellite scatterometer winds, *J. Geophys. Res.* **87**, 3318-3336, 1982.

Schuhmacher, A., Stereophotogrammetrische Wellenaufnahmen, Wissenschaftliche Ergebnisse der deutschen Atlantik Expedition auf dem Forschungs- und Vermessungsschiff Meteor, **7**, 1939.

Shemdin, O. H., H. Minh Tran, and S.C. Wu, Directional measurements of short ocean waves with stereophotography, forthcoming in J. Geophys. Res., 1988.

Tang, S., and O.H. Shemdin, Measurements of high frequency waves using a wave follower, *J. Geophys. Res.* **88**, 9832- 9940, 1983.

Waas, S., Development of an instrument to measure joint slope-height distributions of water surface waves with a stereo camera system. Diploma thesis, Institute for Environmental Physics, University of Heidelberg, 1988. (In German)

Woiceshyn, P.M., M.G. Wurtele, D.H. Boggs, L.F. McGoldrick and S. Peteherych, The necessity for a new parametrization of an empirical model for wind/ocean scatterometry, *J. Geophys. Res.* **91(C1)**, 2273-2288, 1986.

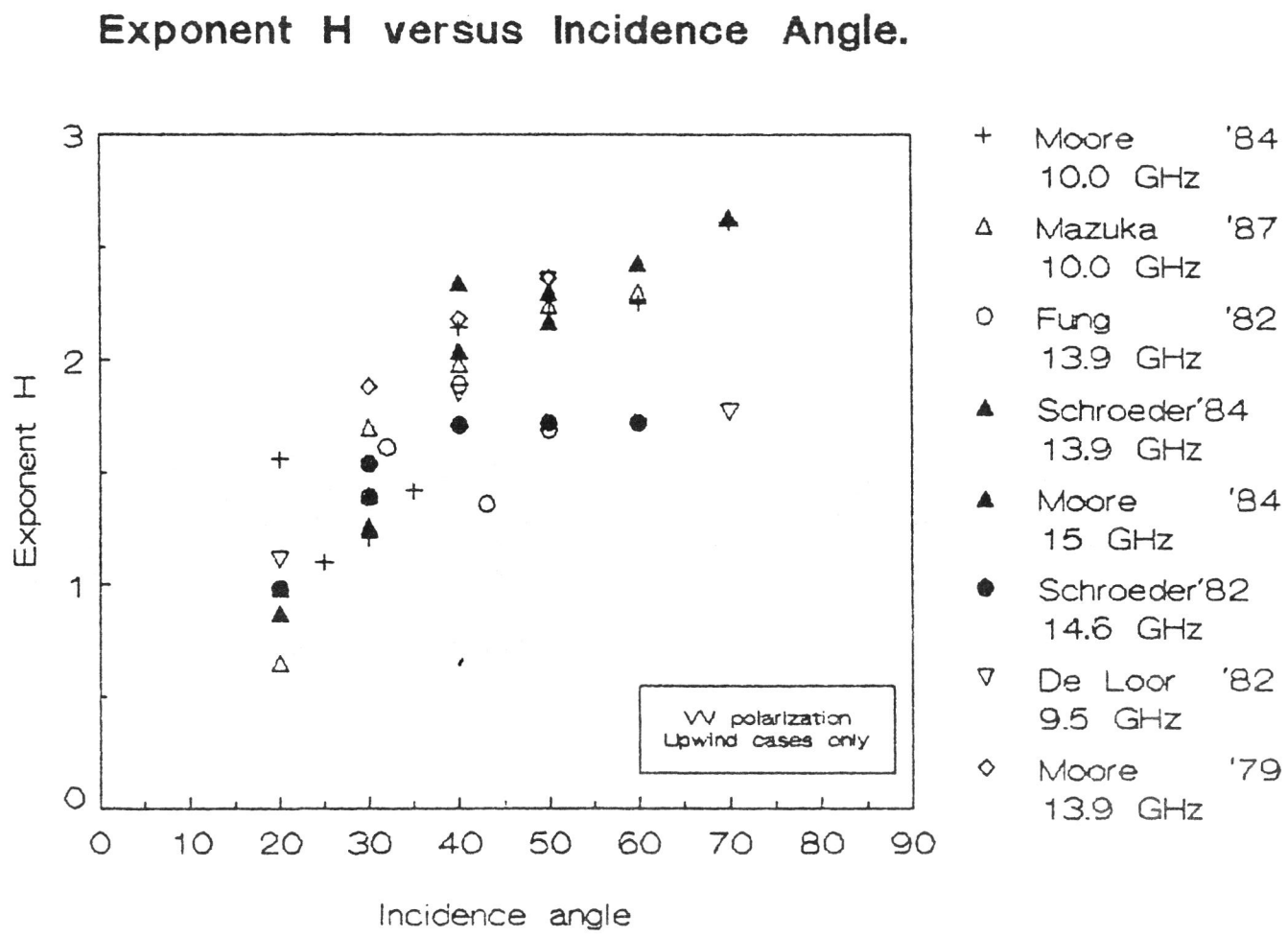

Figure 1: Wind speed dependence exponent $H(f,p,\theta,\phi)$ (see 1.1) as a function of the incidence angle θ, as obtained from several publications in the literature.

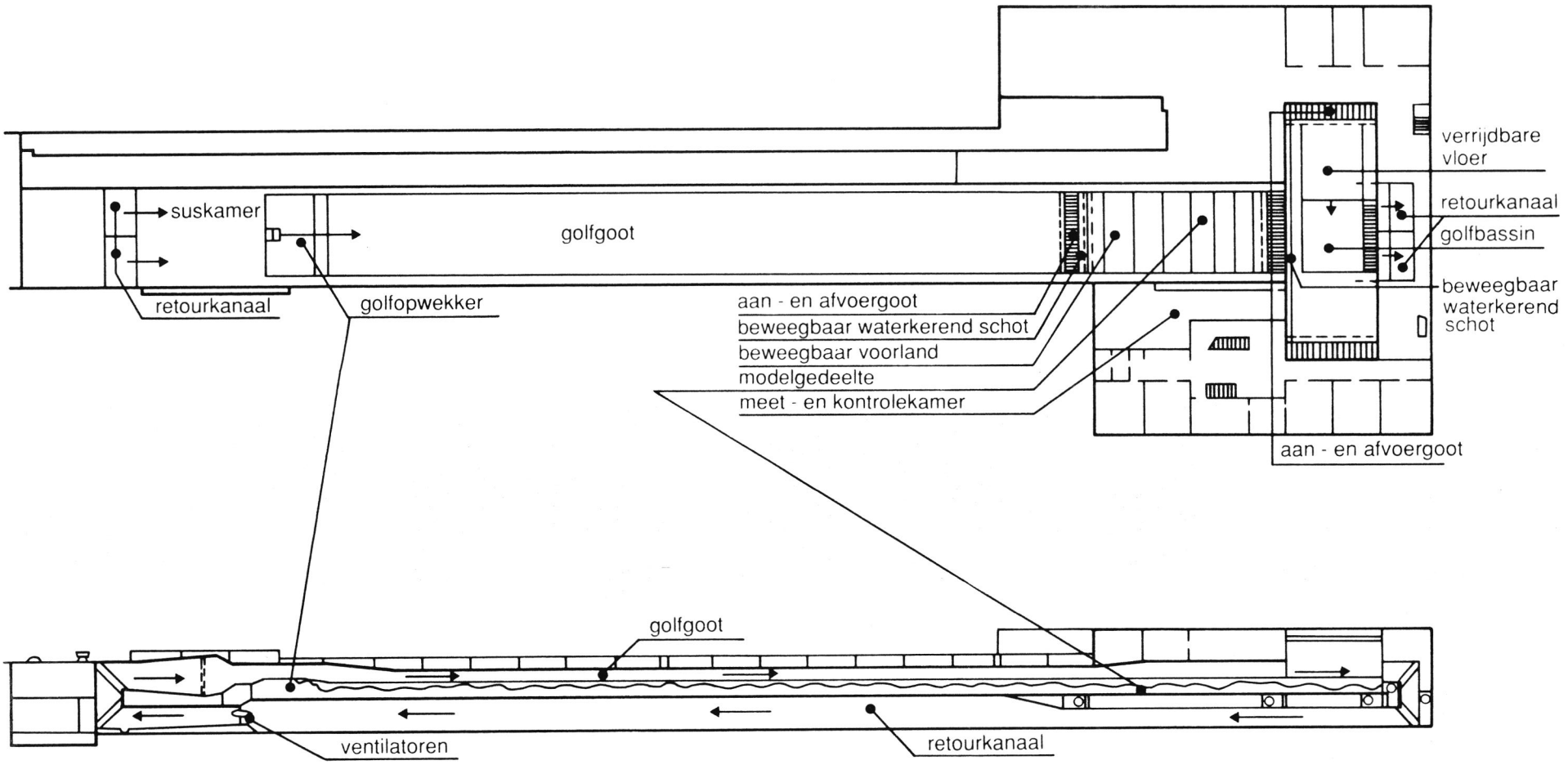

Figure 2: Map and cross section of the Delft wind wave tank. The equipment was located in the end section of the tank (right hand side) in the so-called "hammer end". This hammer end is wider and higher than the remaining part of the facility. Total length of the facility: 100 m, width: 8 m, depth: 0.80 m (maximum). Wind speed range (U_{10}): 0 - 20 m/s.

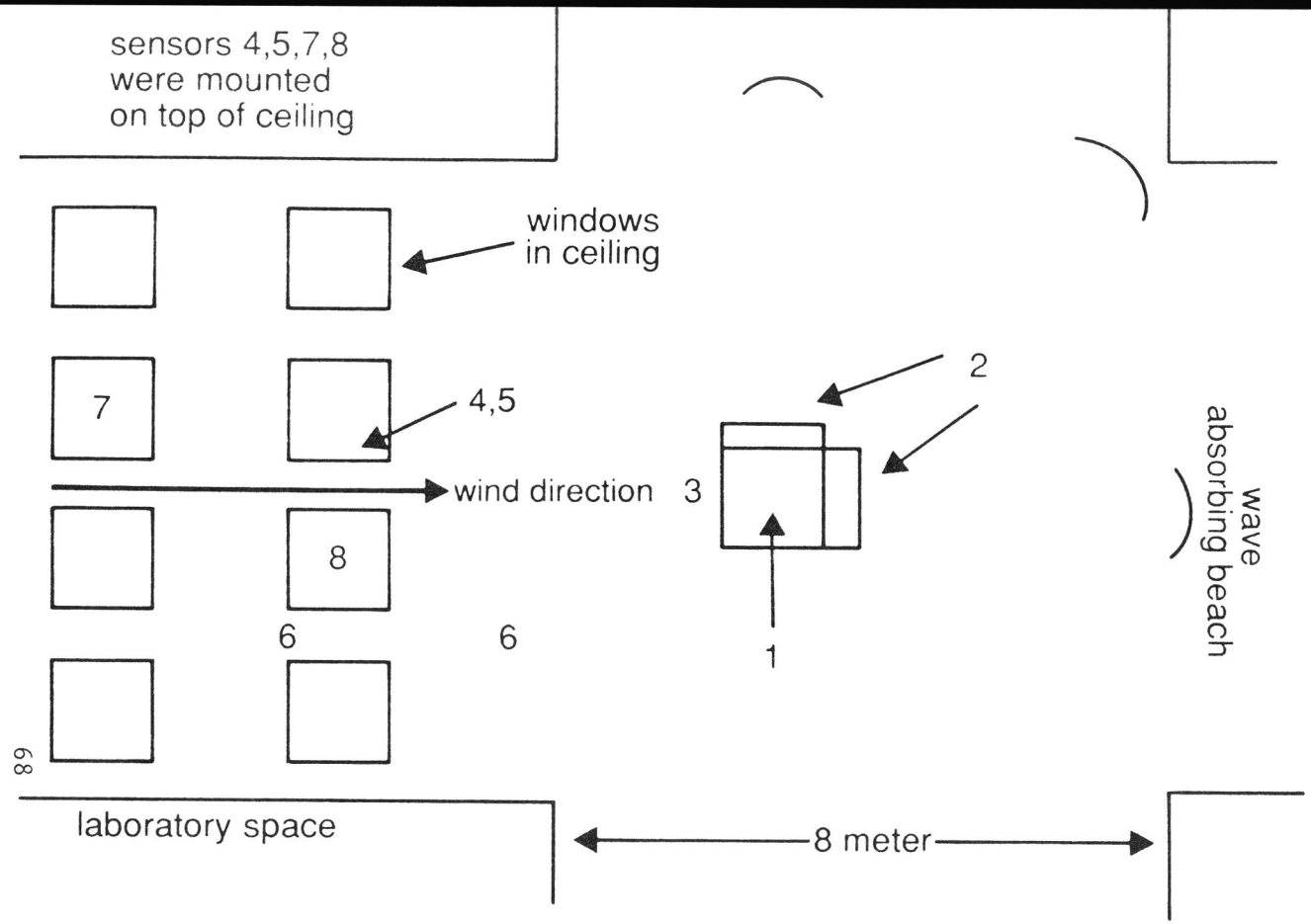

Figure 3: Locations of the various sensors in the hammer end.

1.Microwave scatterometer footprint.

2.Imaging Slope Gauge illumination source.

3.Reflective Stereo Slope Gauge.

4.Laser Slope Gauge.

5.High frequency wave wire.

6.Reference wave height sensors (low frequency).

7.Reflective Slope Gauge.

8.Controlled Flux Technique.

The anemometers have been used at 12 different positions throughout the hammer end; compare fig.15.

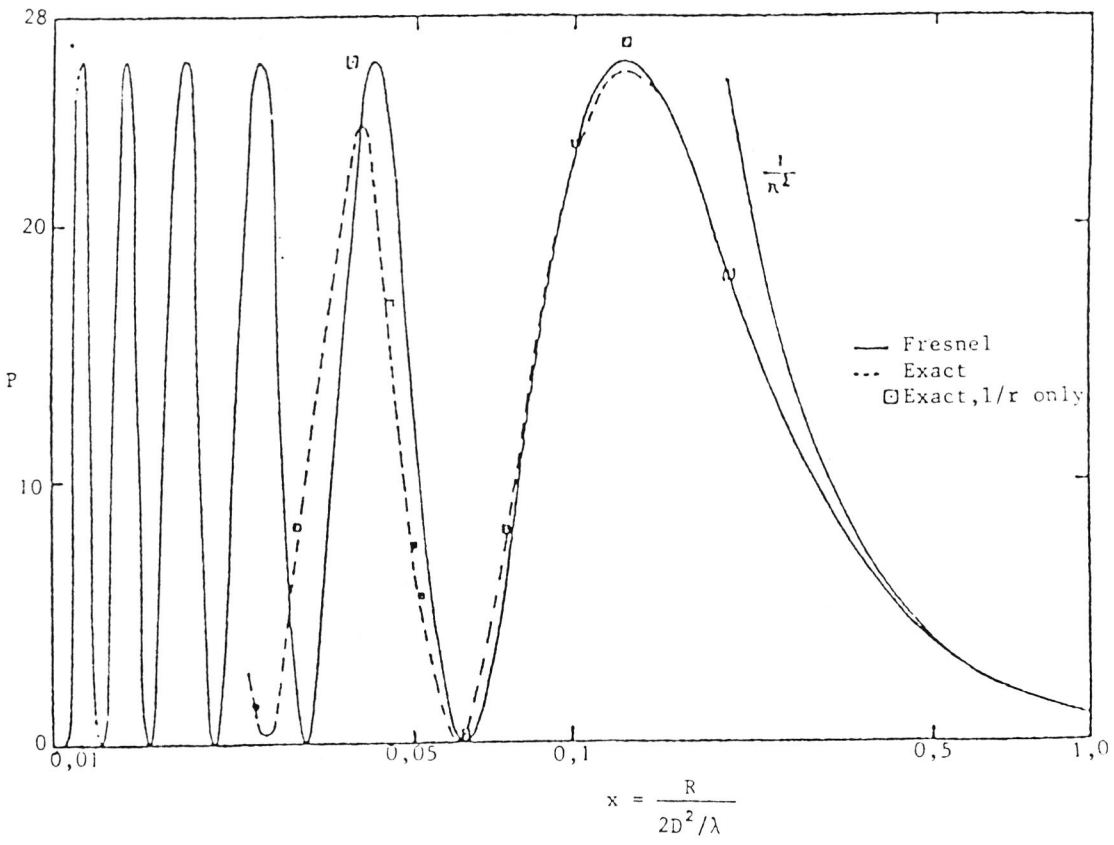

Figure 4: The near field on the antenna axis as a function of the distance.

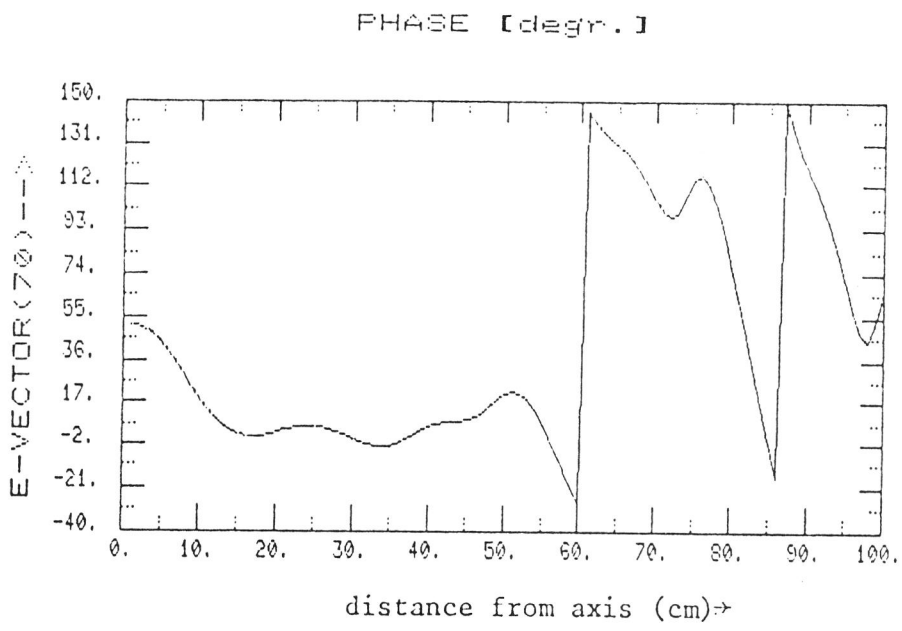

Figure 5: The phase of the electrical field at a distance of 4.22 m for a 1.1 m antenna, perpendicular to the antenna axis.

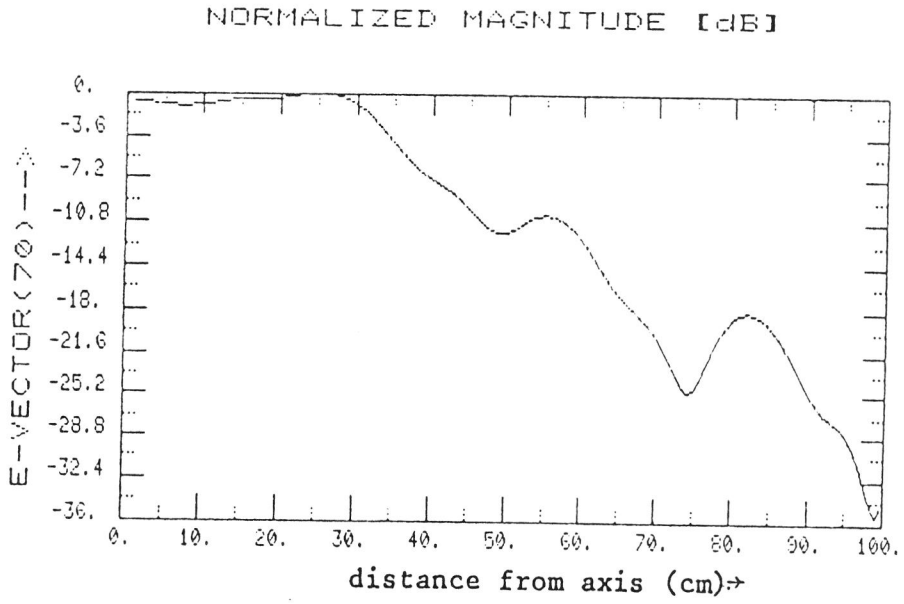

Figure 6 The amplitude of the electrical field at a distance of 4.22 m for a 1.1 m antenna, perpendicular to the antenna axis.

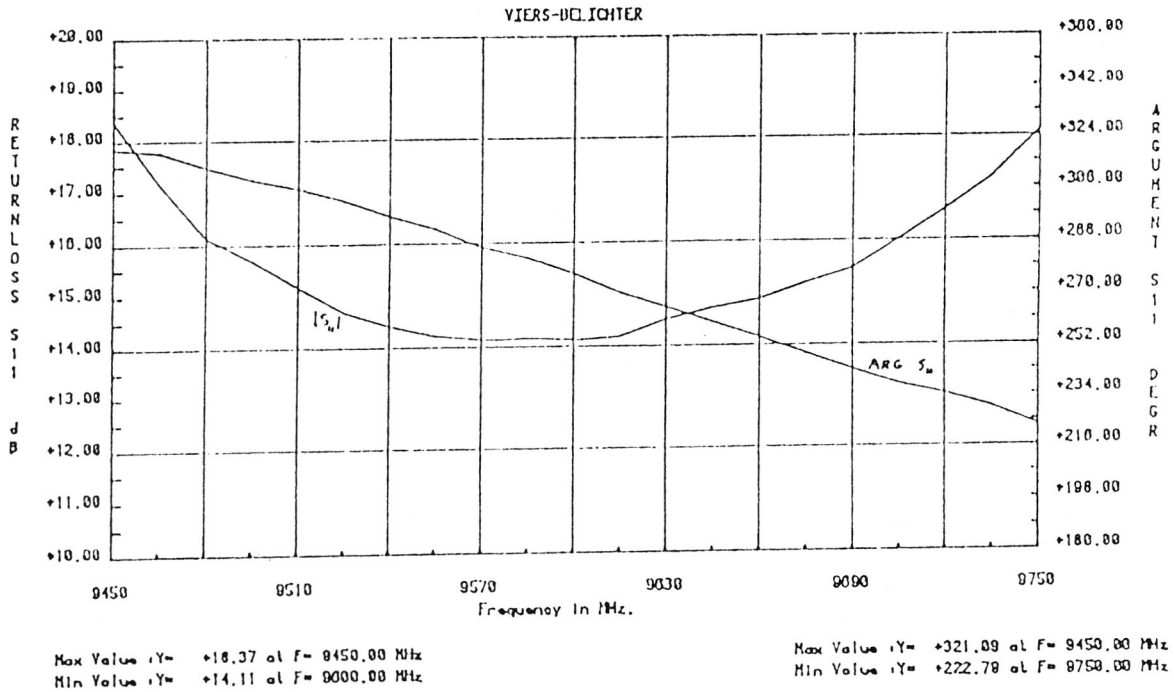

Figure 7: The return loss of port 1 of the feed as a function of frequency.

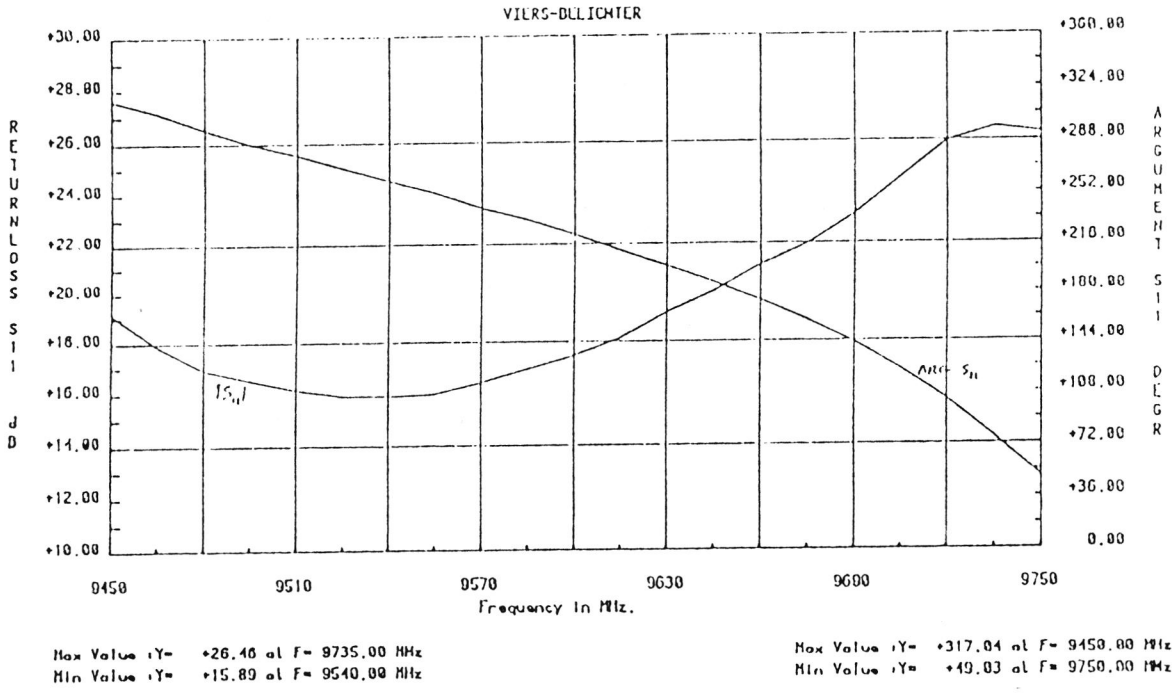

Figure 8: The return loss of port 2 of the feed as a function of frequency.

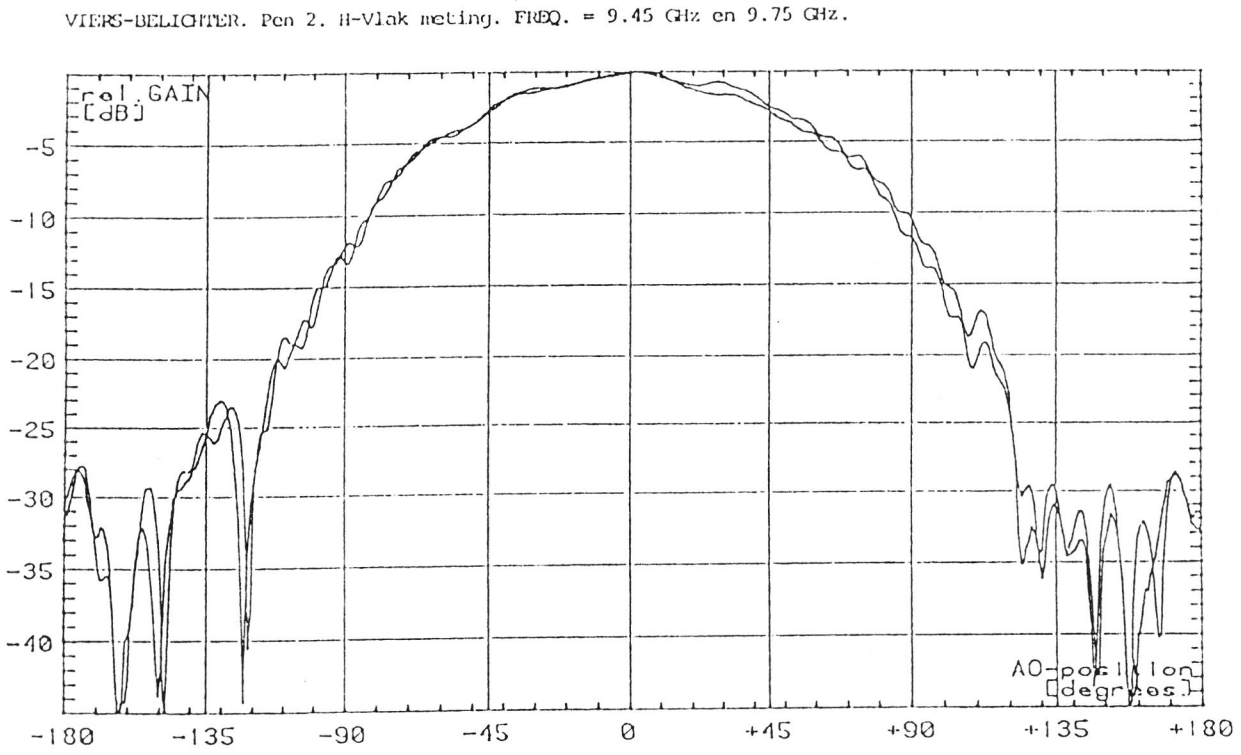

Figure 9: H-plane pattern measurement of the feed antenna for two different frequencies (9.45 and 9.75 GHz).

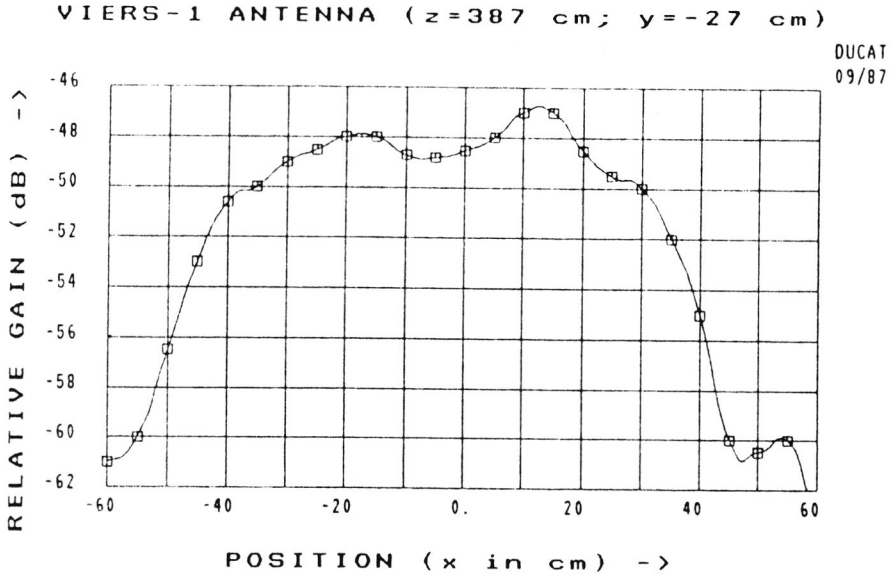

Figure 10: The amplitude response of the antenna system at a distance of 3.87 m.

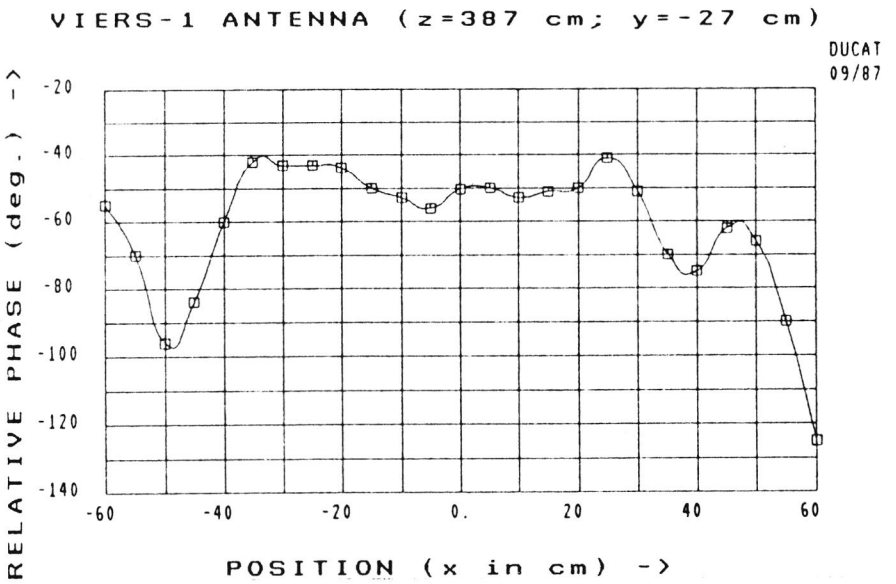

Figure 11: The phase response of the antenna system at a distance of 3.87 m.

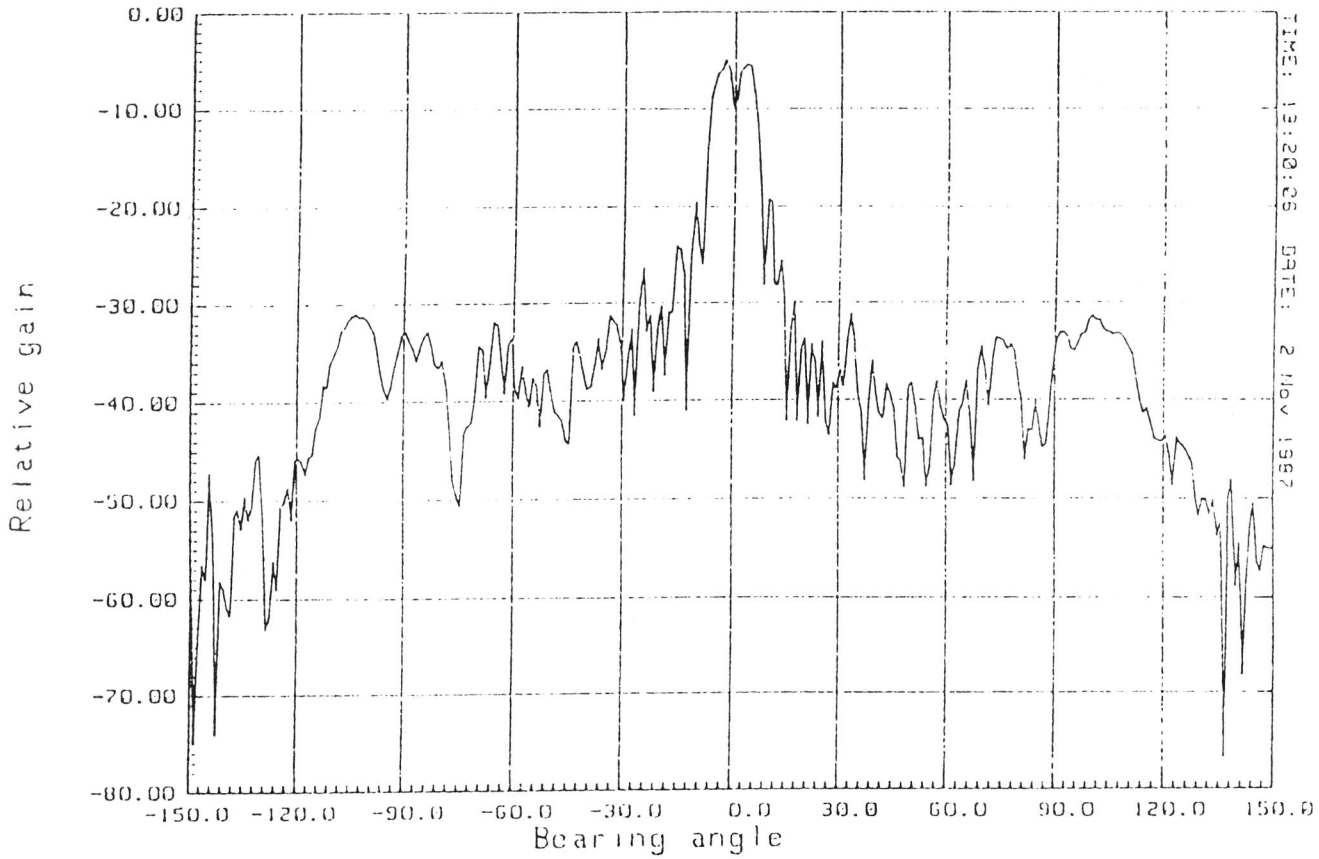

Figure 12: H-plane pattern at a distance of 4.5 m.

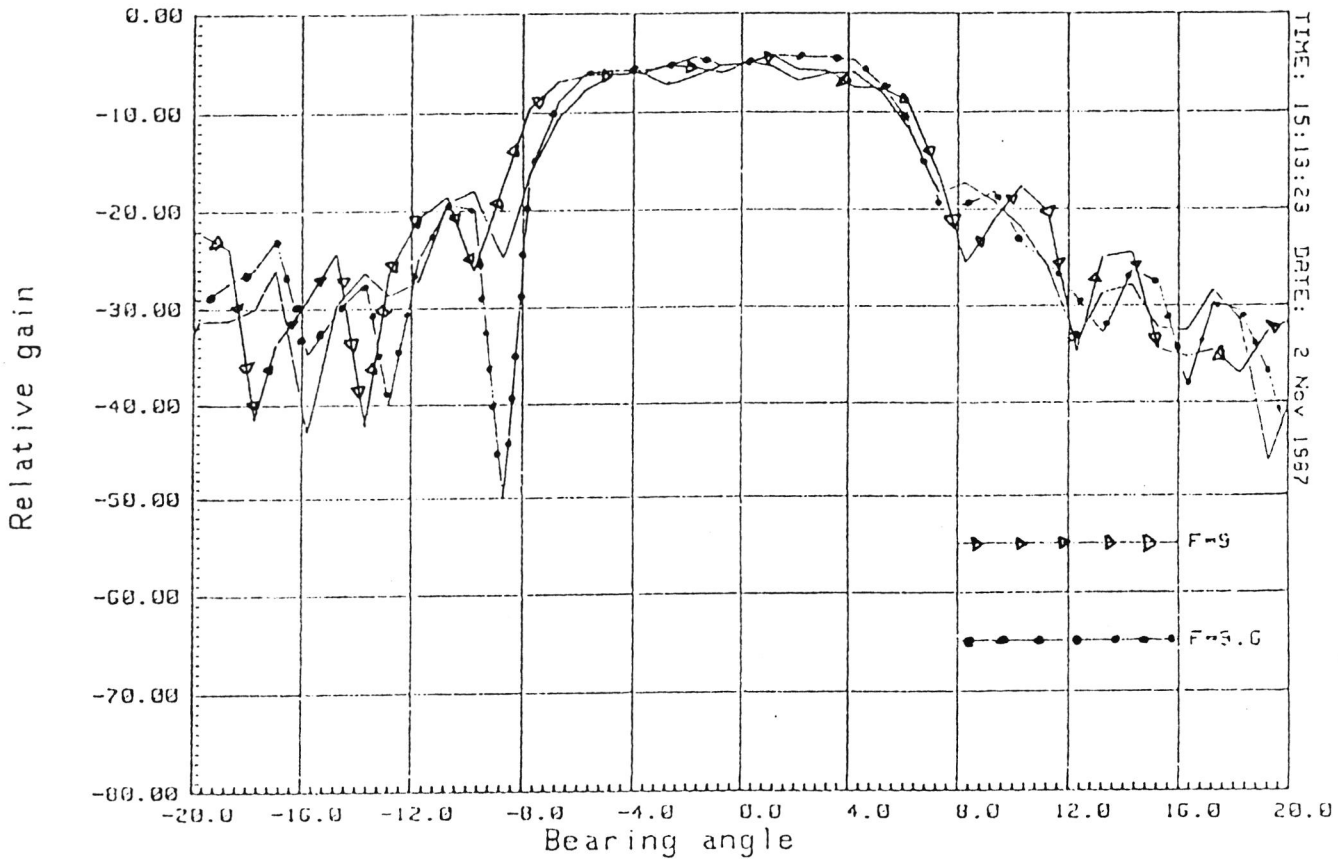

Figure 13: H-plane pattern measurement for three different frequencies (9.0, 9.6 and 10.0 GHz) at a distance of 4.18 m.

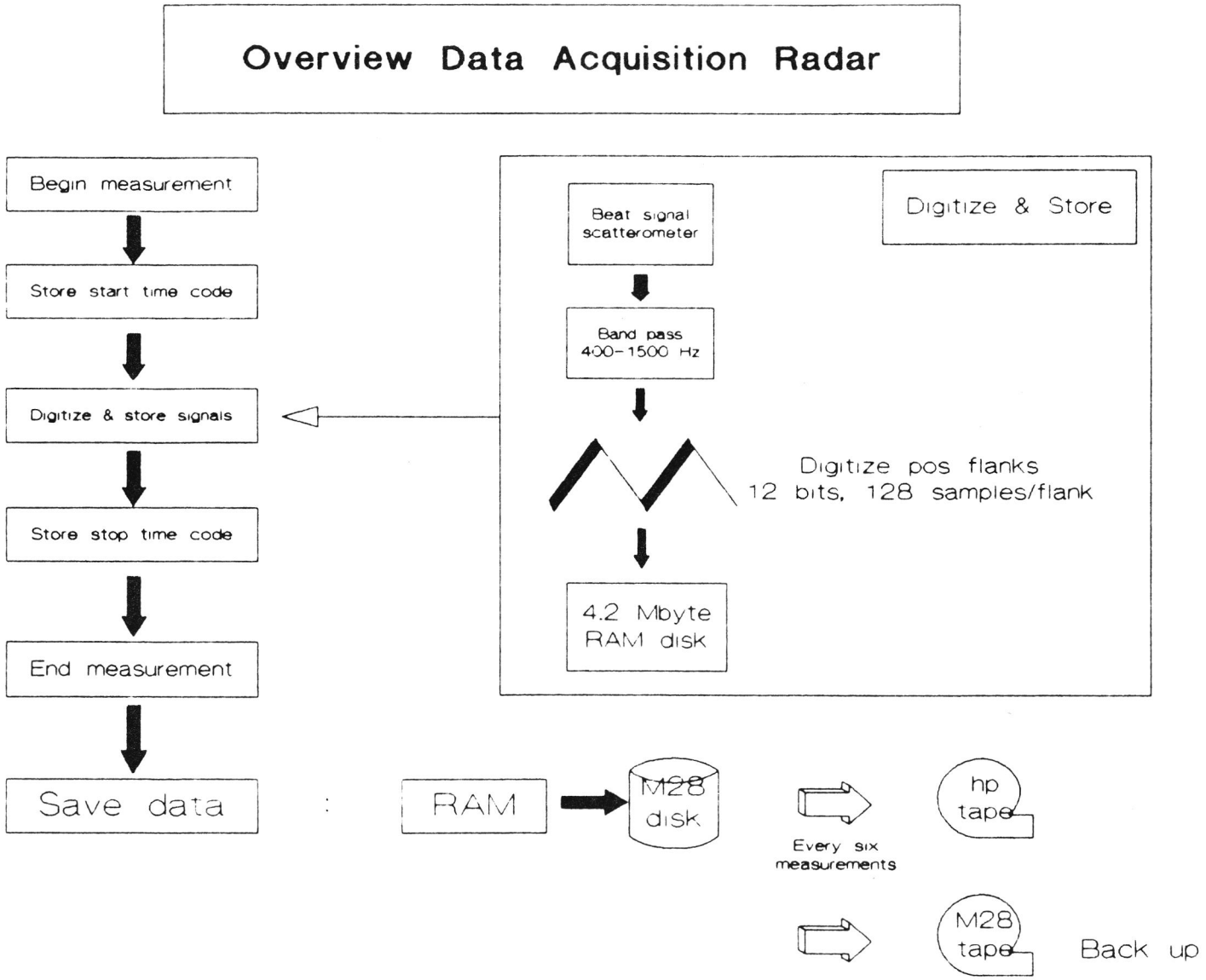

Figure 14: Schematic overview of the data acquisition of the radar.

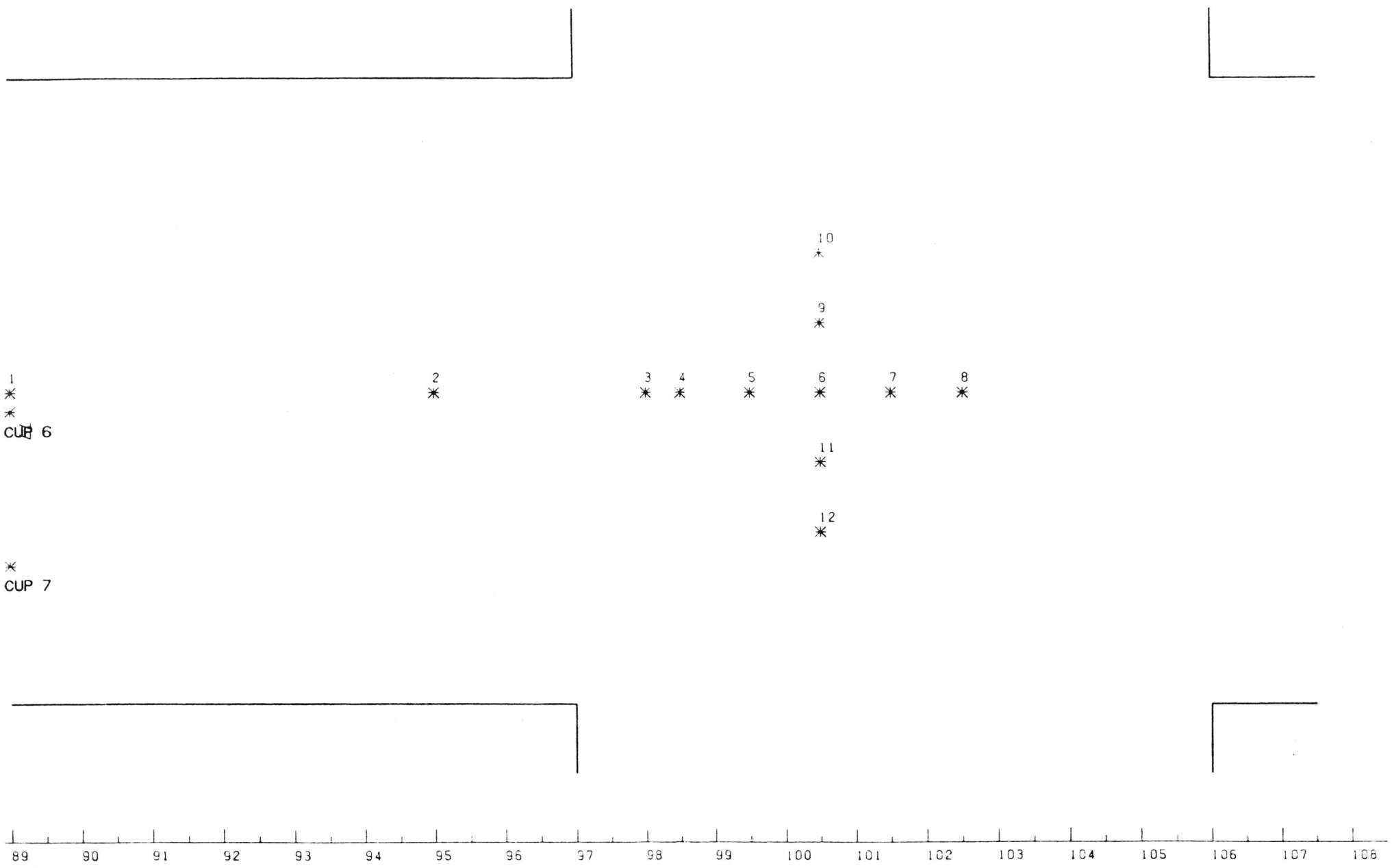

Figure 15: The various positions of anemometers in the flume.

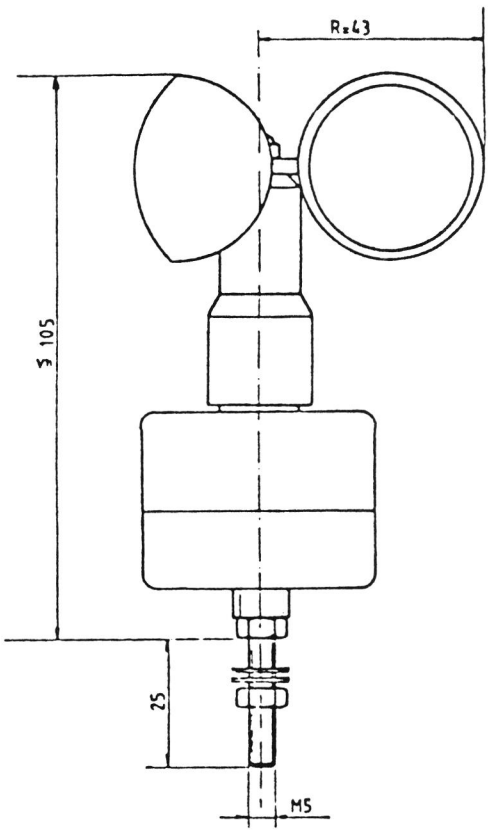

Figure 16: Ekopower PW-S1 cup-anemometer.

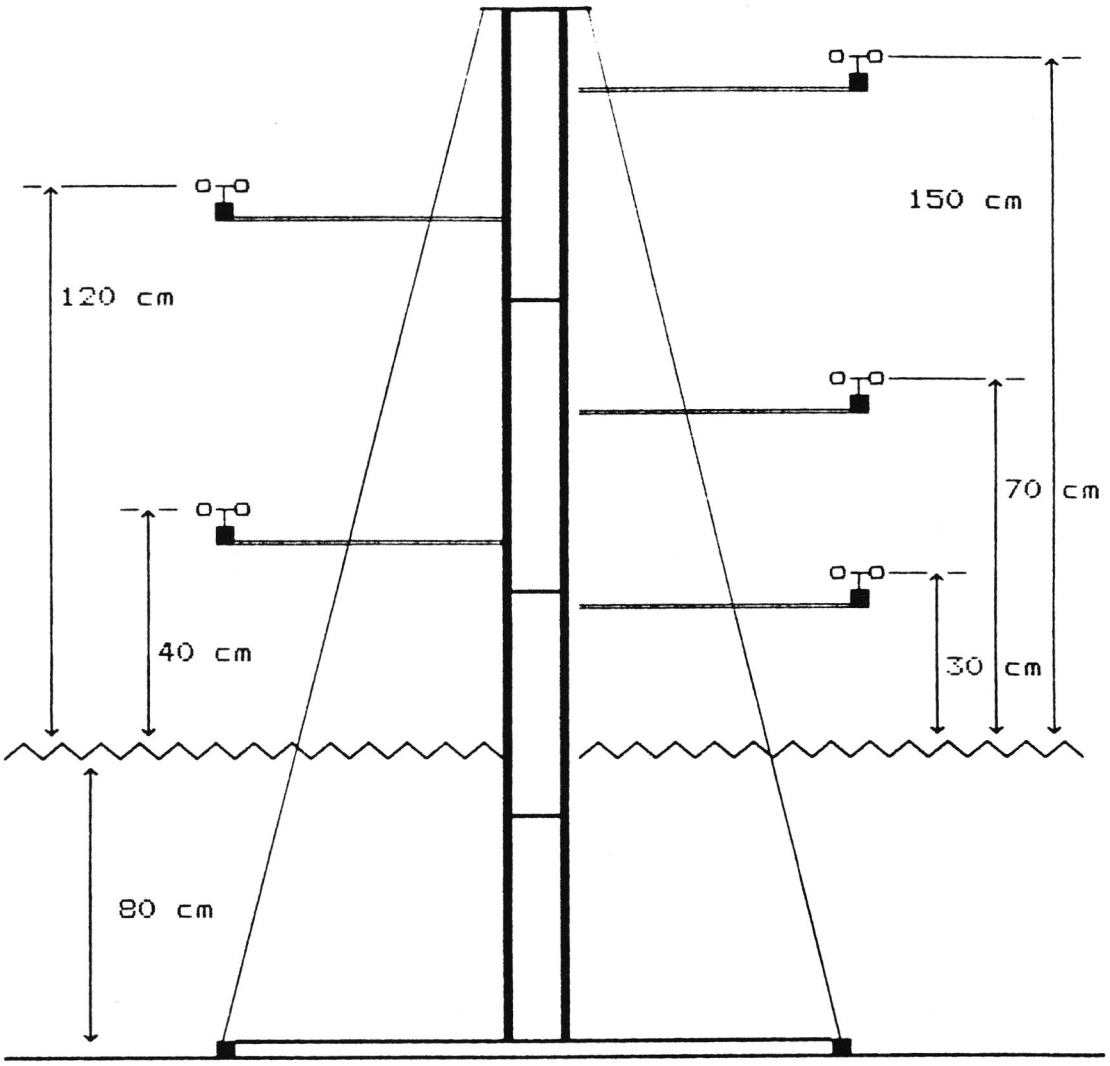

Figure 17: Cup-anemometer mast.

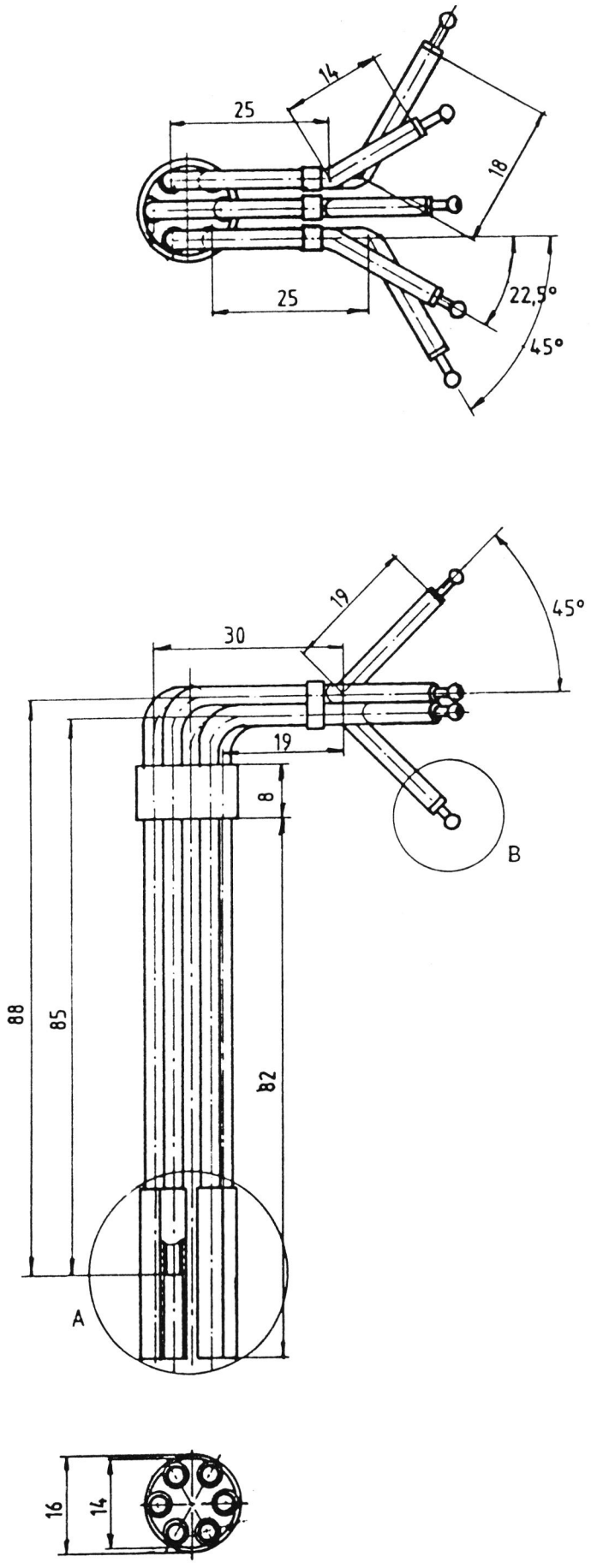

Figure 18: The pressure anemometer.

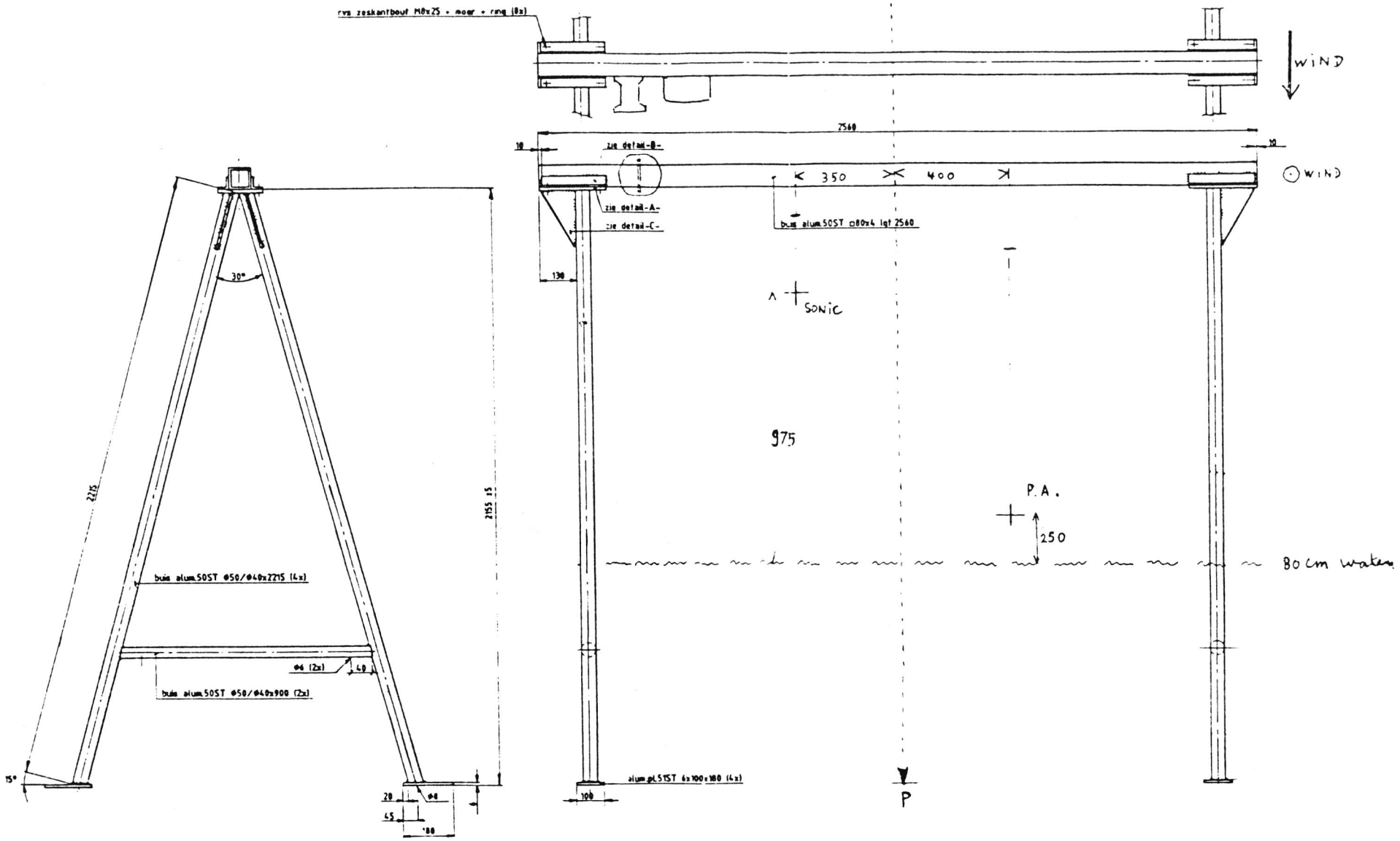

Figure 19: Trestle-frame with sonic anemometer and pressure anemometer.

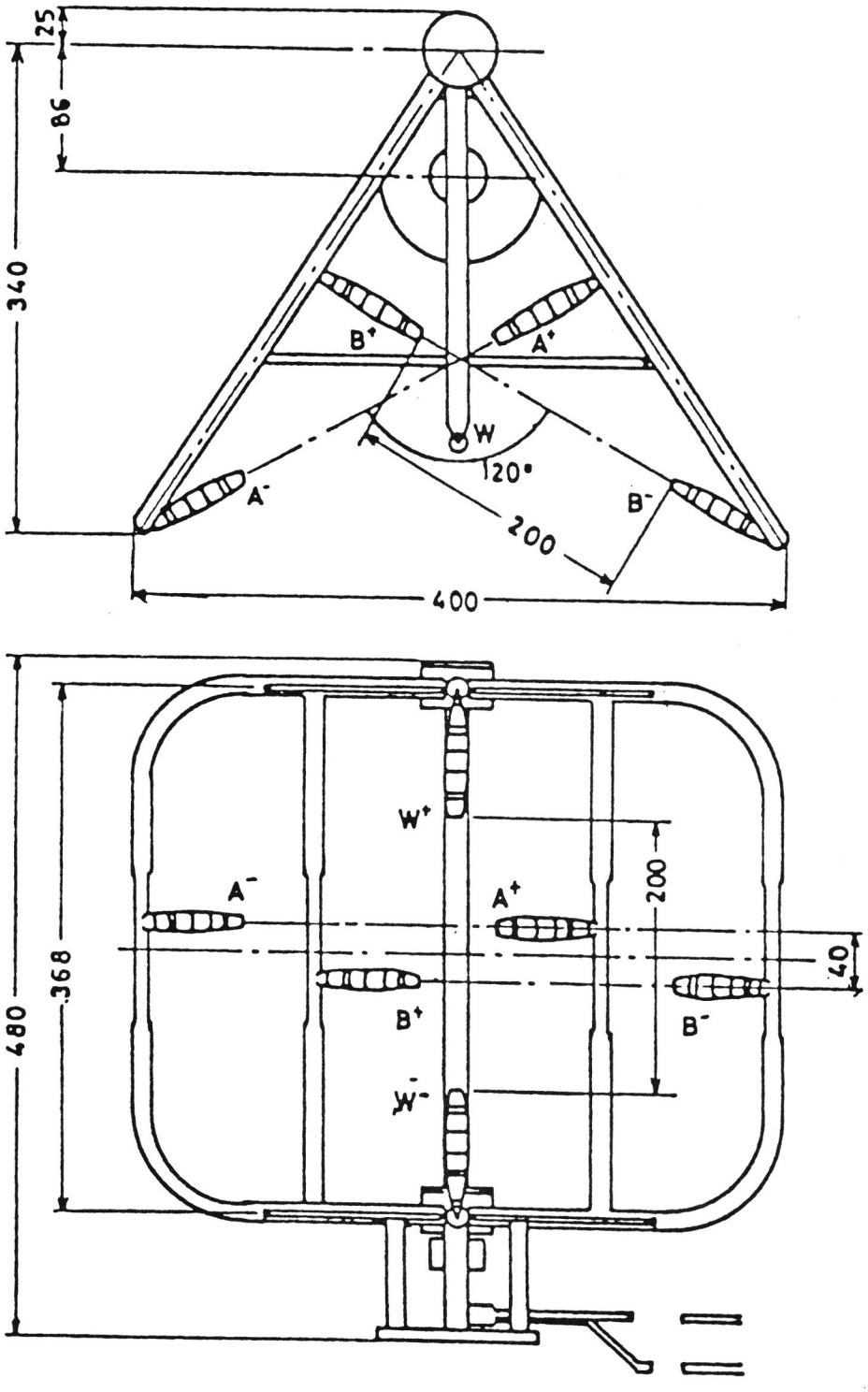

Figure 20: The sonic anemometer.

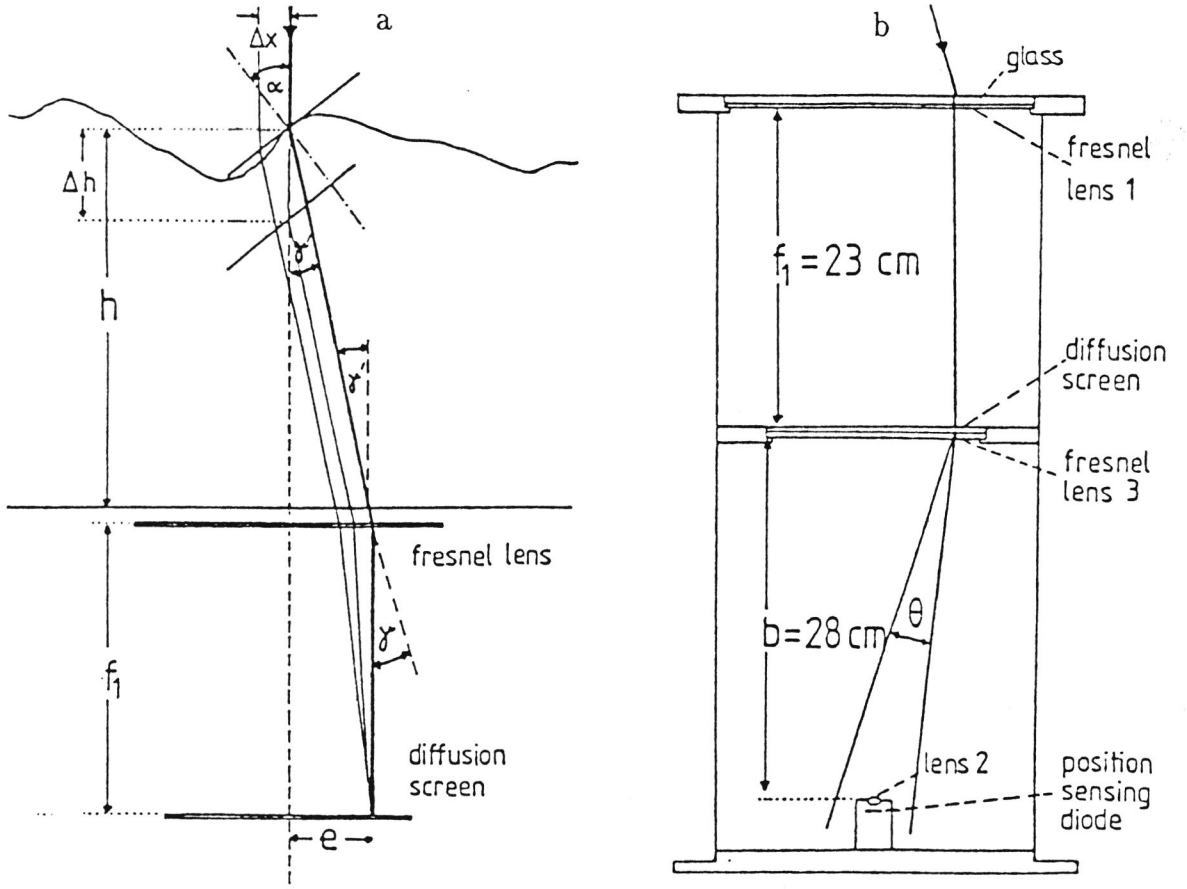

Figure 21: The Laser Slope Gauge (LSG) for wave slope measurements: a)refraction of the laser beam at the water surface and collection of the refracted beam by a Fresnel lens; b) cross-section of the submerged optical receiver of the LSG.

Reflective Stereo Slope Gauge (RSSG)

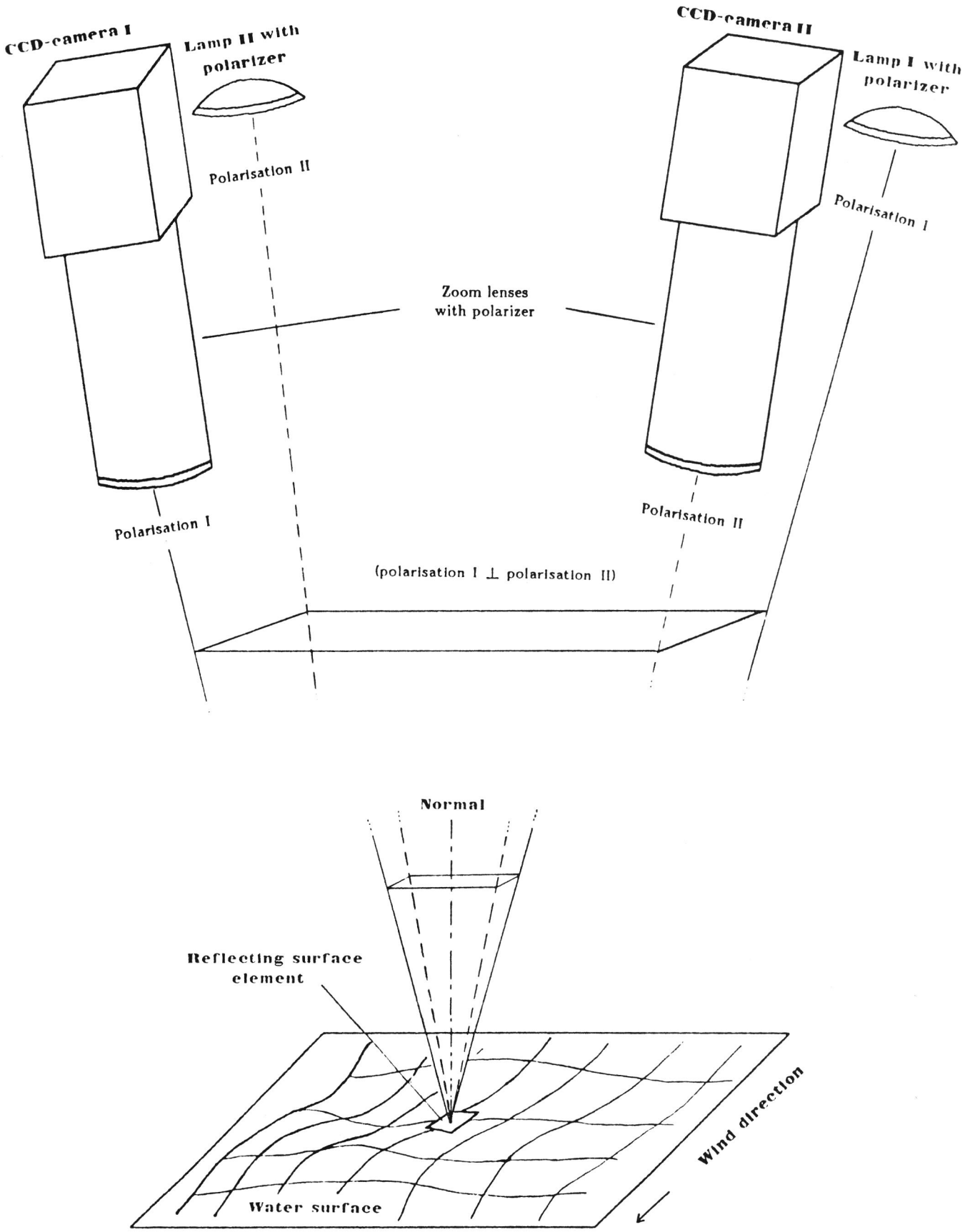

Figure 22: Outline of the Reflective Stereo Slope Gauge (RSSG).

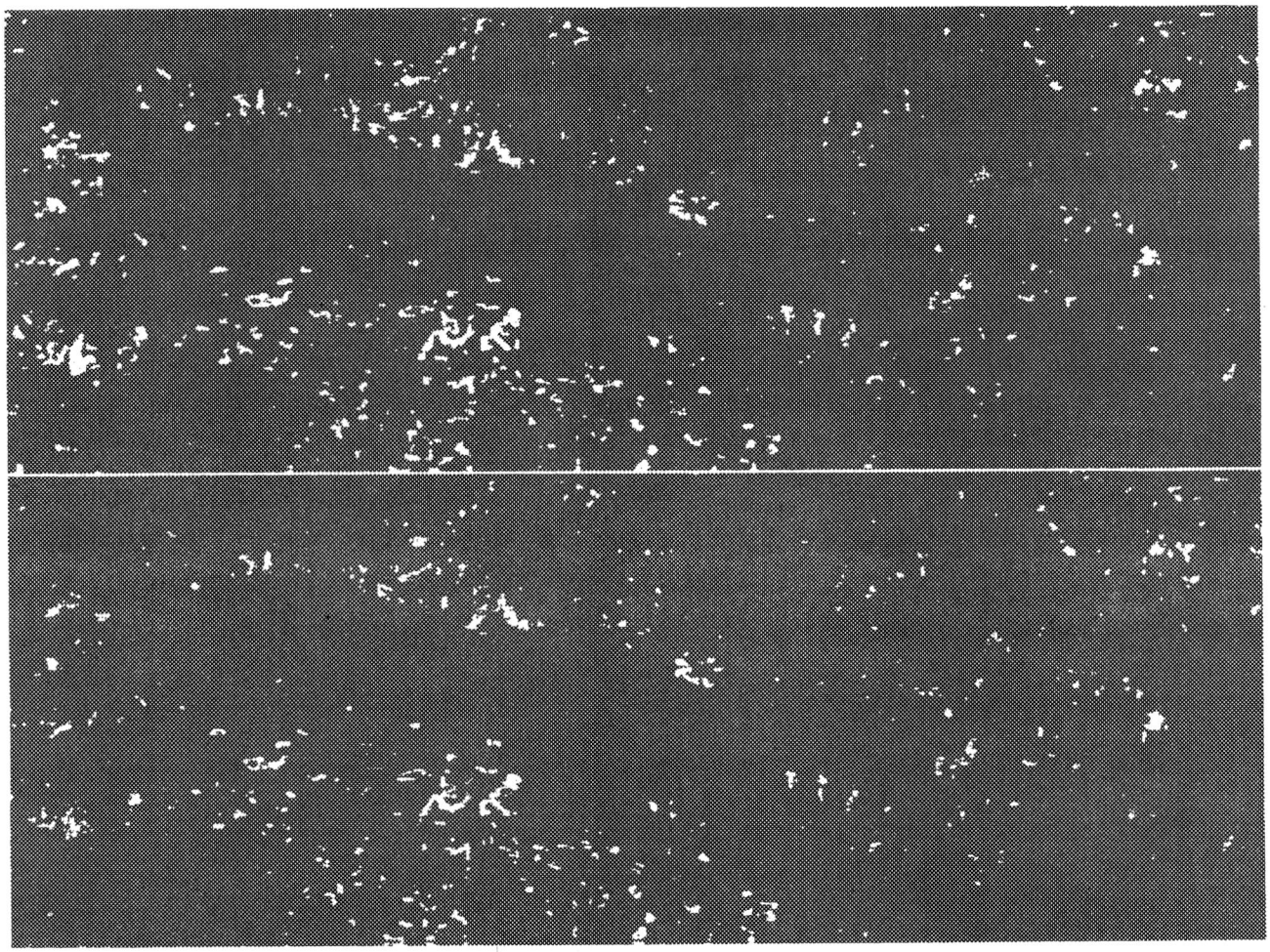

Figure 23: A typical stereo image of the specular reflexes from the water surface as observed by the RSSG. The left and right image are shown in the top and bottom images. The reflexes from both images are identical in shape and differ only in position, due to the different heights. Observed area on the water surface: 44 × 29 cm. The slope range is ± 3° along wind and ± 2° cross wind.

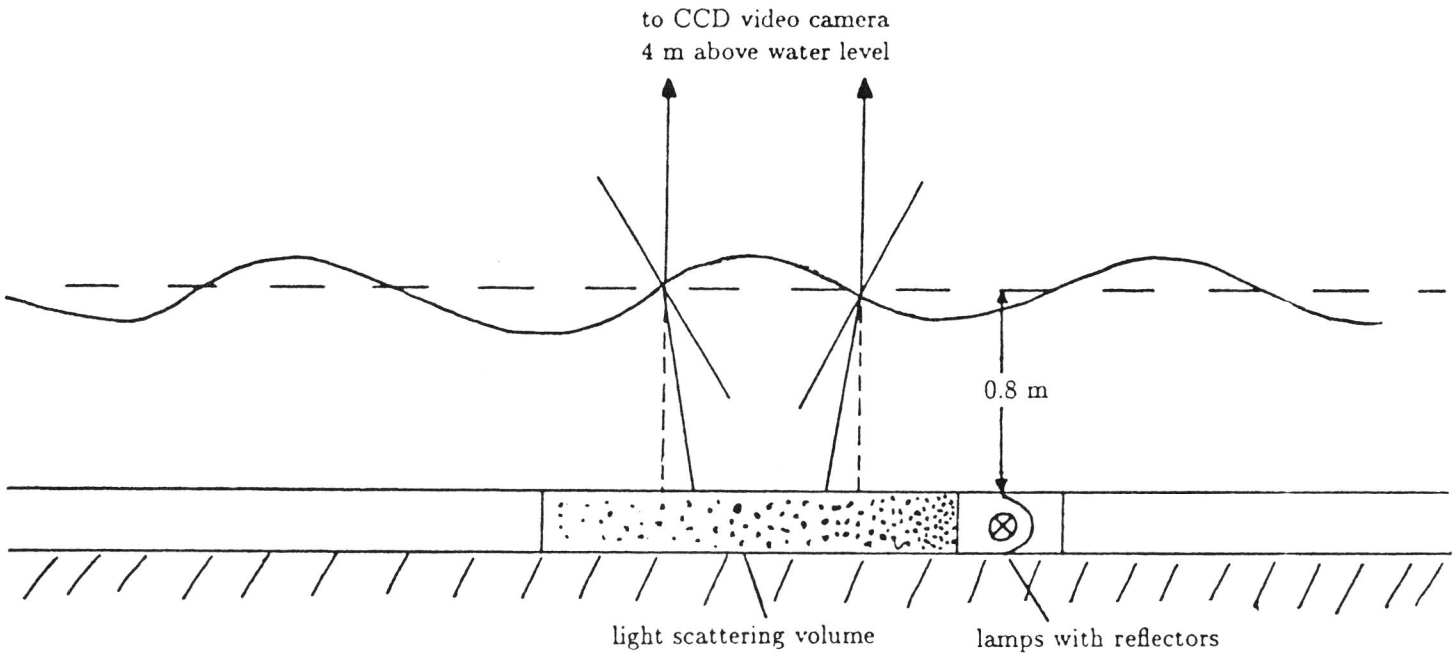

Figure 24: Outline of the Imaging Slope Gauge (ISG), shown in an along wind cross section. The submerged illumination system replaces a 0.25 × 2 × 2 m concrete slab at the bottom of the water tank.

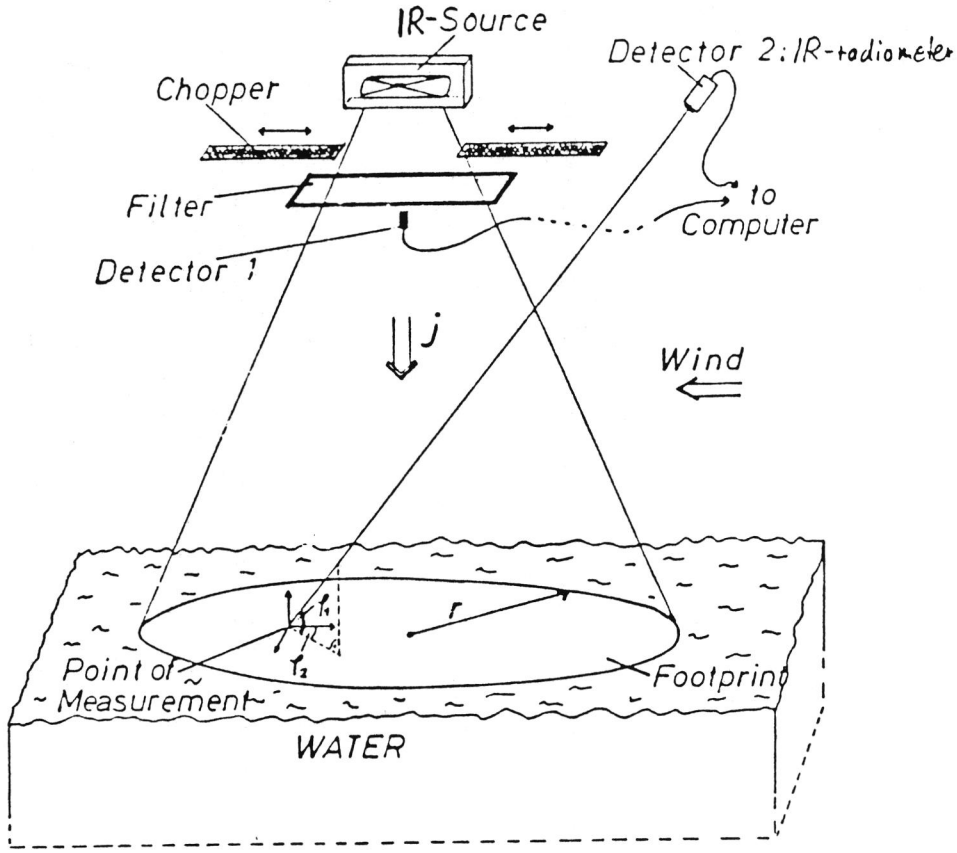

Figure 25: Outline of the Controlled Flux Technique (CFT), used to investigate the transfer processes across the aqueous boundary layer.

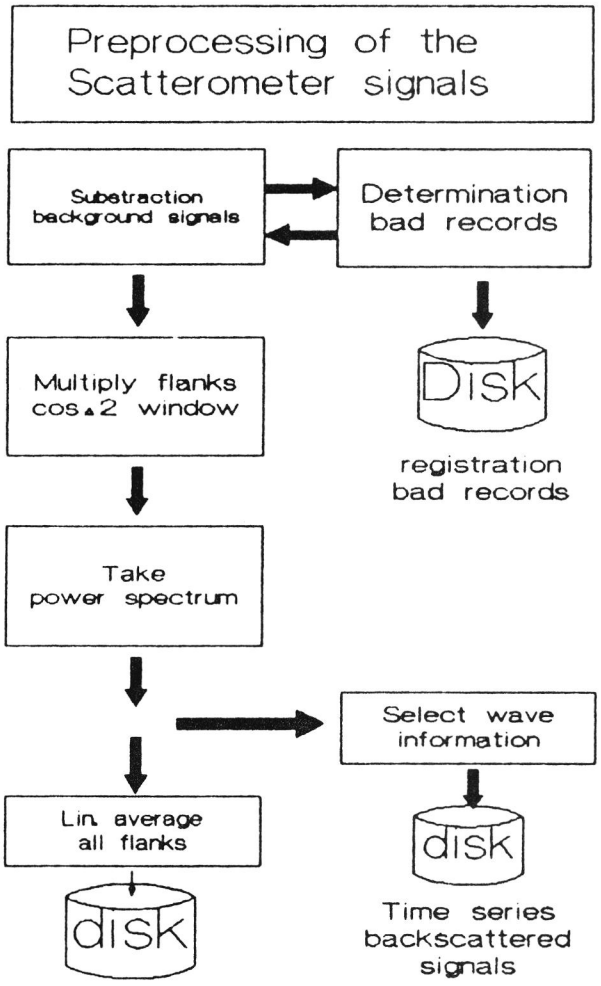

Figure 26: Schematic overview of the preprocessing of the scatterometer data.

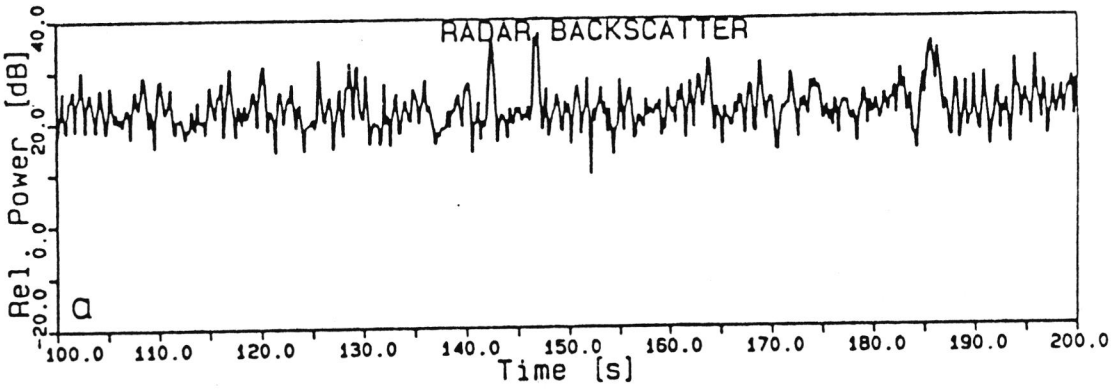

Figure 27: Time series of the microwavebackscatter at HH polarization and an incidence angle of 45°, looking upwind. The friction velocity was 0.37 m/s, U_{10} = 11.5 m/s. Note the strong modulation of the signals by the long waves (0.9 second period). The two spiky returns at t = 142 and t = 146.5 were caused by breaking waves (uncalibrated data).

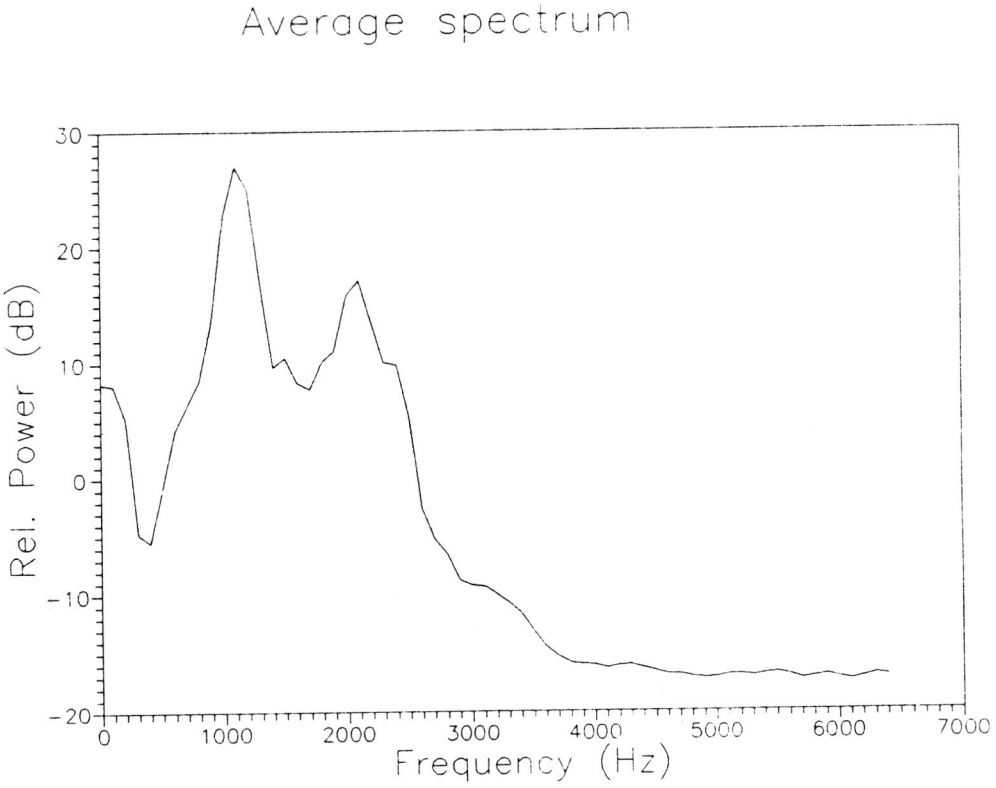

Figure 28: Typical example of the power spectrum of the beat signal of the radar . Frequency is proportional to range. The proportionality factor is 200 Hz/m. The reflections from the water surface are centered around f=1100 Hz. The returns at 2000 Hz are caused by secondary reflections from the tank, illuminated indirectly, via the water surface. Direct reflections from the tank walls and internal reflections of the radar have been effectively removed.

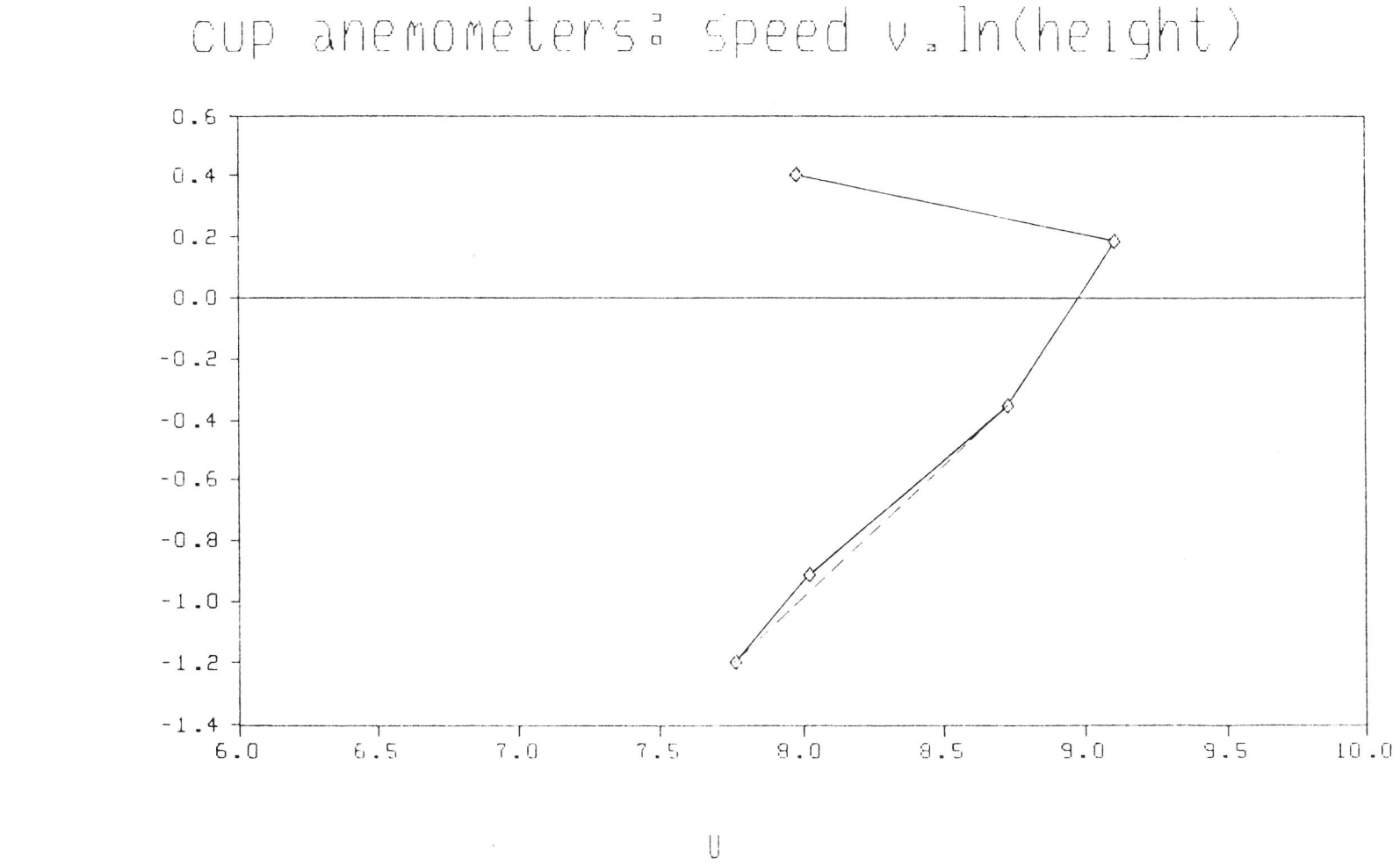

Figure 29: Example of cup anemometer results.

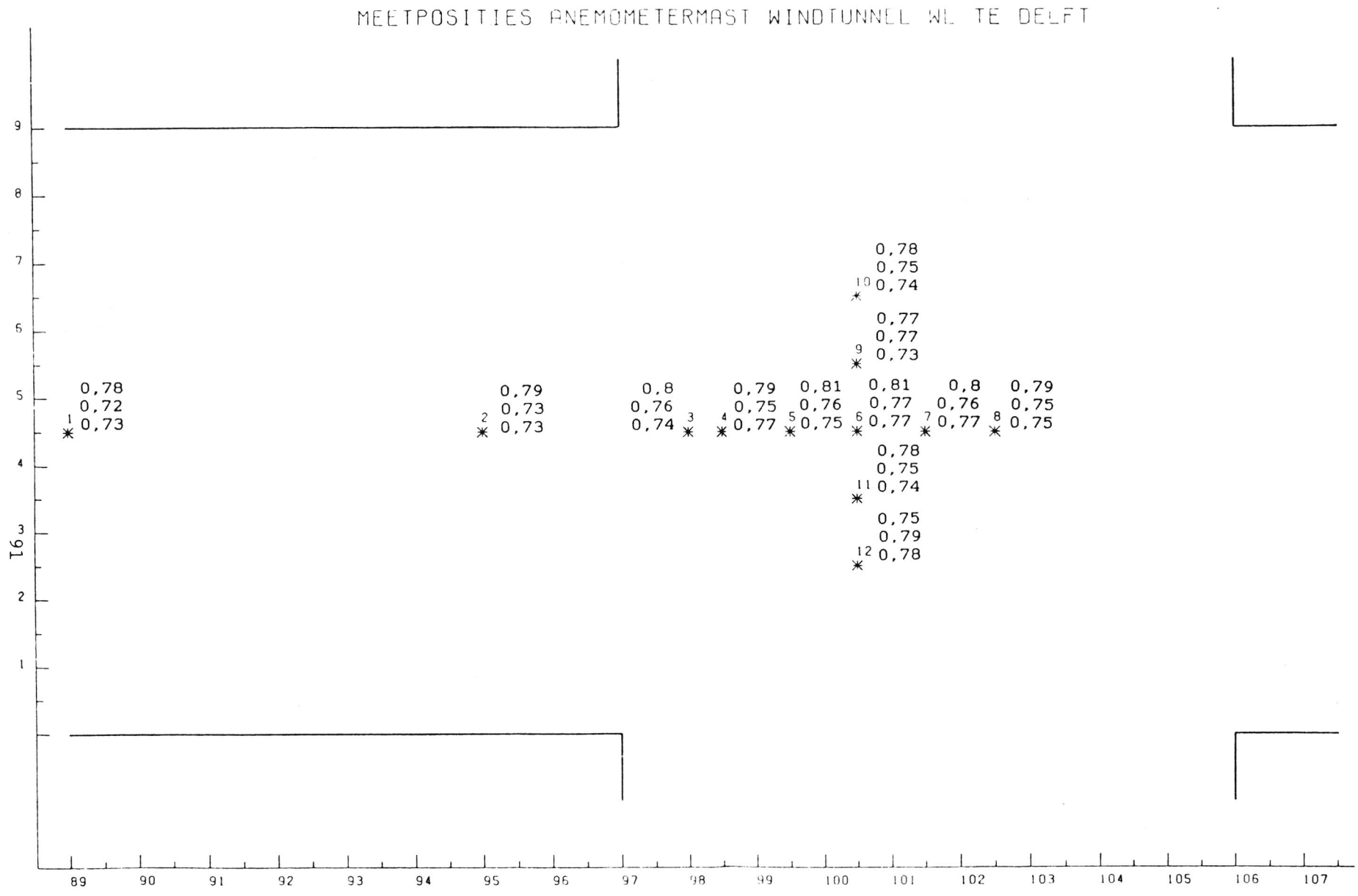

Figure 30: Cup anemometer data. The numbers are the readings of the instrument at 30 cm. above the water level and of cup 6. The top figures are for a nominal wind speed of 4 m/s, the middle ones for 8 and the bottom ones for 12 m/s.

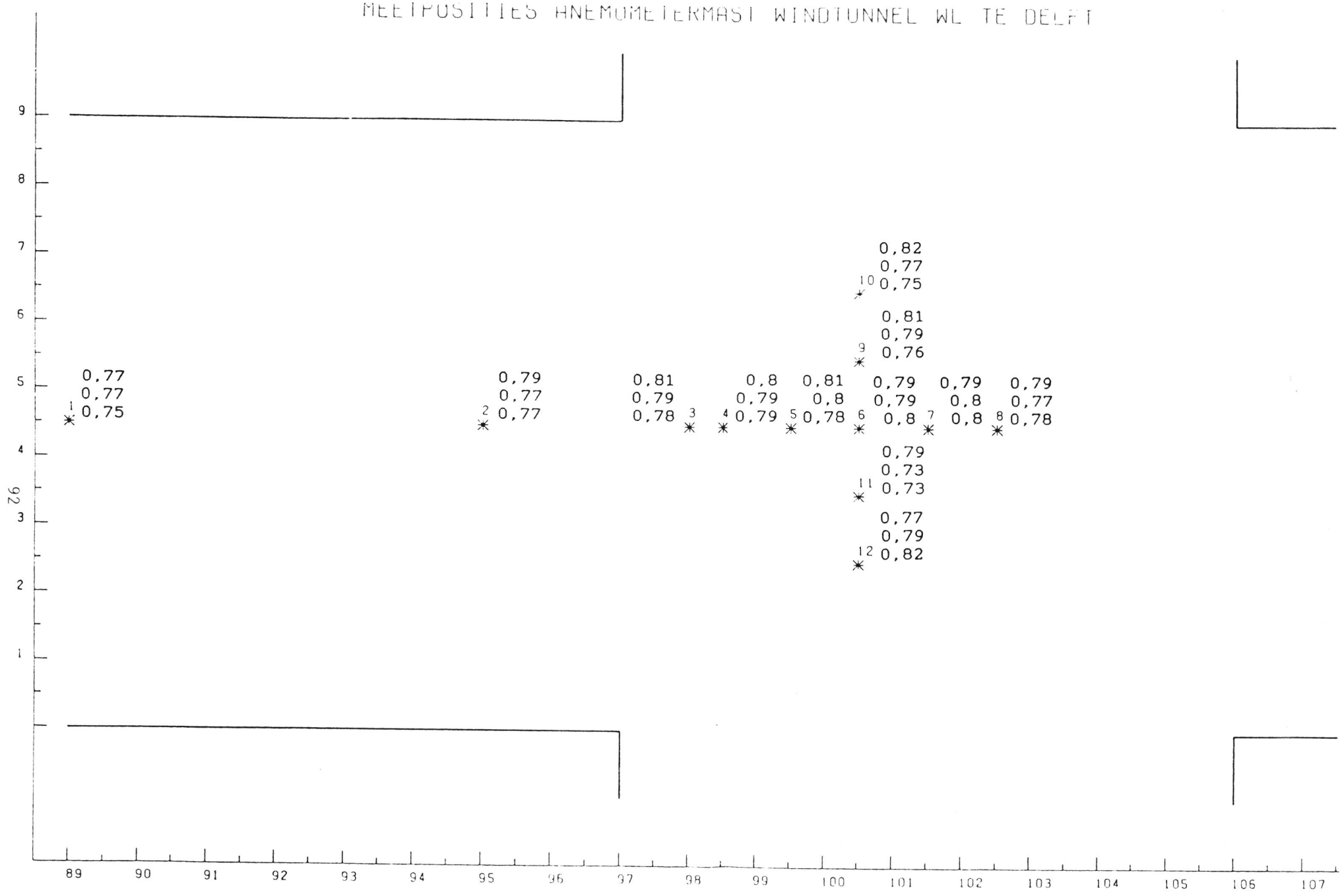

Figure 31: Cup anemometer data at 40 cm. above the water level.

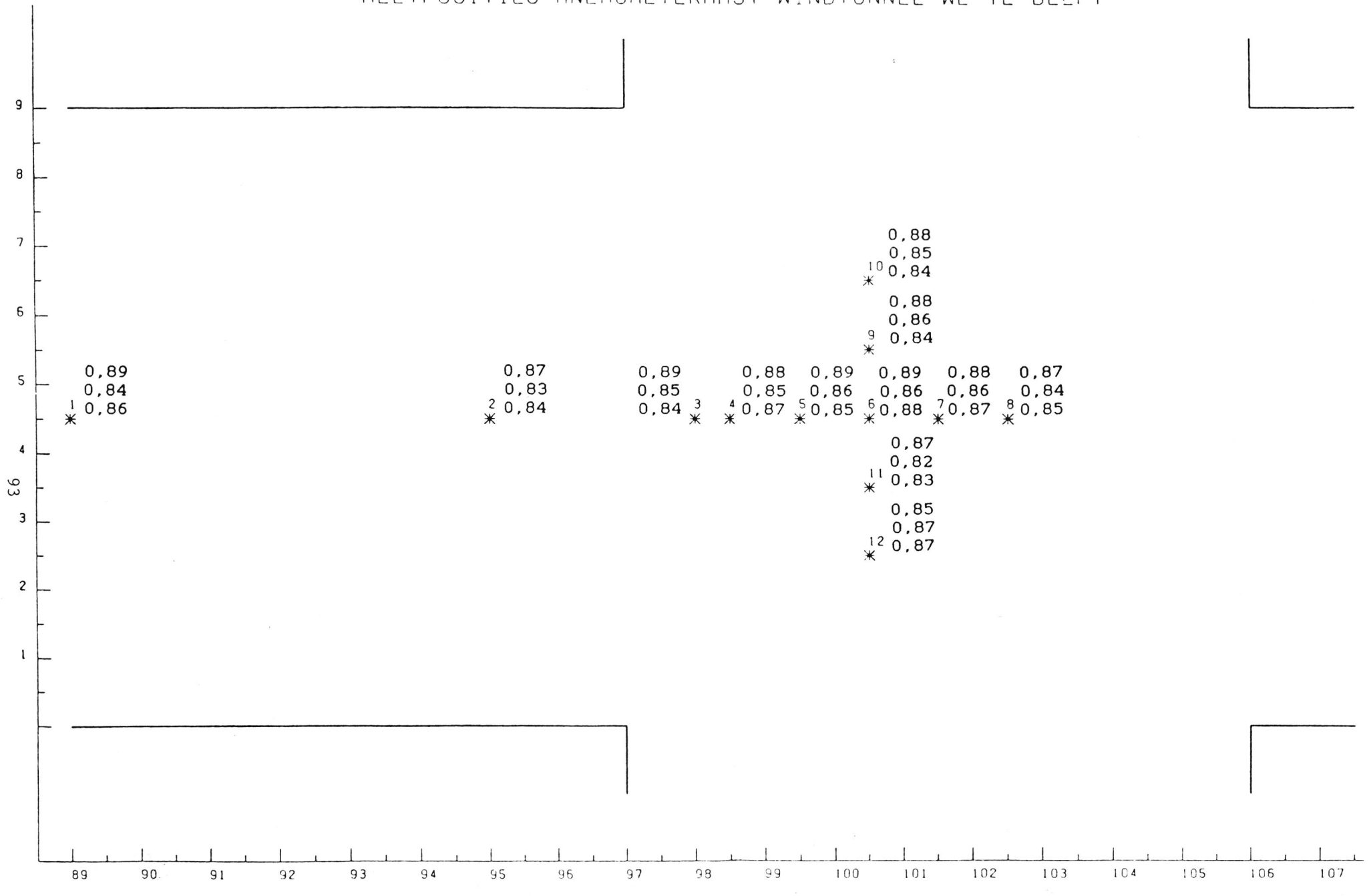

Figure 32: Cup anemometer data at 70 cm. above the water level.

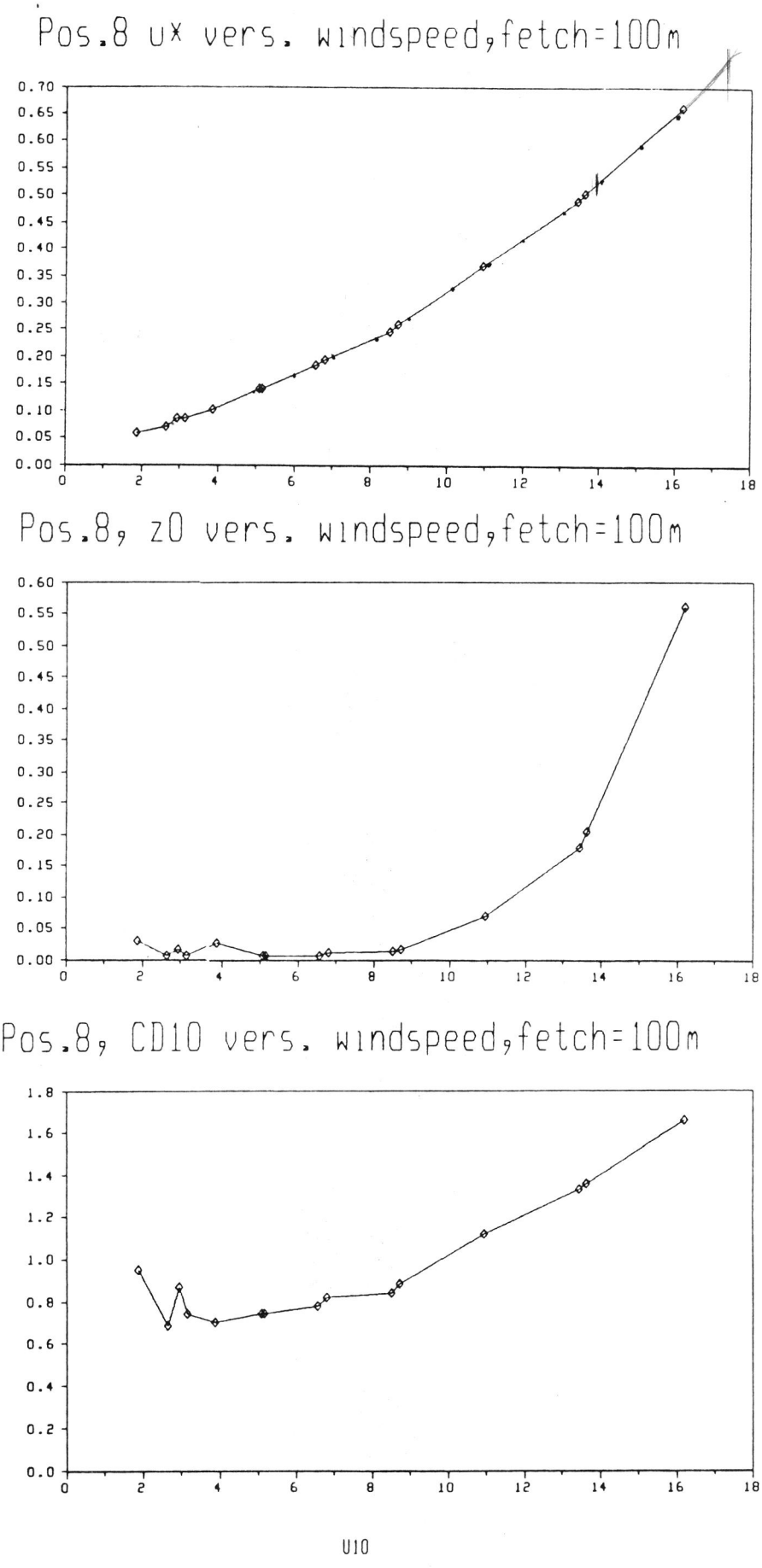

Figure 33: Dragcoefficient (C_D × 1000), roughness length (z_0, in mm) and friction velocity (u_*, in m/s) as a function of the wind speed, extrapolated to the 10 meter level (U_{10}, in m/s) at position 8. No radar dish present.

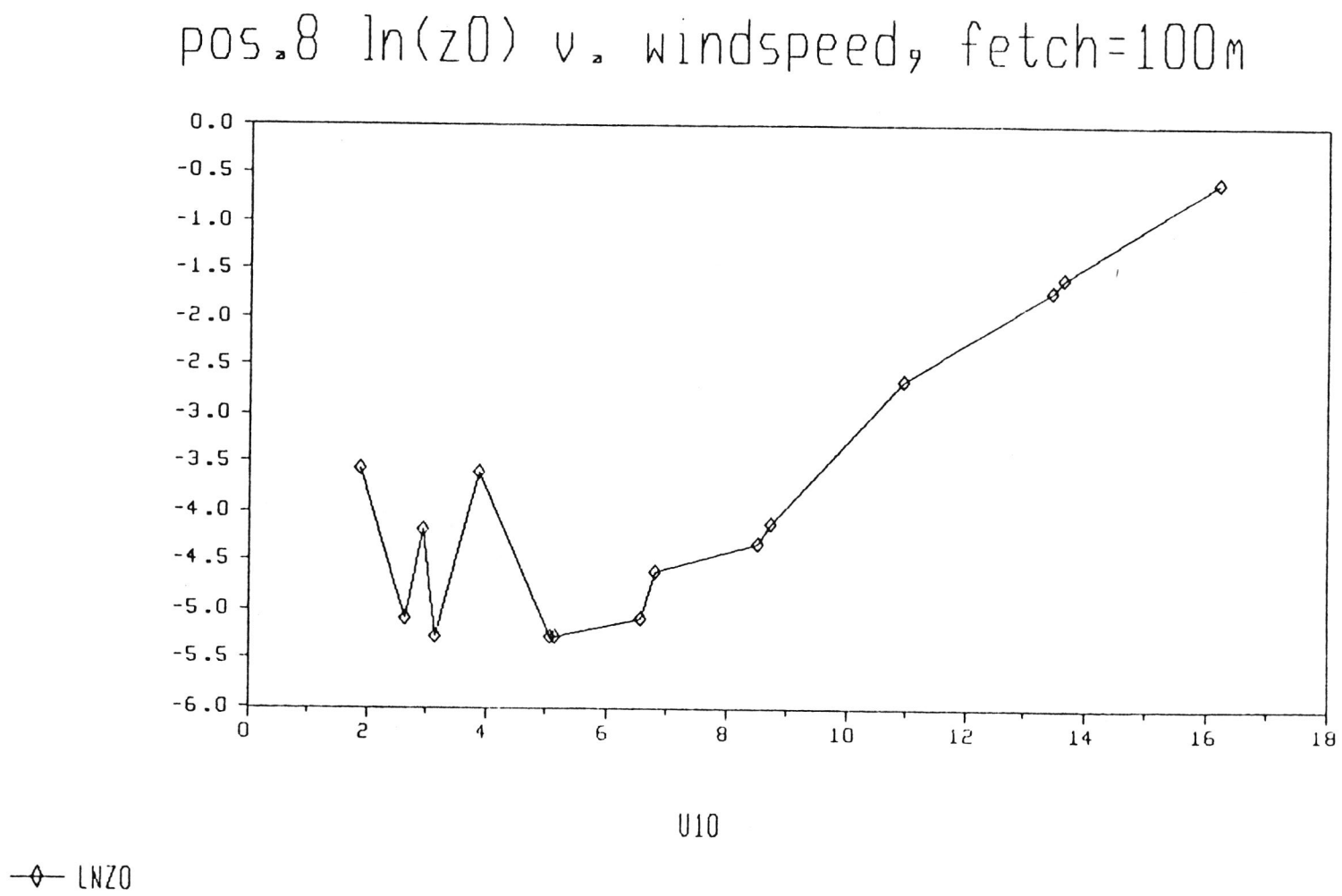

Figure 34: Logarithm of the roughness length as a function of the 10 meter wind speed.

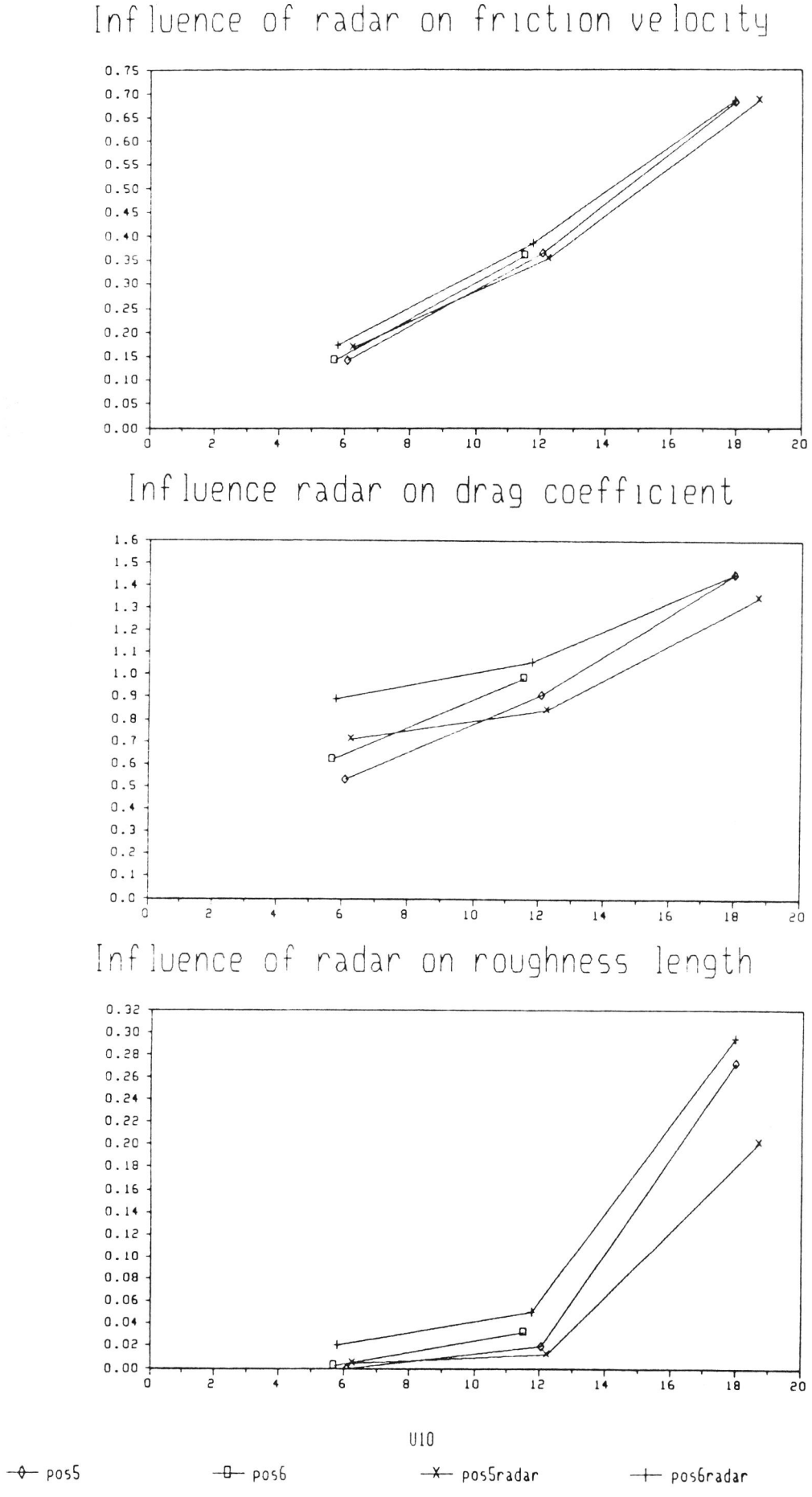

Figure 35: Effect of the radar dish at positions 5 and 6. Quantities as in figure 33.

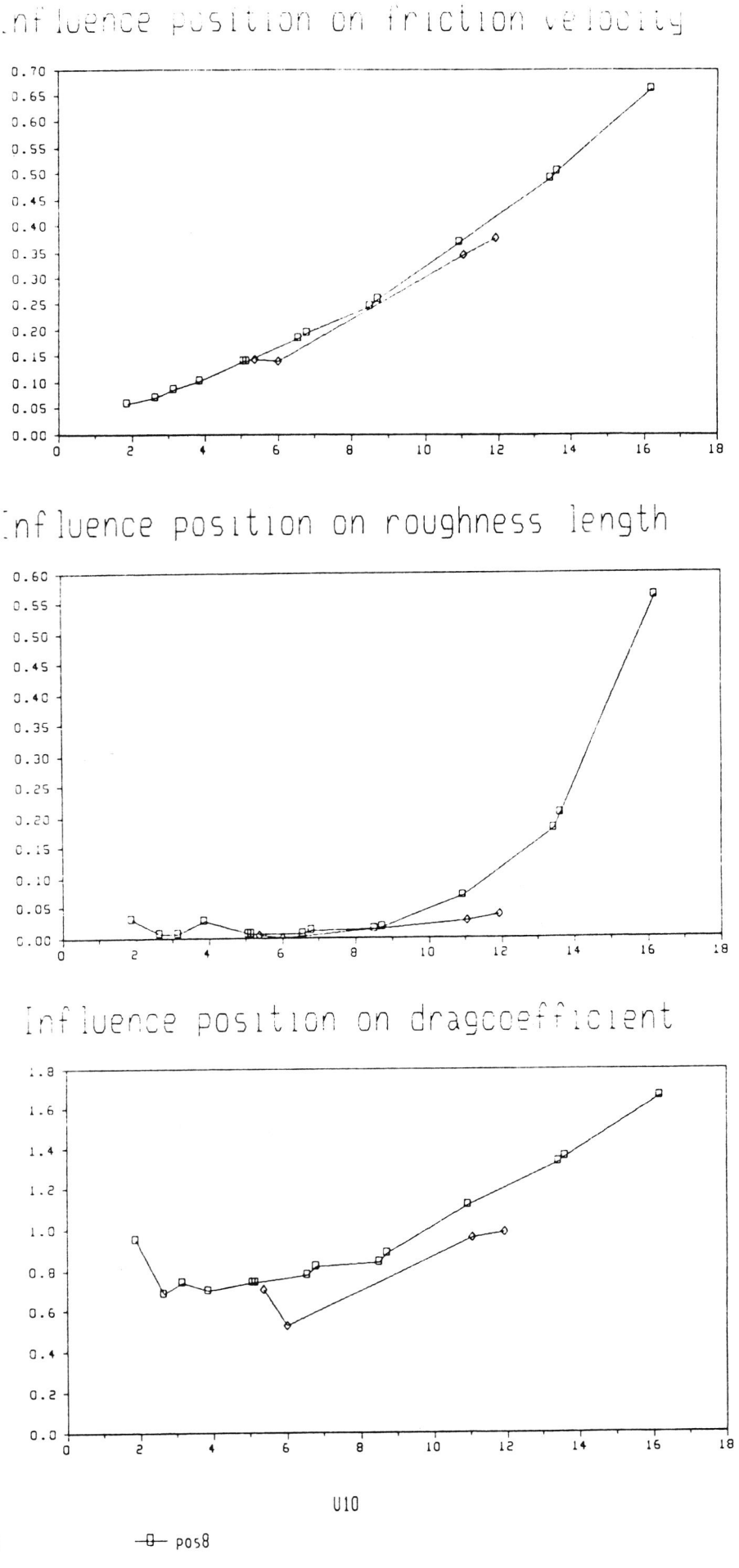

Figure 36: Change with position of the flow parameters for positions 6 (radar footprint) and 8.

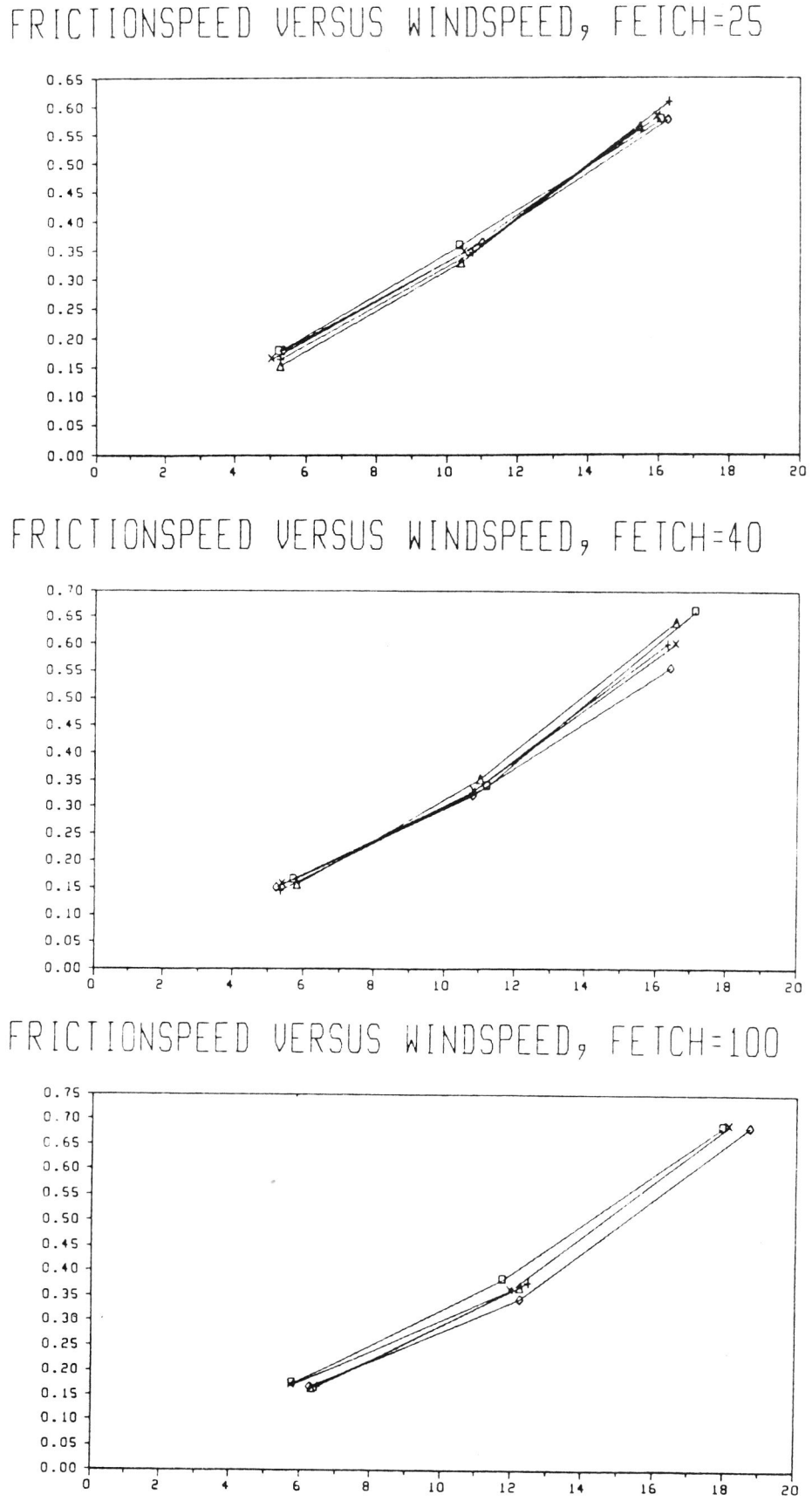

Figure 37: Change of the friction velocity with wind speed and position for several fetches.

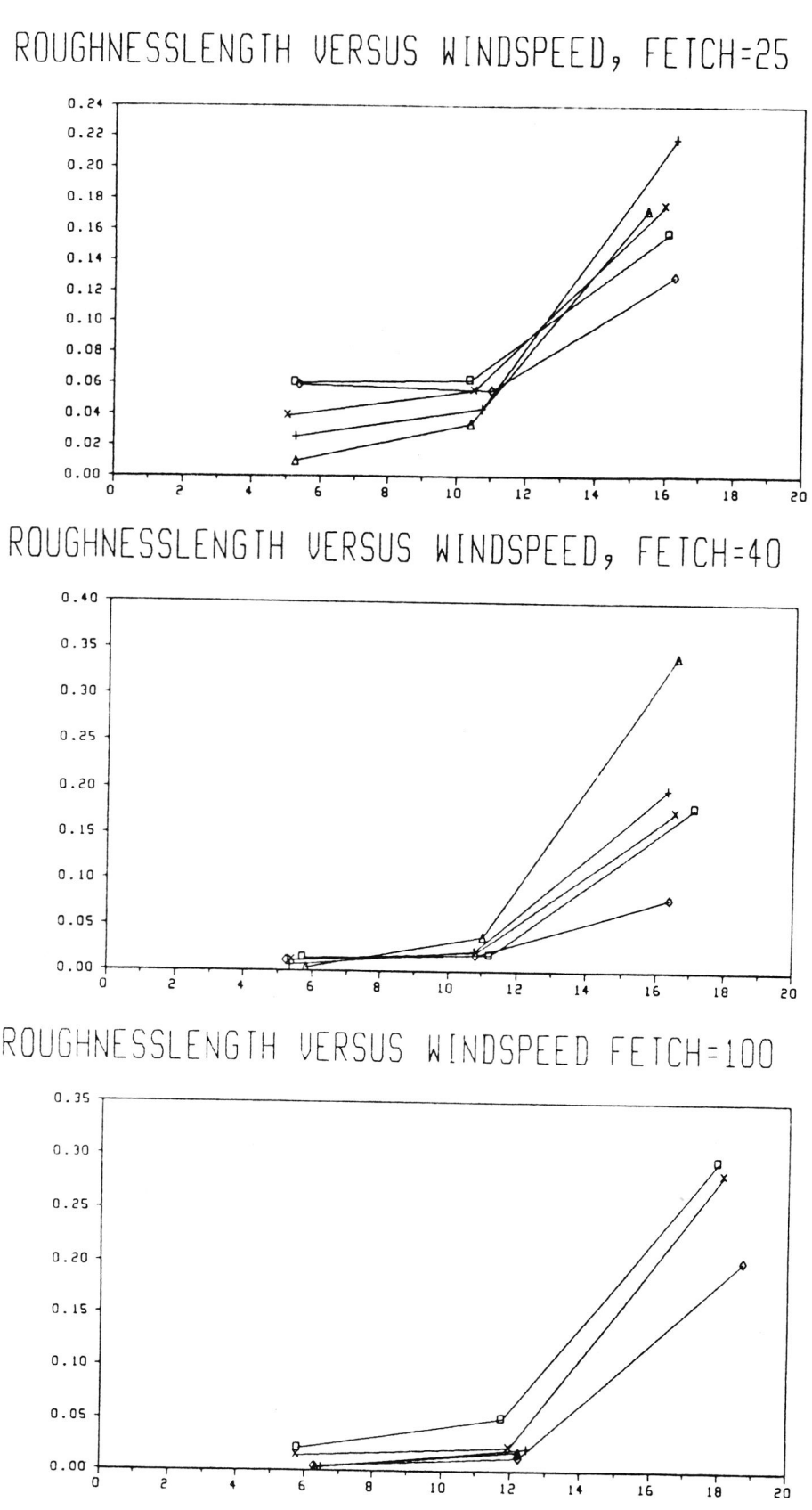

Figure 38: As figure 37, for the roughness length.

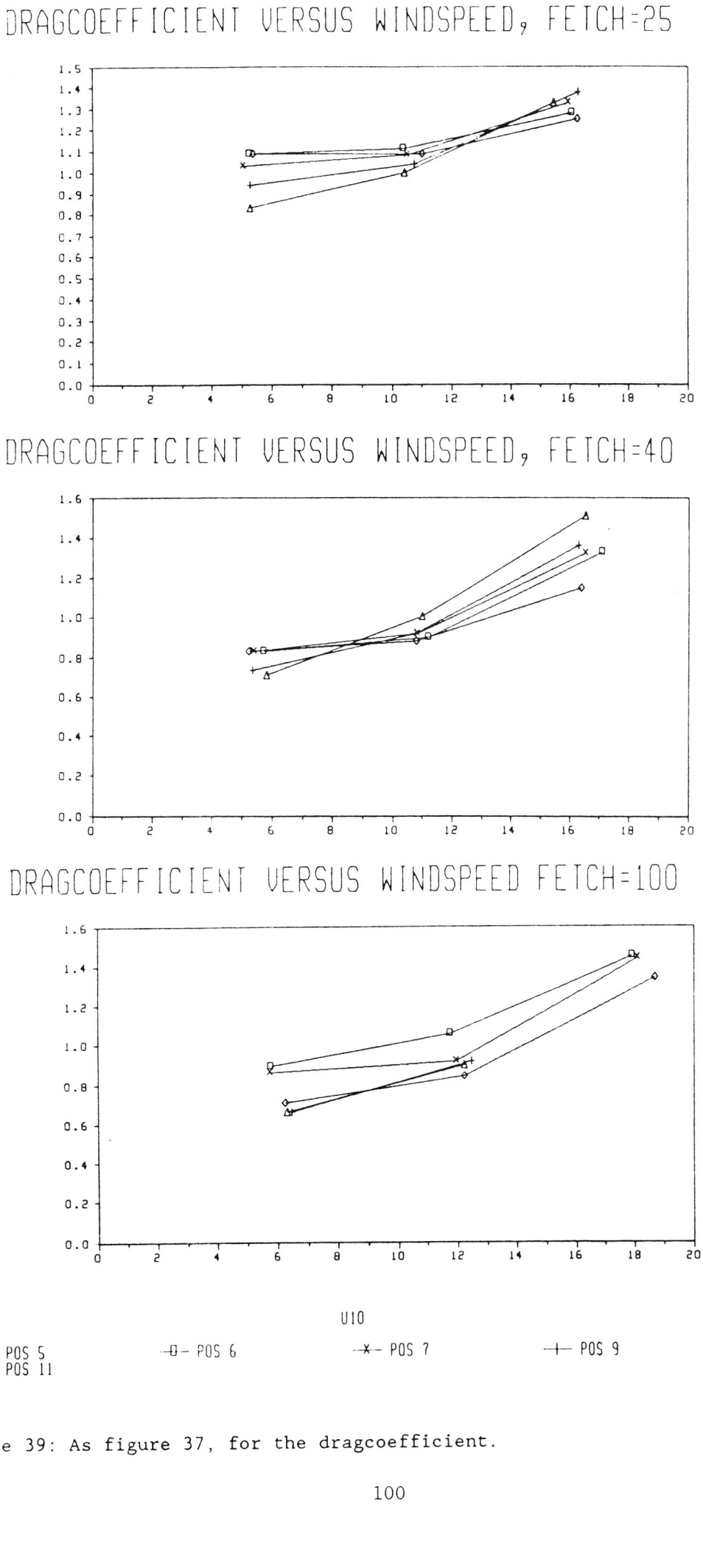

Figure 39: As figure 37, for the dragcoefficient.

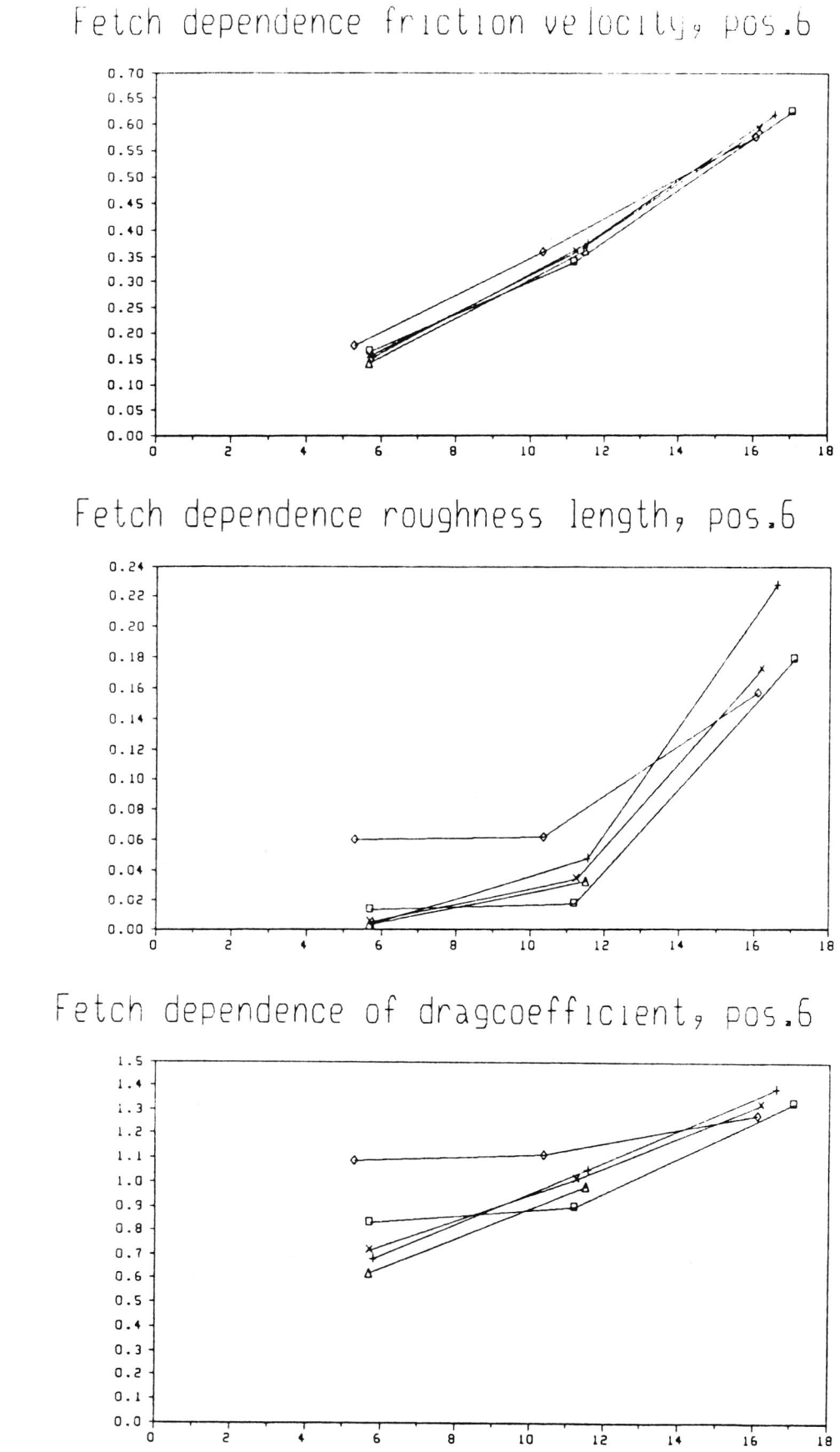

Figure 40: Fetch dependence of the flow parameters for position 6 (radar footprint).

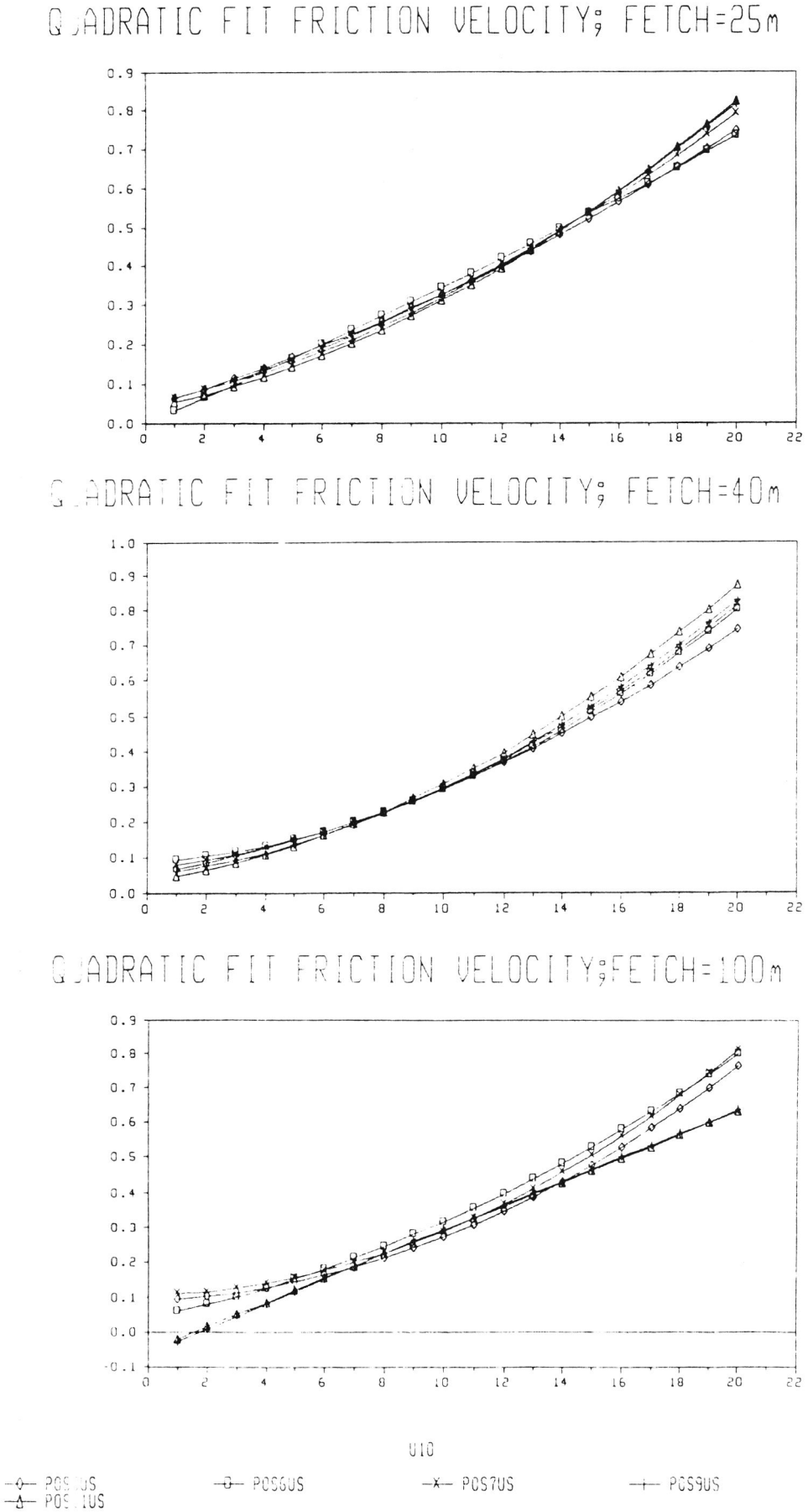

Figure 41: Quadratic fit to the friction velocity at various positions and fetches.

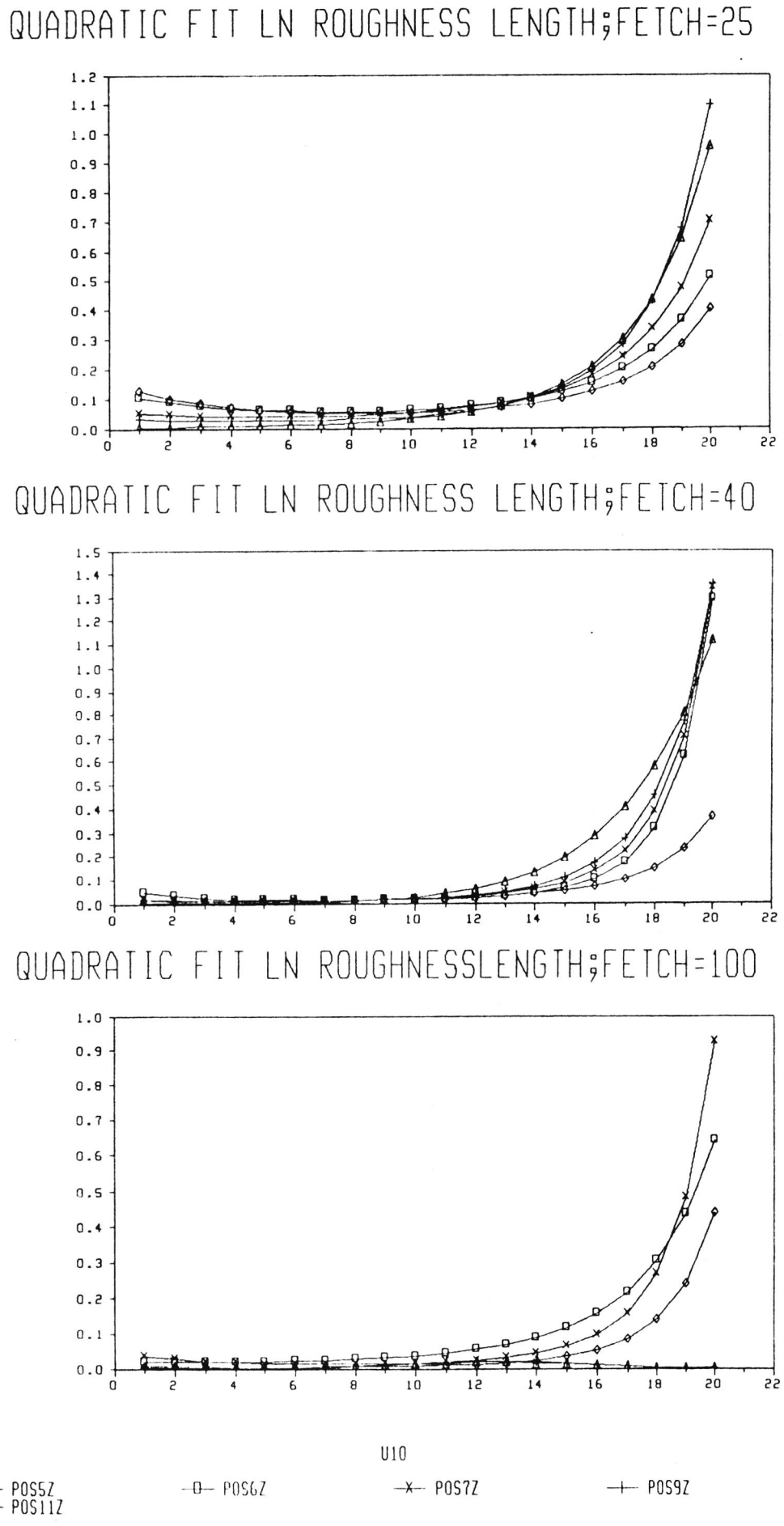

Figure 42: As figure 41, for the logarithm of the roughness length.

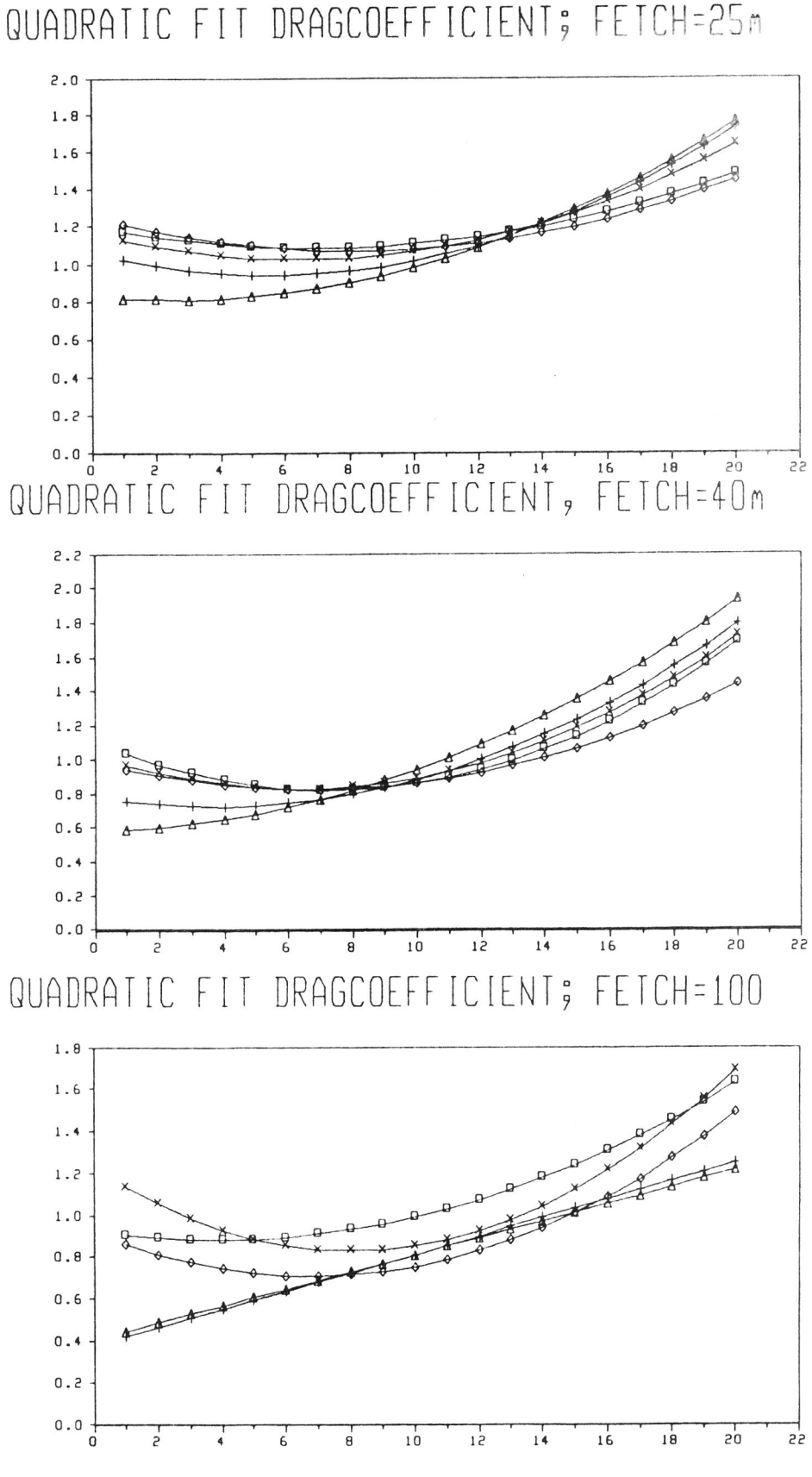

Figure 43: As figure 41, for the dragcoefficient.

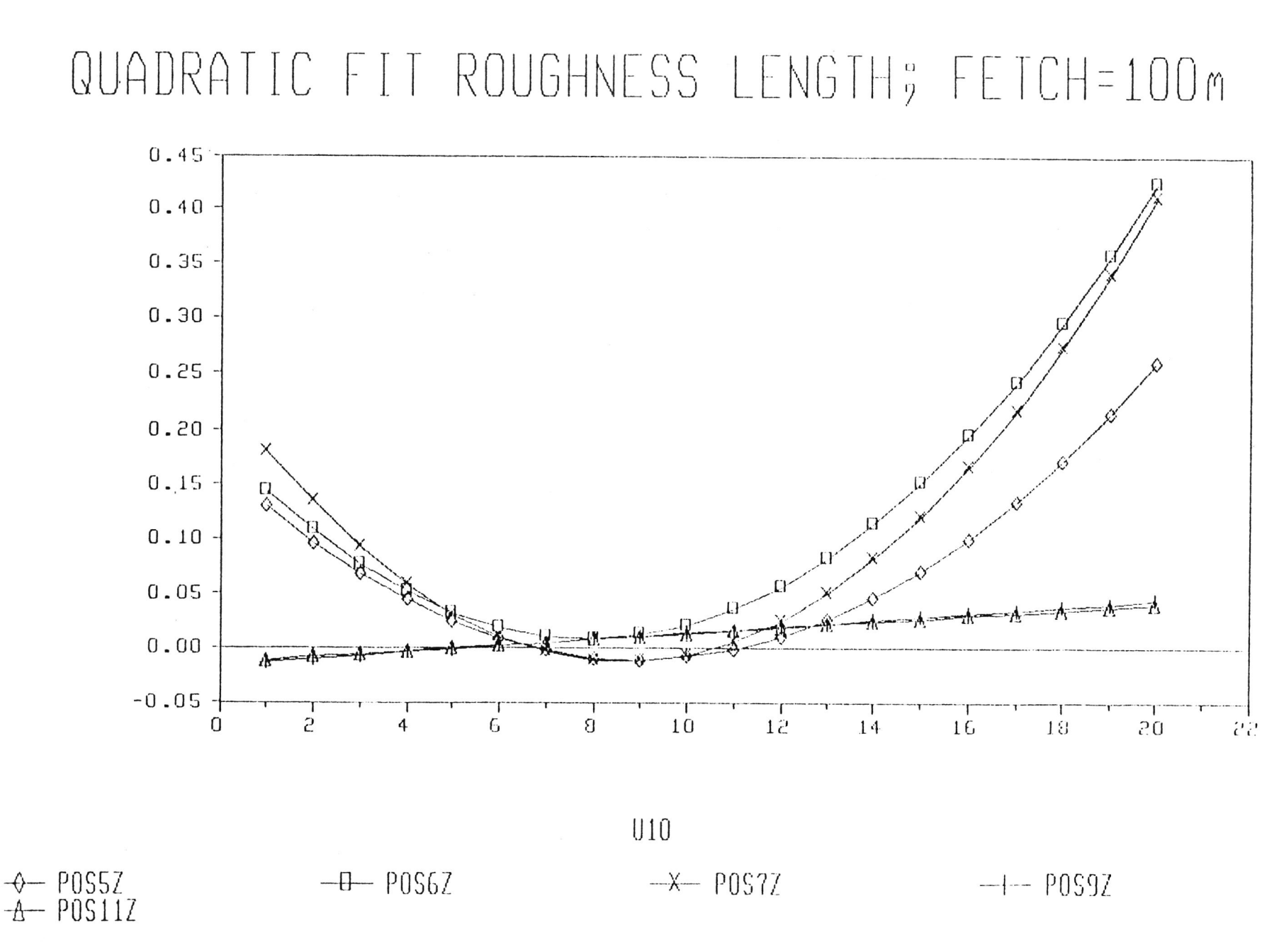

Figure 44: As figure 41, for the roughness length and a single fetch.

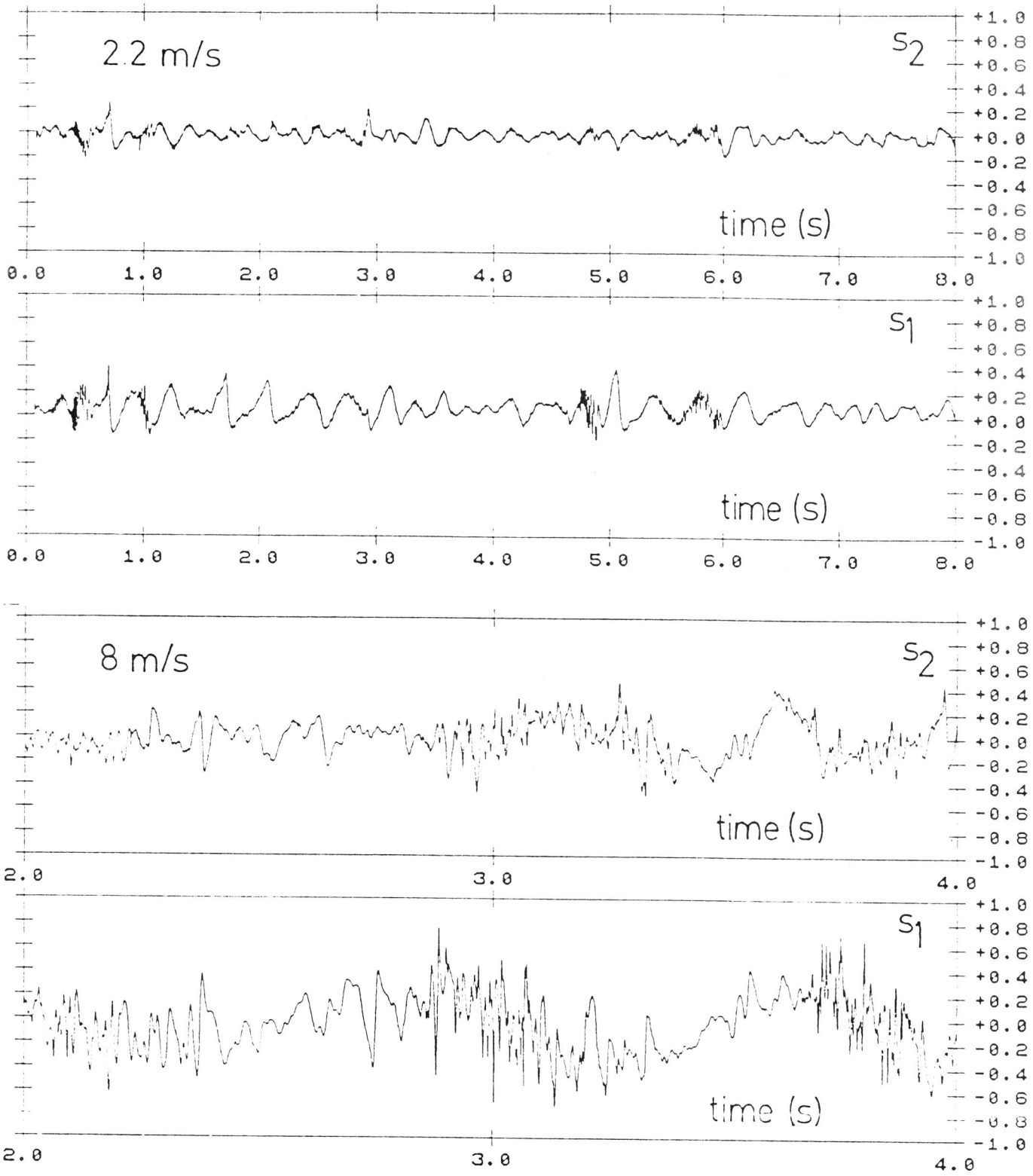

Figure 45: Two typical time series of the along wind slope sl and the cross wind slope s2 at 2.2 and 8 m/s wind, as measured with the LSG; positive slopes are directed against the wind.

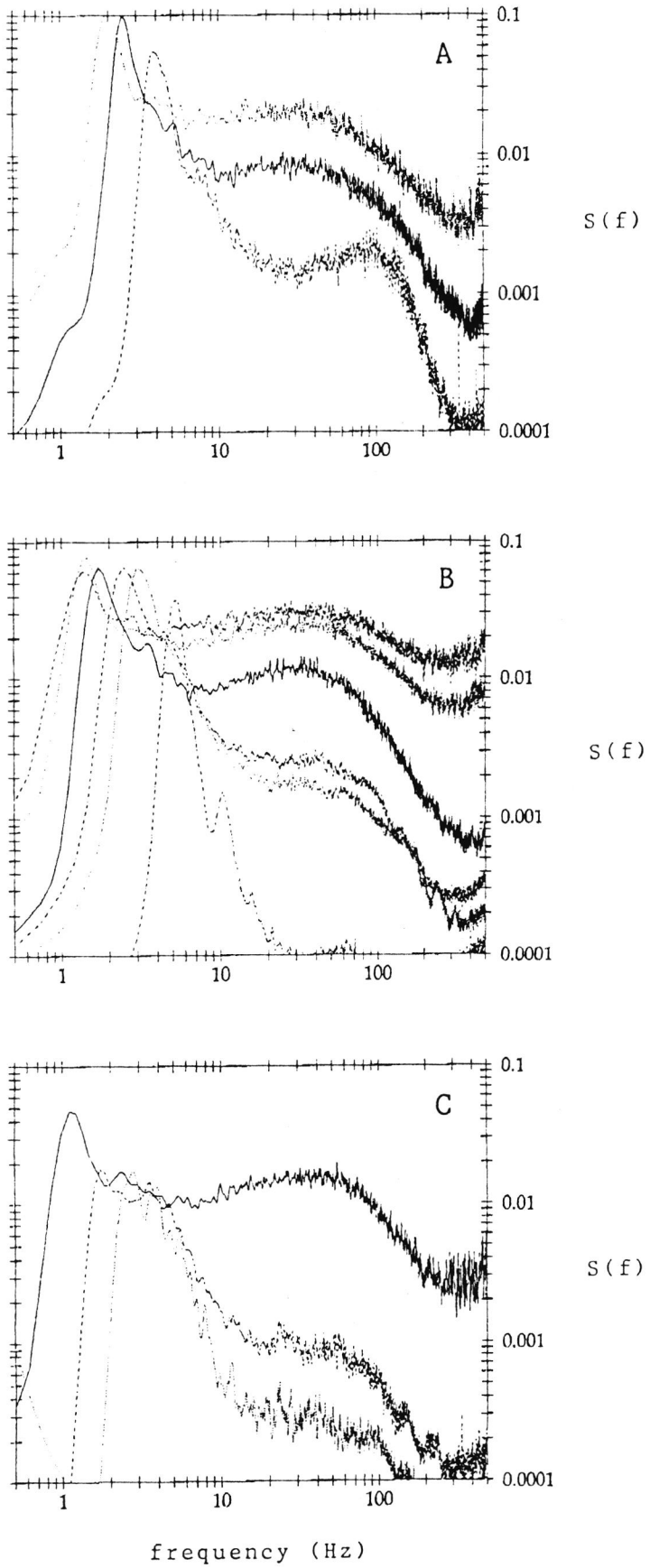

Figure 46: Wind speed dependence of the frequency spectra of the wave slope determined with the LSG at a) 15, b) 30 and c) 90 meter fetch.

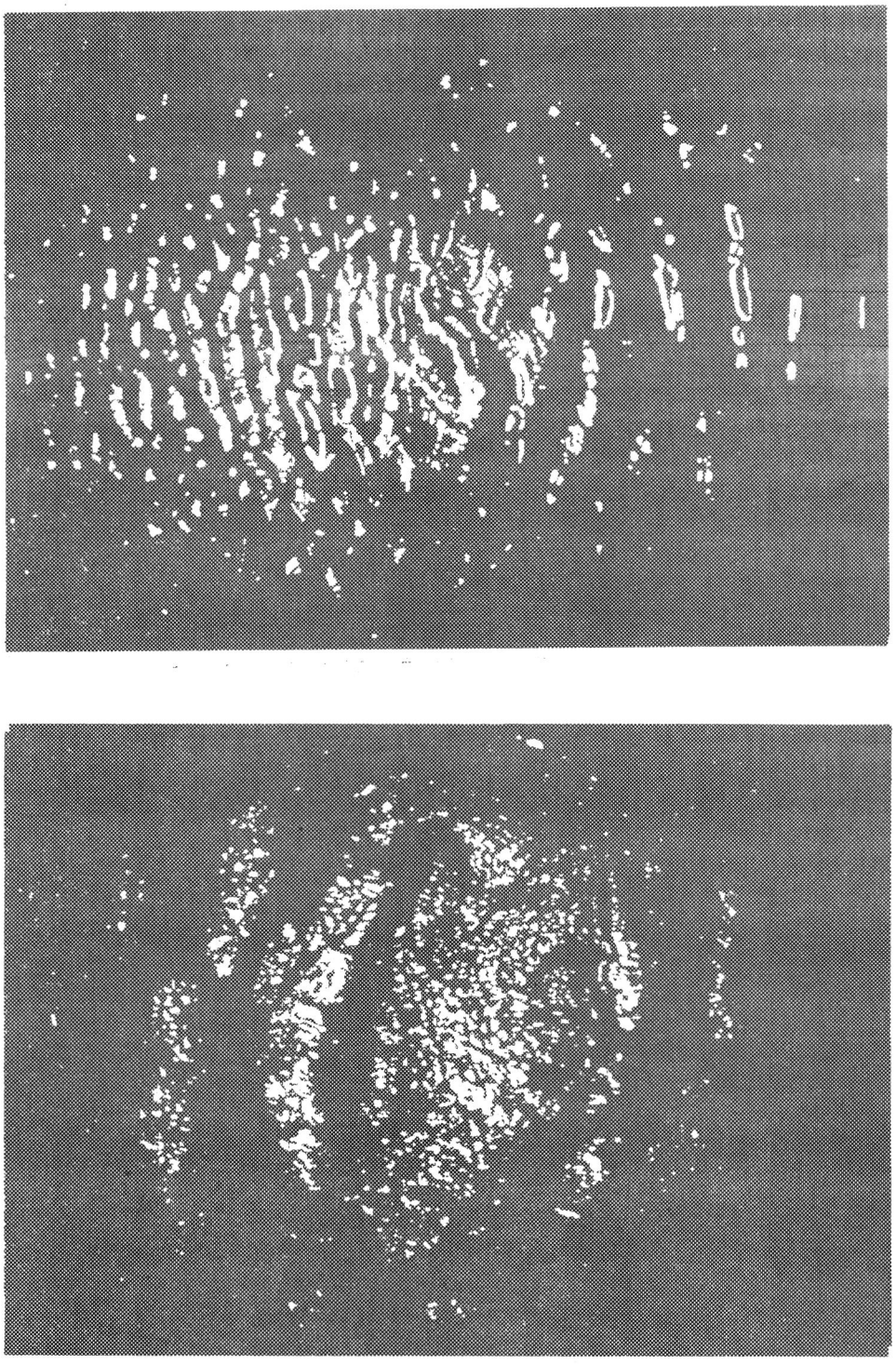

Figure 47: Photographs of the specular reflections from the water surface as seen by the reflective slope gauge (RSG) at 4 m/s (skewed view) and 12 m/s (perpendicular view). Image sector approximately 1.5 × 2 m.

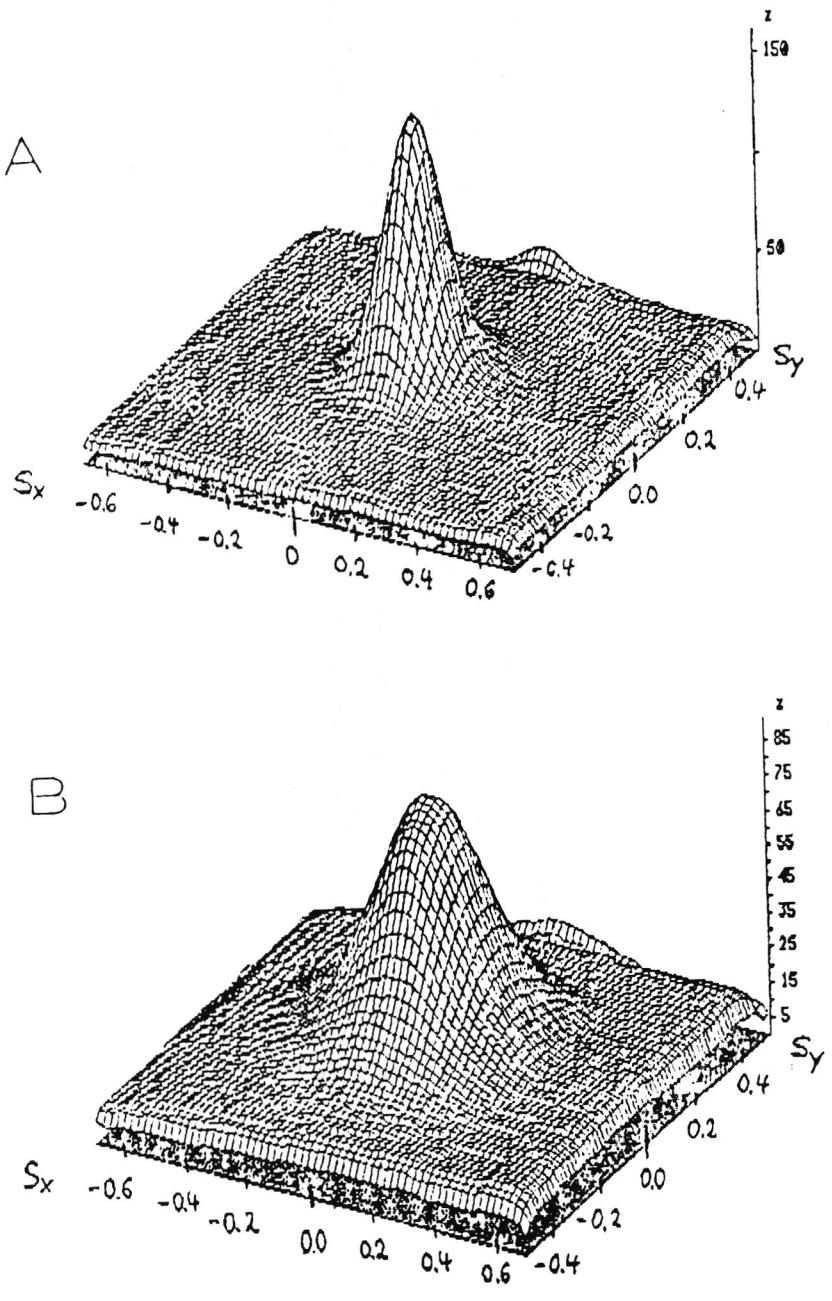

Figure 48: Two-dimensional slope distribution (uncorrected) as obtained with the RSG by addition of 2048 reflex images as shown in fig.47 at a) 3.1 m/s and b) 8.0 m/s wind speed, both at 90 m. fetch.

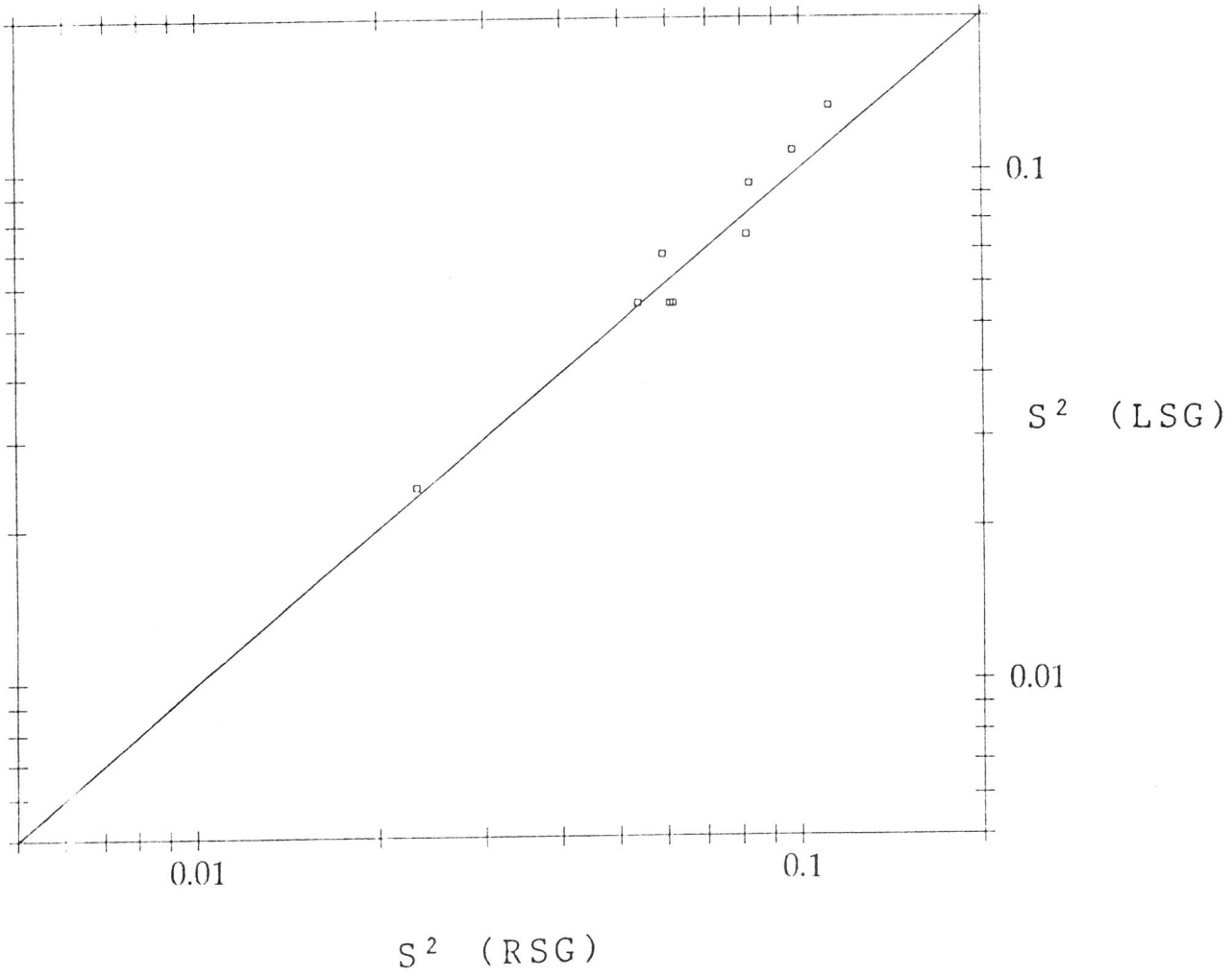

Figure 49: Comparison of the mean square wave slope determined with the RSG and the LSG.

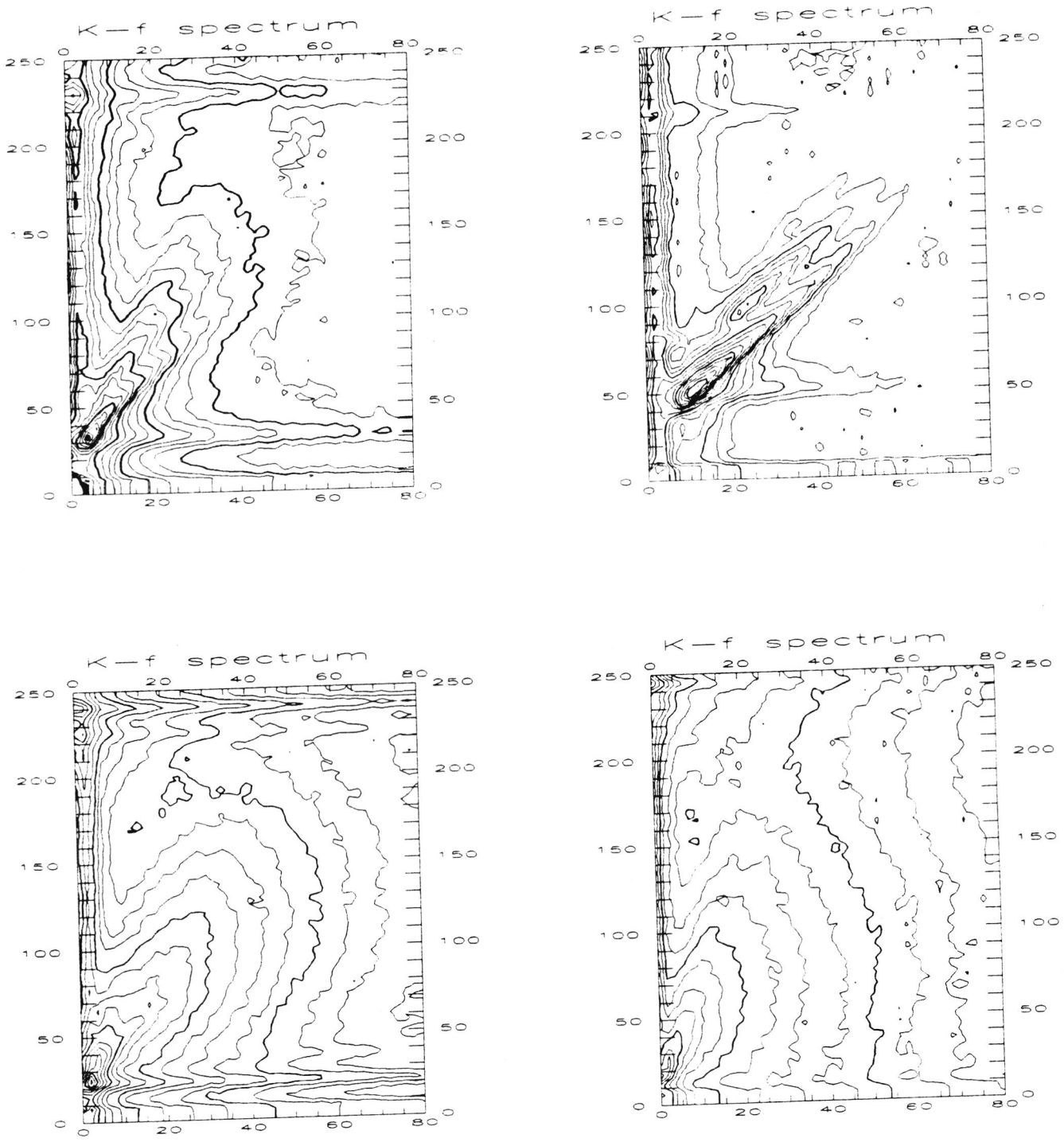

Figure 50: Wavenumber-frequency spectra calculated from ISG image sequences at 40 m. fetch. Wind speeds: a) 1.9, b) 3.1, c) 8 and d) 12 m/s. Each shading covers a decade.

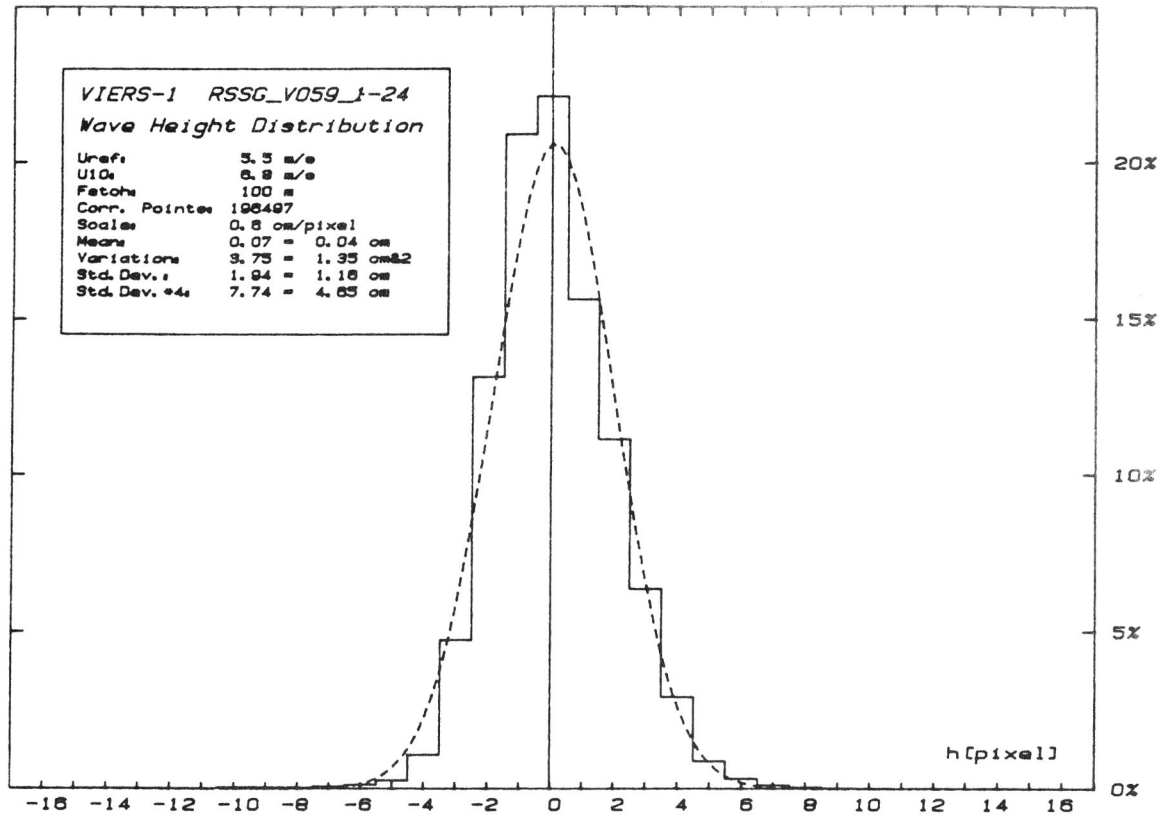

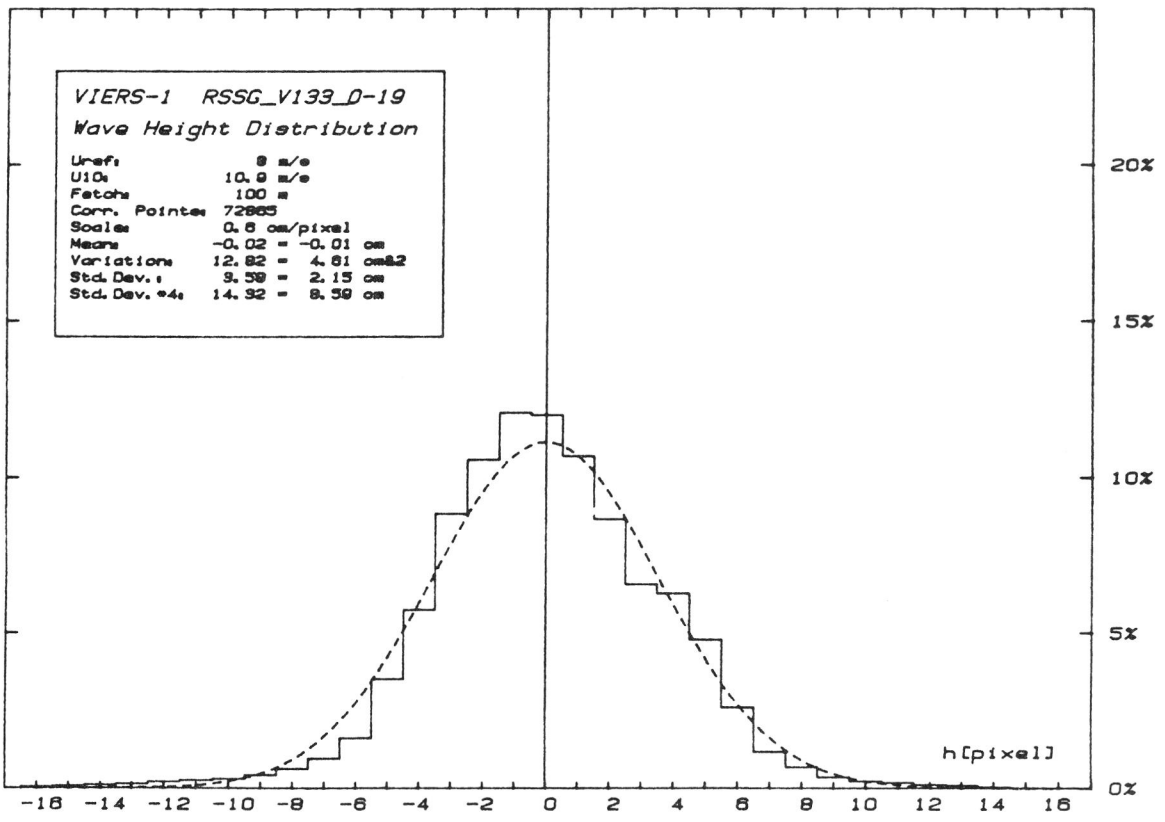

Figure 51: Wave height distributions derived from stereo images with the RSSG at a) 5.5 and b) 8 m/s reference wind speeds and a fetch of 100 m. Dashed lines: Gaussian distribution with area and standard deviation equal to that of the measured distribution.

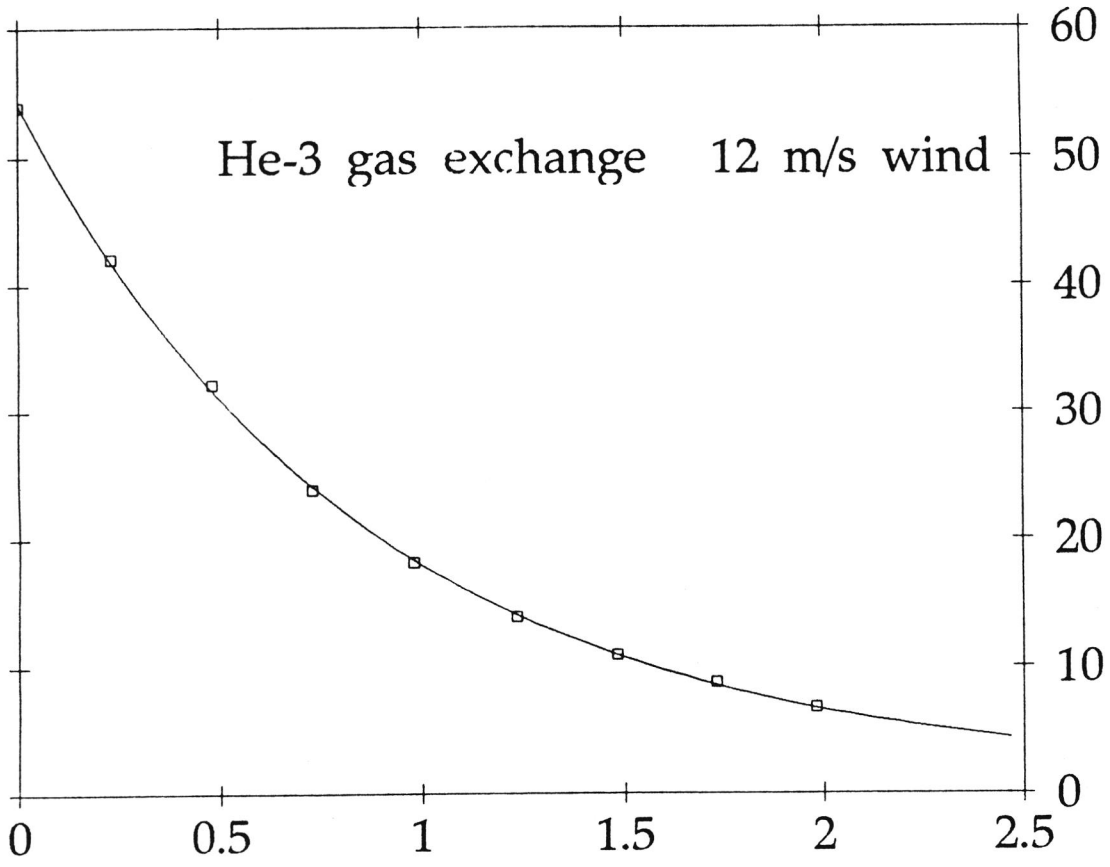

Figure 52: Decrease of the He^3 concentration in water as a function of time. The solid line is a least squares fit to the data, based on an exponential relation.

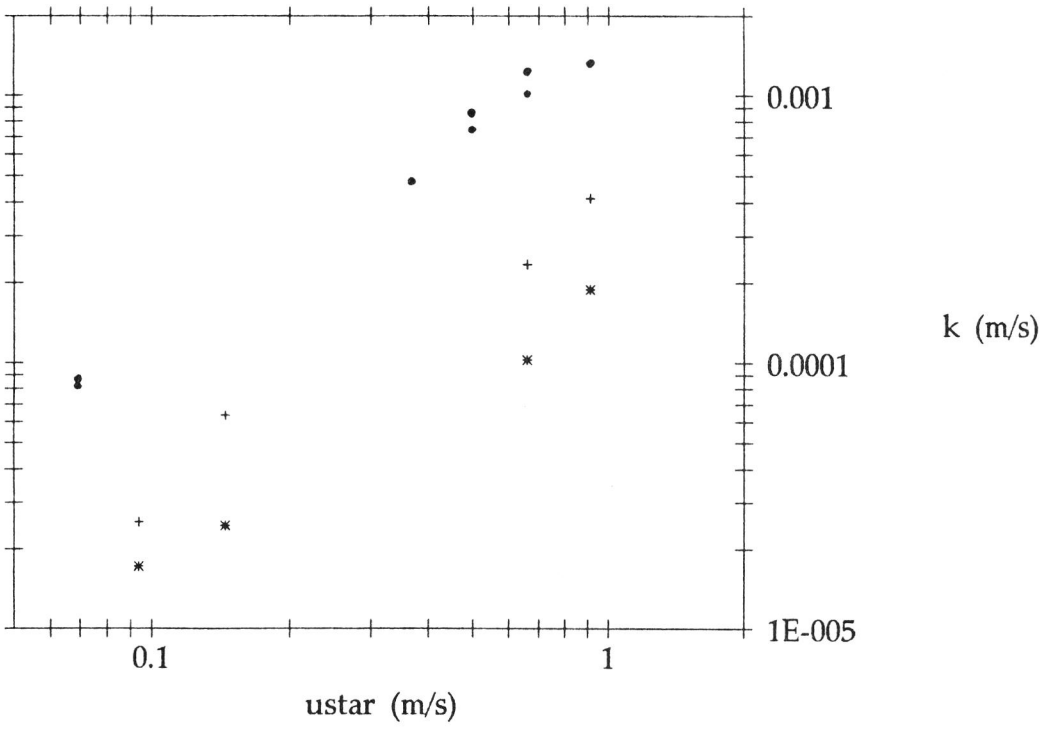

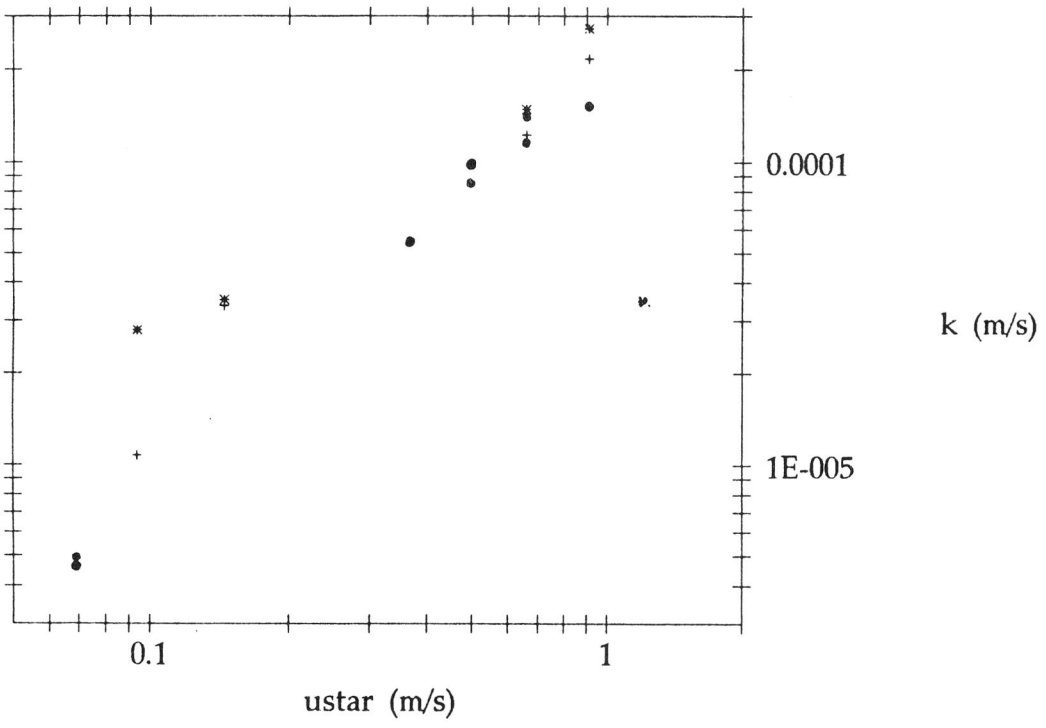

Figure 53: Summary of the measured transfer velocities across the aqueous boundary layer during the November 1987 and February 1988 campaigns in the Delft wind-wave facility. a) Measured transfer velocities; b) transfer velocities extrapoated to a Schmidt number Sc=600. The symbols indicate the tracer: • : heat; + : SF_6; * : He^3.

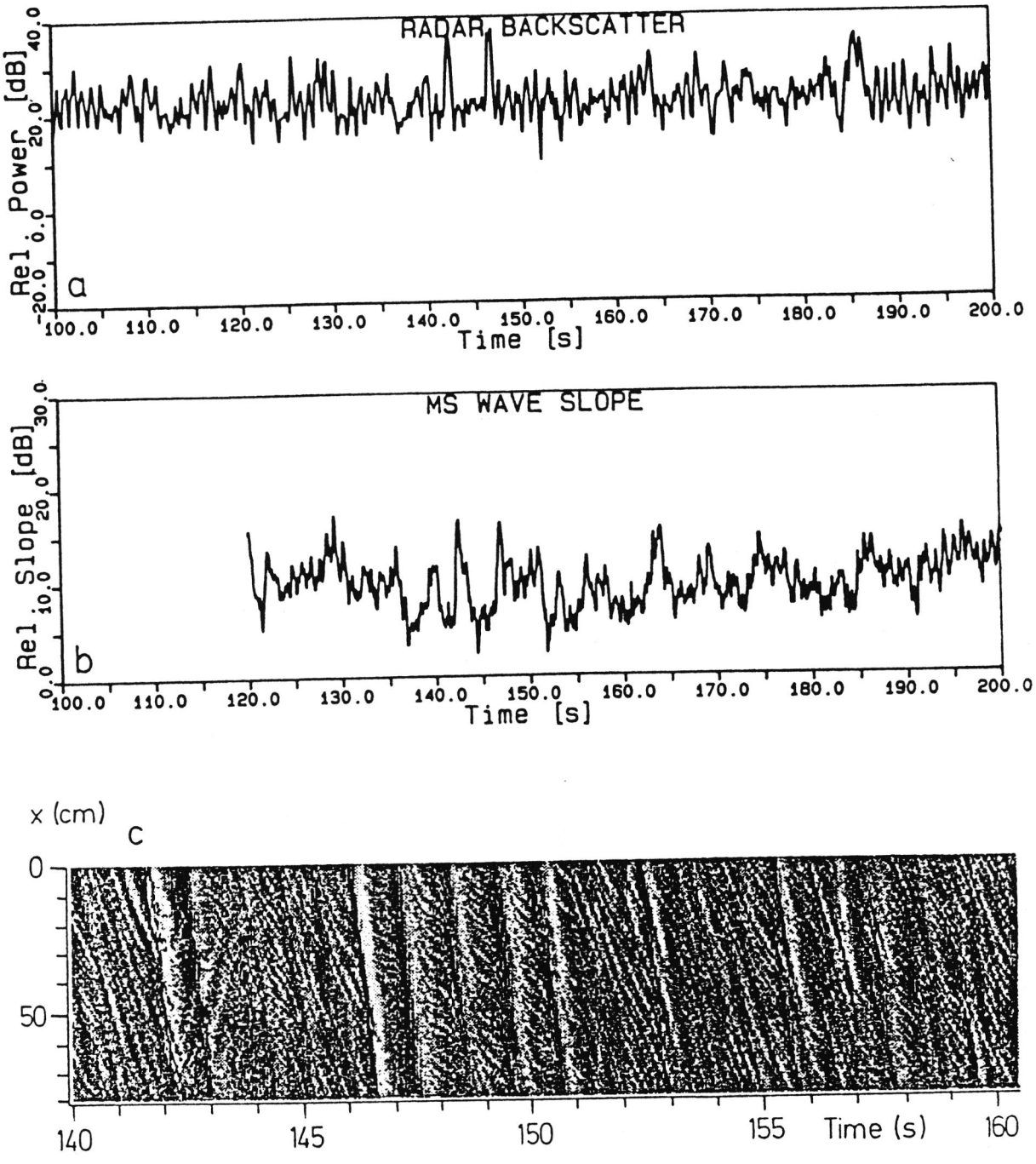

Figure 54: Simultaneous time series of (a) the microwave backscatter at HH polarization and an incidence angle of 45°, looking upwind and (b) the mean square slope, calculated from images, recorded with the ISG. The friction velocity u_* was 37 cm/s (U_{10} = 11.5 m/s). Note the strong modulation of the signals by the long wave (1.1 second period). The two spiky returns at t=142 s and t = 146.5 s are caused by breaking waves. Figure c shows a space time image of the wave slope. A single along wind line in the center of the radar footprint was taken from each picture of the series of two-dimensional ISG images and with these a new image was formed, showing the time history of that line. The wave slope is coded in shades of gray, dark shades indicating downwind directed slopes.

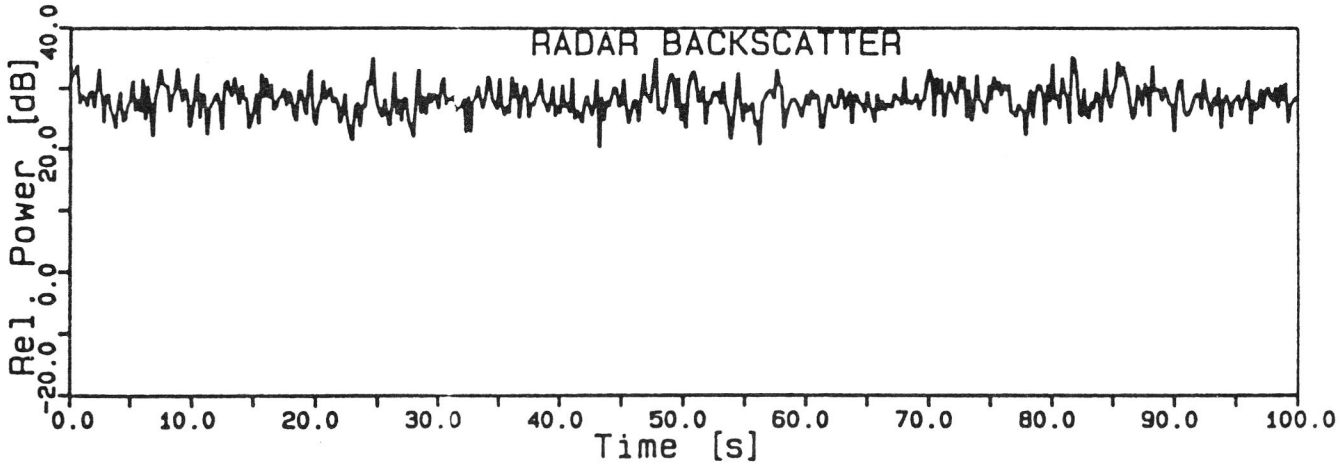

Figure 55: As figure 54a, only at VV polarization. The backscattered signal is much less modulated by the long waves than in the HH case. Relative values only.

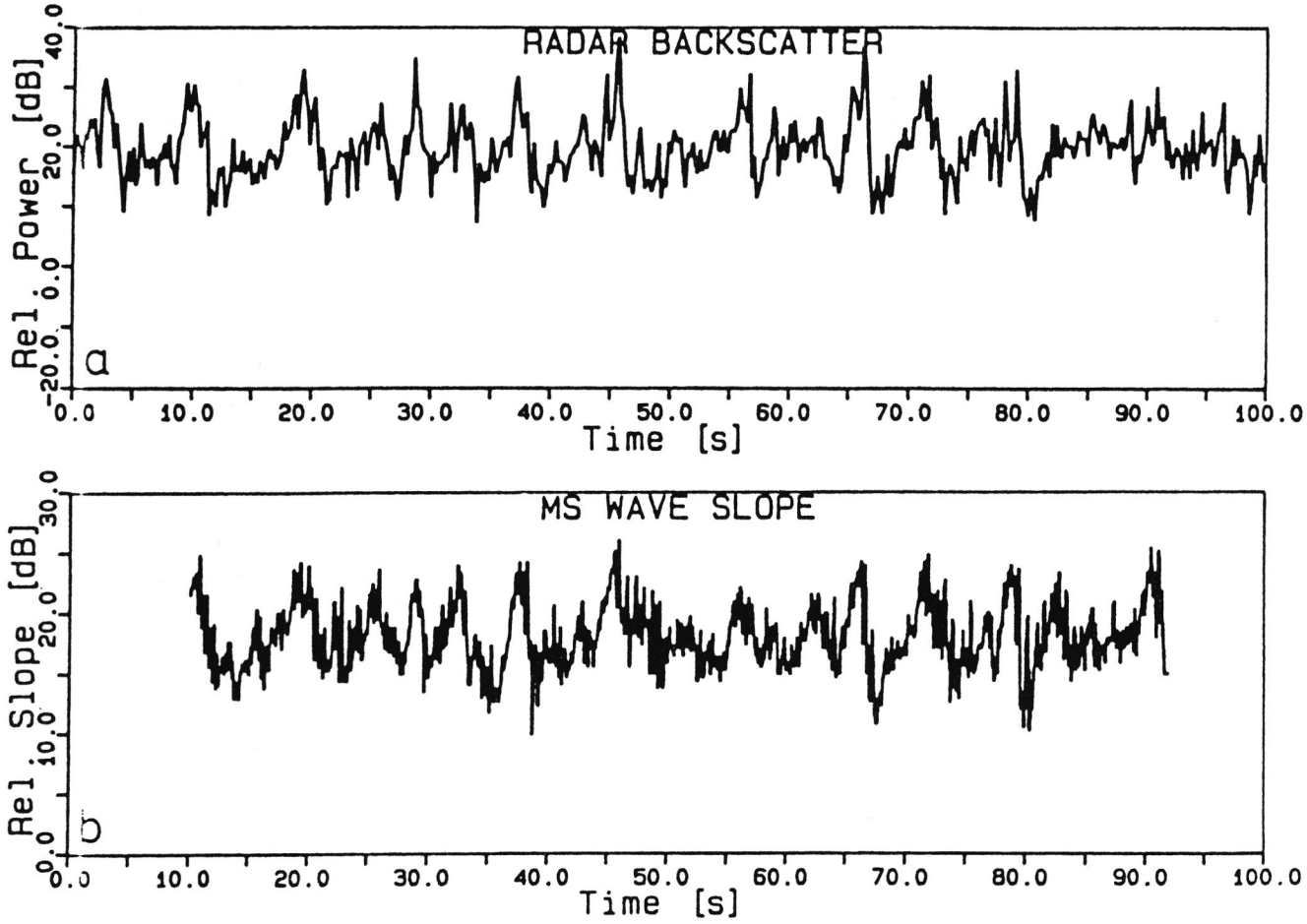

Figure 56: Time recording of the microwave backscatter at 35° incidence angle, looking upwind and with HH polarization (relative values) and the mean square slope as obtained from a single line in the ISG footprint. The friction velocity was 15 cm/s (U_{10} = 5.8 m/s). Note the spiky behaviour of the backscattered signal and the striking correspondence in long term variations of the mean square slope and microwave bbackscatter. The spikes are related to waves, generated immediately after a micro-scale breaking event.

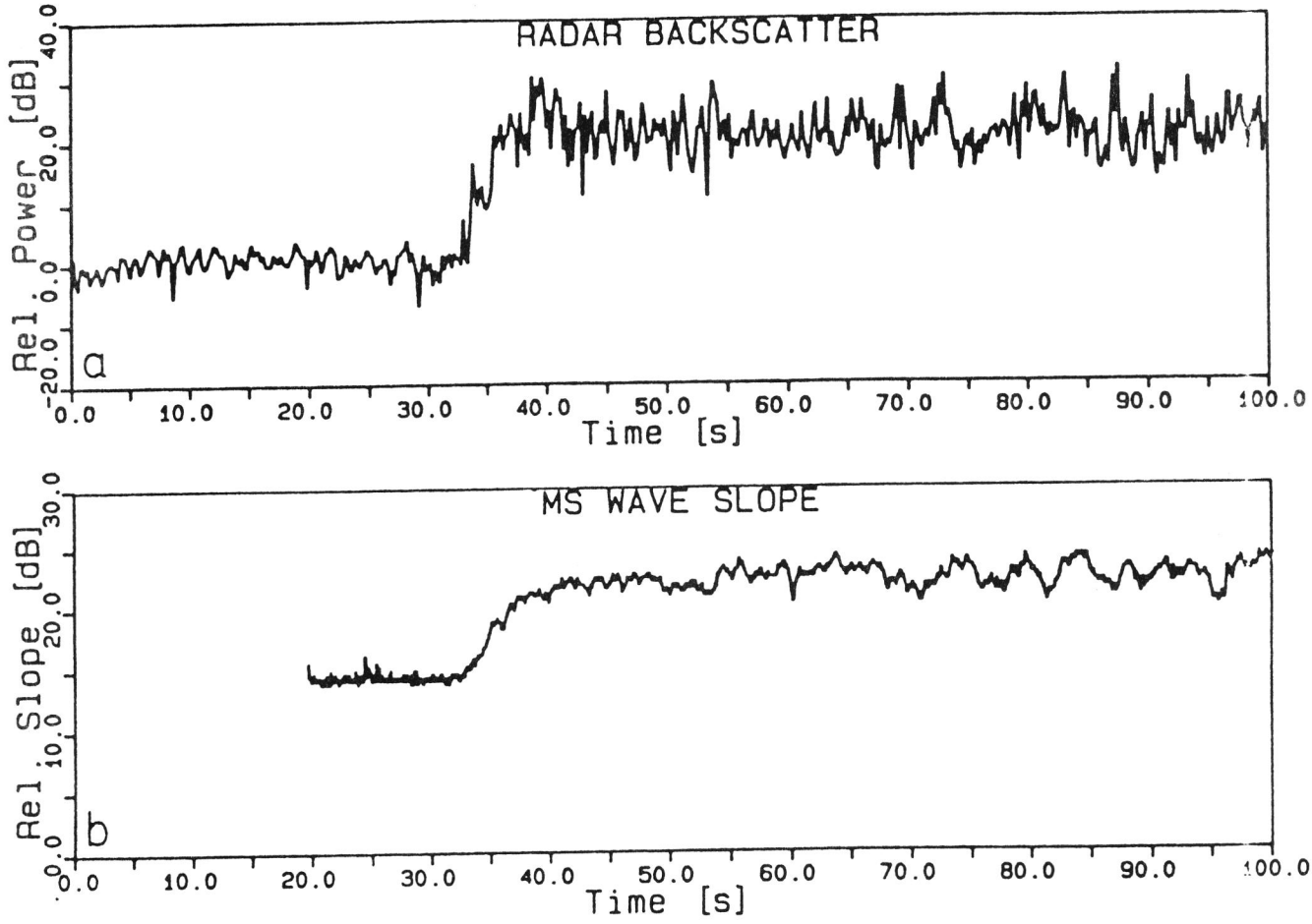

Figure 57: Response of (a) the microwave backscatter and (b) the mean square slope to an increase of wind speed from 0 to 8.6 m/s. The radar functioned at HH polarization and was looking upwind at an incidence angle of 45°.

APPENDIX A

VIERS: combined radar/wind/wave measurements
Delft wind/wave tank.
1987/1988

-No-	Wind				Waves					Radar				Type
								RSG	WAVE	RAD AR	POL	AZIM	INC.	
No.	speed	fetch	CUP	SON	ISG	LSG	RSG							
122	0	100	n	n	n	n	n	n	n	y	hh	90	60	cal.rad.
123	0	100	n	n	n	n	n	n	y	y	vv	90	60	cal.rad.
124	8	100	n	n	y	n	y	n	y	y	hh	0	45	az.prof.
125	8	100	n	n	y	n	y	n	y	y	vv	0	45	az.prof.
126	8	100		n	n	n	n	y	n	n				ISSG
127	8	100	n	n	y	n	y	n	y	y	hh	30	45	az.prof.
128	8	100	n	n	y	n	n	n	y	y	vv	30	45	az.prof.
129	8	100	n	n	y	n	y	n	y	y	hh	45	45	az.prof.
130	8	100	n	n	y	n	y	n	y	y	vv	45	45	az.prof.
131	8	100	n	n	y	n	y	n	y	y	hh	60	45	az.prof.
132	8	100	n	n	y	n	y	n	y	y	vv	60	45	az.prof.
133	8	100	n	n	n	n	n	y	n	n				stereo
134	8	100	n	n	y	n	y	n	y	y	hh	90	45	az.prof.
135	8	100	n	n	y	n	y	n	y	y	vv	90	45	az.prof.
136	8	100	n	n	y	n	y	n	y	y	hh	120	45	az.prof.
137	8	100	n	n	y	n	y	y	y	y	vv	120	45	az.prof.
138	8	100	n	n	y	n	y	n	y	y	hh	135	45	az.prof.
139	8	100	n	n	y	n	y	y	y	y	vv	135	45	az.prof.
140	8	100	n	n	y	n	y	n	y	y	hh	150	45	az.prof.
141	8	100	n	n	y	n	y	n	y	y	vv	150	45	az.prof.
142	8	100	n	n	y	n	y	n	y	y	hh	180	45	az.prof.
143	8	100	n	n	y	n	?	n	y	y	vv	180	45	az.prof.
144	0	100	n	n	n	n	n	n	n	y	hh	90	60	cal.rad.
145	0	100	n	n	n	n	n	n	n	y	vv	90	60	cal.rad.
146	0	100	n	n	y	n	n	n	n	n				cal.ISG.
147	0	100	n	n	y	n	n	n	n	n				cal.ISG.
148	4	100	n	n	y	n	y	y	y	y	hh	45	35	az.prof.
149	4	100	n	n	y	n	y	y	y	y	vv	45	35	az.prof.
150	0	100	n	n	y	n	n	n	n	n				cal.ISG.
151	8	100	n	n	y	n	y	n	y	y	hh	45	35	az.prof.
152	8	100	n	n	y	n	y	n	y	y	vv	45	35	az.prof.
153	8	100	n	n	y	n	y	y	y	y	hh	0	35	az.prof.
154	8	100	n	n	y	n	y	n	y	y	vv	0	35	az.prof.
155	4	100	n	n	y	n	n	n	y	y	hh	0	35	az.prof.
156	4	100	n	n	y	n	n	n	y	y	vv	0	35	az.prof.
157	4	100	n	n	y	n	y	n	y	y	hh	90	35	az.prof.
158	4	100	n	n	y	n	y	n	y	y	vv	90	35	az.prof.
159	8	100	n	n	y	n	n	n	y	y	hh	90	35	az.prof.
160	8	100	n	n	y	n	n	n	y	y	vv	90	35	az.prof.

CUP = cup anemometer array
ISG = Imaging slope gauge
RSG = Reflective slope gauge
Wave= High frequency wave wire
Son = sonic anememeter/press. anemometer
LSG = Laser slope gauge
RSSG = Reflective stereo slope gauge

-No-	Wind				Waves					Radar				Type
								R	W	R		A	I	
			C	S	I	L	R	S	A	D	P	Z	N	
			U	O	S	S	S	S	V	A	O	I	C	
No.	speed	fetch	P	N	G	G	G	G	E	R	L	M	.	
161	4	100	n	n	y	n	n	n	y	n				wind onset
162	4	100	n	n	y	n	n	n	y	y	hh	135	35	az.prof.
163	4	100	n	n	y	n	n	n	y	y	vv	135	35	az.prof.
164	8	100	n	n	y	n	n	n	y	y	hh	135	35	az.prof.
165	8	100	n	n	y	n	n	n	y	y	vv	135	35	az.prof.
166	8	100	n	n	y	n	n	n	y	y	hh	180	35	az.prof.
167	8	100	n	n	y	n	n	n	y	y	vv	180	35	az.prof.
168	4	100	n	n	]	n	n	n	y	y	hh	180	35	az.prof.
169	4	100	n	n	y	n	n	n	y	y	vv	180	35	az.prof.
170	0	100	n	n	n	n	n	n	n	y	hh	90	60	cal.rad.
171	0	100	n	n	n	n	n	n	n	y	vv	90	60	cal.rad.
172	2.1	100	n	n	y	y	y	n	y	y	hh	0	45	wind dep.
173	2.1	100	n	n	y	y	y	y	y	y	vv	0	45	wind dep.
174	3	100	n	n	y	y	y	y	y	y	hh	0	45	wind dep.
175	3	100	n	n	y	y	y	y	y	y	vv	0	45	wind dep.
176	4.1	100	n	n	y	y	y	y	y	y	hh	0	45	wind dep.
177	4	100	n	n	y	y	y	y	y	y	vv	0	45	wind dep.
178	5.3	100	n	n	y	y	y	y	y	y	hh	0	45	wind dep.
179	5.3	100	n	n	y	y	y	y	y	y	vv	0	45	wind dep.
180	0	100	n	n	n	n	n	n	n	y	hh	90	60	cal.rad.
181	0	100	n	n	n	n	n	n	n	y	vv	90	60	cal.rad.
182	0	100	n	n	n	n	n		n	y	hh	90	60	cal.rad.
183			n	n	n	n	n	n	n	y	hh	90	60	cal.rad.
184	0	100	n	n	n	n	n	n	n	y	hh	90	60	cal.rad.
185	0	100	n	n	n	n	n	n	n	y	vv	90	60	cal.rad.
186	0	100		n	n	n	n	n	n	y	hh	90	60	cal.rad.
187	3	100	n	n	n	n	n	n	n	n				cal.IR.
188	7	100	n	n	y	y	y	y	y	y	hh	0	45	wind onset
189	7	100	n	n	y	y	y	n	y	y	vv	0	45	wind dep.
190	7	100	n	n	y	n	n	n	y	y	hh	0	45	wind dep.
191	8	100	n	n	y	y	y	y	y	y	hh	0	45	wind dep.
192	8	100	n	n	y	y	y	n	y	y	vv	0	45	wind dep.
193	8	40	n	n	y	y	y	y	y	y	hh	0	45	wind dep.
194	8	40	n	n	y	y	y	y	y	y	vv	0	45	wind dep.
195	10.5	40	n	n	y	y	y	y	y	y	hh	0	45	wind dep.
196	10.5	40	n	n	y	y	y	n	y	y	vv	0	45	wind dep.
197		40	n	n	n	y	n	n	n	n				IR test
198		40	n	n	n	y	n	n	n	n				IR test
199		40	n	n	n	y	n	n	n	n				IR test
200	12	40	n	n	y	y	y	y	y	y	hh	0	45	wind dep.
201	12	40	n	n	y	y	y	y	y	y	vv	0	45	wind dep.
202	15.5	40	n	n	y	y	y	y	y	y	hh	0	45	wind dep.
203	15.5	40	n	n	y	y	y	y	y	y	vv	0	45	wind dep.
204			n	n	y	y	y	y	n	n				cal.opt.
205			n	n	y	n	n	n	n	n				cal.ISG.
206			n	n	n	n	n	n	n	n				cal IR.
207														cal.IR.
208														cal.IR.

CUP = cup anemometer array
Son = sonic anememeter/press. anemometer
ISG = Imaging slope gauge
LSG = Laser slope gauge
RSG = Reflective slope gauge
RSSG = Reflective stereo slope gauge
Wave= High frequency wave wire

-No-	Wind				Waves					Radar				Type
No.	speed	fetch	CUP	SON	ISG	LSG	RSG	RSSG	WAVE	RADAR	POL	AZIM	INC.	
209														cal.IR.
210														cal.IR.
211														cal.IR.
212														cal.IR.
213														cal.IR.
214														cal IR.
215	0	100	n	n	n	n	n	n	n	y	hh	0	45	cal.rad.
216	0		n	n	n	n	n	n	n	y	vv	90	60	cal.rad.
217	4	40	n	n	y	y			y	n				wind dep.
218	4	40	n	n	y	y	y	y	y	y	hh	0	45	wind dep.
219	4	40	n	n	y	y	y	y	y	y	vv	0	45	wind dep.
220		40	n	n	y	n	n	n	n	n				wind onset
221	8	40	n	n	y	y	y	y	y	n				wind dep.
222	12	40	n	n	y	y	y	y	y	y	hh	0	45	wind dep.
223	12	40	n	n	y	y	y	y	y	y	vv	0	45	wind dep.
224	4	25	n	n	y	y	y	y	y	y	hh	0	45	wind dep.
225	4	25	n	n	y	y	y	y	y	y	vv	0	45	wind dep.
226	8	25	n	n	y	y	y	y	y	y	hh	0	45	wind dep.
227	8	25	n	n	y	y	y	y	y	y	vv	0	45	wind dep.
228	8	25	n	n	n	n	n	n	n	n				IR test
229	12	25	n	n	y	y	y	y	y	y	hh	0	45	wind dep.
230	12	25	n	n	y	y	y	y	y	y	vv	0	45	wind dep.
231	0				y					n				cal.ISG.
232	8	25	n	n	y	y	y	y	y	y	hh	90	45	wind dep.
233	8	25	n	n	y	y	y	y	y	y	vv	0	45	wind dep.
234	12	25	n	n	y	y	y	y	y	y	hh	90	45	wind dep.
235	12	25	n	n	y	y	y	y	y	y	vv	90	45	wind dep.
236	4	25	n	n	y	y	y	y	y	n				wind dep.
237			n	n	y	y	y	y	n	n				cal.opt.
238			n	n	n	n	n	n	n	y	hh	90	60	cal.rad.
239			n	n	n	n	n	n	n	y	vv	90	60	cal.rad.
240	10.5	100	n	n	y	y	y	y	n	n				wind dep.
241	10.5	100	n	n	n	n	n	y	n	n				wind dep.
242	12	100	n	n	y	y	y	y	n	n				wind dep.
243	12	100	n	n	n	y	y	y	n	n				wind dep.
244	15	100	n	n	y	y	y	y	y	y	hh	0	45	wind dep.
245	15	100	n	n	y	y	y	y	y	y	vv	0	45	wind dep.
246		100	n	n	y	y	y	y	y	n				wind dep.
247	0	100	n	n	y	n	n	n	n	n				cal.ISG.
249	10.5	100	n	n	y	n	n	n	y	y	hh	0	45	wind dep.
250	10.5	100	n	n	y	n	n	n	y	y	vv	0	45	wind dep.
251	12	100	n	n	y	n	n	n	y	y	hh	0	45	wind dep.
252	12	100	n	n	y	n	n	n	y	y	vv	0	45	wind dep.
254	0	100	n	n	n	n	n	n	n	y	hh	90	60	cal.rad.
255	0				n	n	n	n	n	y	vv	90	60	cal.rad.
256	0				y	n	n	n	n	n				cal ISG.
257	8	100	n	n	y	n	n	n	y	y	hh	0	60	Inc.prof.
258	8	100	n	n	y	n	n	n	y	y	vv	0	60	Inc.prof.

CUP = cup anemometer array
ISG = Imaging slope gauge
RSG = Reflective slope gauge
Wave= High frequency wave wire
Son = sonic anememeter/press. anemometer
LSG = Laser slope gauge
RSSG = Reflective stereo slope gauge

-No-	Wind				Waves					Radar				Type
								R	W	R		A	I	
			C	S	I	L	R	S	A	A	P	Z	N	
			U	O	S	S	S	S	V	D	O	I	C	
No.	speed	fetch	P	N	G	G	G	G	E	A	L	M	.	
259	8	100	n	n	y	n	n	n	y	y	hh	0	50	Inc.prof.
260	8	100	n	n	y	n	n	n	y	y	vv	0	50	Inc.prof.
261	8	100	n	n	y	n	n	n	y	y	hh	0	45	Inc.prof.
262	8	100	n	n	y	n	n	n	y	y	vv	0	45	Inc.prof.
263	8	100	n	n	y	n	n	n	y	y	hh	0	40	Inc.prof.
264	8	100	n	n	y	n	n	n	y	y	vv	0	40	Inc.prof.
265	8	100	n	n	y	n	n	n	y	y	hh	0	35	Inc.prof.
266	8	100	n	n	y	n	n	n	y	y	vv	0	35	Inc.prof.
267	8	100	n	n	y	n	n	n	y	y	hh	0	30	Inc.prof.
268	8	100	n	n	y	n	n	n	y	y	vv	0	30	Inc.prof.
269	8	100	n	n	y	n	n	n	y	y	hh	0	25	Inc.prof.
270	8	100	n	n	y	n	n	n	y	y	vv	0	25	Inc.prof.
271			n	n	n	n	n	n	n	n				cal.ISG.
272	0	100	n	n	n	n	n	n	n	y	hh	90	60	cal.rad.
273	0	100	n	n	n	n	n	n	n	y	vv	90	60	cal.rad.
274	0		n	n	y	n	n	n	n	n				cal.ISG.
275	8	100	n	n	y	n	n	n	y	y	hh	0	45	az.prof.
276	8	100	n	n	y	n	n	n	y	y	vv	0	45	az.prof.
277	8	100	n	n	y	n	n	n	y	y	hh	10	45	az.prof.
278	8	100	n	n	y	n	n	n	y	y	vv	10	45	az.prof.
279	8	100	n	n	y	n	n	n	y	y	hh	20	45	az.prof.
280	8	100	n	n	y	n	n	n	y	y	vv	20	45	az.prof.
281	8	100	n	n	y	n	n	n	y	y	hh	70	45	az.prof.
282	8	100	n	n	y	n	n	n	y	y	vv	70	45	az.prof.
283	8	100	n	n	y	n	n	n	y	y	hh	80	45	az.prof.
284	8	100	n	n	y	n	n	n	y	y	vv	80	45	az.prof.
285	8	100	n	n	y	n	n	n	y	y	hh	90	45	az.prof.
286	8	100	n	n	y	n	n	n	y	y	vv	90	45	az.prof.
287	8	100	n	n	y	n	n	n	y	y	hh	100	45	az.prof.
288	8	100	n	n	y	n	n	n	y	y	vv	100	45	az.prof.
289	8	100	n	n	y	n	n	n	y	y	hh	110	45	az.prof.
290	8	100	n	n	y	n	n	n	y	y	vv	110	45	az.prof.
291	8	100	n	n	y	n	n	n	y	y	hh	160	45	az.prof.
292	8	100	n	n	y	n	n	n	y	y	vv	160	45	az.prof.
293	8	100	n	n	y	n	n	n	y	y	hh	170	45	az.prof.
294	8	100	n	n	y	n	n	n	y	y	vv	170	45	az.prof.
295	0		n	n	n	n	n	n	n	y	hh	90	60	cal.rad.
296	0		n	n	n	n	n	n	n	y	vv	90	60	cal.rad.
297	4	100	n	n	y	n	n	n	y	y	hh	0	45	gen.waves
298	4	100	n	n	y	n	n	n	y	y	vv	0	45	gen.waves
299	7	100	n	n	y	n	n	n	y	y	hh	0	45	gen.waves
300	8	100	n	n	y	n	n	n	y	y	hh	0	45	gen.waves
301	7	100	n	n	y	n	n	n	y	y	hh	0	35	gen.waves
302	7	100	n	n	y	n	n	n	y	y	hh	0	60	gen.waves
303	8	100	n	n	y	n	n	n	y	y	vv	0	45	gen.waves
304	7	100	n	n	y	n	n	n	y	y	vv	0	45	gen.waves
305	0		n	n	n	n	n	n	n	y	vv	90	60	cal.rad.
306	0		n	n	n	n	n	n	n	y	hh	90	60	cal.rad.

CUP = cup anemometer array
Son = sonic anememeter/press. anemometer
ISG = Imaging slope gauge
LSG = Laser slope gauge
RSG = Reflective slope gauge
RSSG = Reflective stereo slope gauge
Wave= High frequency wave wire

-No-	Wind				Waves					Radar				Type
								R	W	R		A	I	
			C	S	I	L	R	S	A	A	P	Z	N	
			U	O	S	S	S	S	V	D	O	I	C	
No.	speed	fetch	P	N	G	G	G	G	E	A	L	M	.	
307	8	100	n	n	y	n	n	n	y	y	hh	90	60	doppler
308	4	100	n	n	y	n	n	n	y	y	hh	0	45	doppler
309	4	100	n	n	y	n	n	n	y	y	hh	0	35	doppler
310	8	100	n	n	y	n	n	n	y	y	hh	0	35	doppler
311	4	100	n	n	y	n	n	n	y	y	hh	0	45	doppler
312	8	100	n	n	y	n	n	n	y	y	hh	0	45	doppler
313	8	100	n	n	y	n	n	n	y	y	hh	0	35	doppler
314	4	100	n	n	y	n	n	n	y	y	hh	0	35	doppler
315	4	100	n	n	y	n	n	n	y	y	hh	90	35	doppler
316	8	100	n	n	y	n	n	n	y	y	hh	90	35	doppler
317	8	100	n	n	y	n	n	n	y	y	hh	90	45	doppler
318	4	100	n	n	y	n	n	n	y	y	hh	0	45	doppler
319	0		n	n	n	n	n	n	n	y	hh	90	60	cal.rad.
320	0		n	n	y	n	n	n	n	y	vv	90	60	cal.ISG.
321	4	100	n	n	y	n	n	n	n	y	vv	90	60	doppler
322	8	100	n	n	y	n	n	n	n	y	vv	90	60	doppler
323	8	100	n	n	y	n	n	n	n	y	vv	180	60	doppler
324	4	100	n	n	y	n	n	n	n	y	vv	180	60	doppler
325	4	100	n	n	y	n	n	n	n	y	vv	90	60	doppler
326	4	100	n	n	y	n	n	n	n	y	vv	90	45	doppler
327	8	100	n	n	y	n	n	n	n	y	vv	0	45	doppler
328	0		n	n	n	n	n	n	y	n		0	45	nul
329	4	100	n	n	n	n	n	n	y	n		0	45	wind
330	8	100	n	n	n	n	n	n	y	n		0	45	wind
331	12	100	n	n	n	n	n	n	y	n		0	45	wind
332	4	100	n	n	n	n	n	n	y	n		0	45	wind
333	4	100	n	n	n	n	n	n	y	n		0	45	wind
334	8	100	n	n	n	n	n	n	y	n		0	45	wind
335	12	100	n	n	n	n	n	n	y	n		0	45	wind
336	4	100	n	n	n	n	n	n	y	n		0	45	wind
337	8	100	n	n	n	n	n	n	y	n		0	45	wind
338	12	100	n	n	n	n	n	n	y	n		0	45	wind
339	4	100	n	n	n	n	n	n	y	n		0	45	wind
340	8	100	n	n	n	n	n	n	y	n		0	45	wind
341	4	100	n	n	n	n	n	n	y	n		0	45	wind
342	8	100	n	n	n	n	n	n	y	n		0	45	wind
343	0		n	n	n	n	n	n	y	n				nul
344	0	100	n	n	n	n	n	n	y	n				nul
345	8	100	n	n	n	n	n	n	y	n				wind
346	4	100	n	n	n	n	n	n	y	n				wind
347	12	100	n	n	n	n	n	n	y	n				wind
348	12	100	n	n	n	n	n	n	y	n				wind
349	4	100	n	n	n	n	n	n	y	n				wind
350	8	40	n	n	n	n	n	n	y	n				wind
351	12	40	n	n	n	n	n	n	y	n				wind
352	12	40	n	n	n	n	n	n	y	n				wind
353	8	40	n	n	n	n	n	n	y	n				wind
354	4	40	n	n	n	n	n	n	y	n				wind

CUP = cup anemometer array
Son = sonic anememeter/press. anemometer
ISG = Imaging slope gauge
LSG = Laser slope gauge
RSG = Reflective slope gauge
RSSG = Reflective stereo slope gauge
Wave= High frequency wave wire

-No-	Wind				Waves					Radar				Type
								RSS	WAV	RAD	POL	AZIM	INC.	
No.	speed	fetch	CUP	SON	ISG	LSG	RSG	G	E	AR	L	M	.	
355	0	40	n	n	n	n	n	n	y	n				nul
356	0	40	n	n	n	n	n	n	y	n				nul
357	4	40	n	n	n	n	n	n	y	n				wind
358	8	40	n	n	n	n	n	n	y	n				wind
359	12	40	n	n	n	n	n	n	y	n				wind
360	4	40	n	n	n	n	n	n	y	n				wind
361	8	40	n	n	n	n	n	n	y	n				wind
362	12	40	n	n	n	n	n	n	y	n				wind
363	4	40	n	n	n	n	n	n	y	n				wind
364	8	40	n	n	n	n	n	n	y	n				wind
365	12	40	n	n	n	n	n	n	y	n				wind
366	0	25	n	n	n	n	n	n	y	n				nul
367	4	25	n	n	n	n	n	n	y	n				wind
368	8	25	n	n	n	n	n	n	y	n				wind
369	12	25	n	n	n	n	n	n	y	n				wind
370	4	25	n	n	n	n	n	n	y	n				wind
371	8	25	n	n	n	n	n	n	y	n				wind
372	12	25	n	n	n	n	n	n	y	n				wind
373	4	25	n	n	n	n	n	n	y	n				wind
374	8	25	n	n	n	n	n	n	y	n				wind
375	12	25	n	n	n	n	n	n	y	n				wind
376	0	25	n	n	n	n	n	n	y	n				nul
377	0	25	n	n	n	n	n	n	y	n				nul
378	4	25	n	n	n	n	n	n	y	n				wind
379	8	25	n	n	n	n	n	n	y	n				wind
380	12	25	n	n	n	n	n	n	y	n				wind
381	4	25	n	n	n	n	n	n	y	n				wind
382	8	25	n	n	n	n	n	n	y	n				wind
383	12	25	n	n	n	n	n	n	y	n				wind
384	0	25	n	n	n	n	n	n	y	n				nul

CUP = cup anemometer array
Son = sonic anememeter/press. anemometer
ISG = Imaging slope gauge
LSG = Laser slope gauge
RSG = Reflective slope gauge
RSSG = Reflective stereo slope gauge
Wave= High frequency wave wire

Appendix B: Calibration figures for the cup-anemometers.

anemometer nr.	threshold velocity (m/s)	coefficient a (m/V.s)	coefficient b (m/s)	residual error (m/s)
1	1.07	4.1825	-0.3362	0.2138
2	1.00	4.1455	-0.3665	0.1723
3	0.63	4.1591	-0.3498	0.1992
4	1.00	4.1494	-0.3225	0.2039
5	0.89	4.1870	-0.4015	0.1643
6	1.60	4.1498	-0.1610	0.3287
7	1.83	4.1098	-0.1673	0.2730

APPENDIX C: RESULTS OF THE PRESSURE ANEMOMETER.

Run nr	POSITION (Fig.3)	FETCH (m)	RADAR (table)	U10 m/s	U* m/s	DU* m/s	Z0 mm	DZ0 mm	CD10 *1000	DCD10 *1000
2	6	50	0	16.203	0.589	0.024	0.172	0.052	1.32	0.08
3	6	50	0	11.3	0.358	0.008	0.034	0.007	1.01	0.03
4	6	50	0	5.724	0.154	0.008	0.004	0.002	0.72	0.05
5	6	75	0	5.807	0.152	0.008	0.003	0.002	0.68	0.06
6	6	75	0	11.564	0.374	0.021	0.048	0.023	1.05	0.09
7	6	75	0	16.595	0.618	0.032	0.228	0.09	1.39	0.1
10	6	100	0	6.022	0.139	0.01	0	0	0.53	0.05
11	6	100	0	11.951	0.375	0.029	0.036	0.026	0.99	0.12
23	7	75	0	5.482	0.144	0.011	0.003	0.002	0.69	0.08
25	7	75	0	5.411	0.136	0.009	0.002	0.001	0.63	0.07
26	7	75	0	5.363	0.13	0.007	0.001	0.001	0.59	0.06
27	7	75	0	11.445	0.361	0.022	0.036	0.018	1	0.09
28	7	75	0	16.85	0.658	0.028	0.368	0.105	1.53	0.08
29	5	75	0	5.636	0.133	0.007	0.001	0	0.55	0.05
30	5	75	0	11.473	0.372	0.02	0.048	0.021	1.05	0.08
31	5	75	0	17.164	0.679	0.028	0.418	0.124	1.57	0.09
32	11	75	0	5.66	0.145	0.005	0.002	0.001	0.66	0.04
33	11	75	0	11.28	0.354	0.018	0.032	0.017	0.98	0.08
34	11	75	0	17.109	0.666	0.021	0.353	0.078	1.52	0.07
37	9	75	0	5.768	0.148	0.007	0.002	0.001	0.66	0.05
38	9	75	0	12.808	0.441	0.014	0.093	0.027	1.19	0.06
39	9	75	0	17.193	0.706	0.036	0.617	0.26	1.69	0.12
42	8	100	0	1.899	0.058	0.005	0.028	0.02	0.95	0.12
43	8	100	0	2.641	0.069	0.01	0.006	0.008	0.69	0.15
44	8	100	0	3.156	0.086	0.006	0.005	0.004	0.74	0.08
45	8	100	0	3.893	0.103	0.006	0.027	0.011	0.7	0.06
46	8	100	0	5.172	0.14	0.01	0.005	0.005	0.74	0.08
47	8	100	0	6.582	0.183	0.009	0.006	0.003	0.78	0.06
48	8	100	0	8.524	0.246	0.021	0.013	0.011	0.84	0.11
49	8	100	0	10.964	0.367	0.015	0.069	0.024	1.12	0.07
50	8	100	0	13.449	0.49	0.024	0.178	0.059	1.33	0.09
51	8	100	0	16.194	0.66	0.023	0.559	0.136	1.66	0.08
59	8	100	0	6.814	0.195	0.01	0.01	0.006	0.82	0.07
60	8	100	0	8.744	0.259	0.018	0.016	0.009	0.88	0.09
62	8	100	0	13.639	0.503	0.018	0.203	0.063	1.36	0.07
64	8	100	7	2.921	0.086	0.006	0.015	0.01	0.87	0.09
65	8	100	7	5.102	0.139	0.009	0.005	0.003	0.74	0.06
68	6	100	1	5.322	0.143	0.006	0.004	0.002	0.73	0.05
69	6	100	1	10.865	0.351	0.016	0.045	0.02	1.04	0.07
70	6	100	2	5.562	0.148	0.008	0.003	0.002	0.71	0.06
71	6	100	2	10.918	0.338	0.014	0.026	0.014	0.96	0.06
72	6	100	3	5.339	0.139	0.011	0.003	0.002	0.68	0.08
73	6	100	3	11.041	0.343	0.014	0.028	0.013	0.97	0.07
76	6	100	0	5.388	0.143	0.008	0.003	0.002	0.71	0.06
77	6	100	0	11.071	0.343	0.017	0.027	0.015	0.96	0.07
78	6	100	4	5.479	0.147	0.008	0.004	0.003	0.72	0.07
79	6	100	4	11.109	0.355	0.016	0.04	0.015	1.02	0.07
82	6	100	5	5.419	0.147	0.004	0.004	0.001	0.74	0.03
83	6	100	5	10.982	0.346	0.016	0.034	0.015	1	0.07
85	7	100	1	5.083	0.15	0.008	0.014	0.007	0.87	0.07
86	7	100	1	10.688	0.35	0.015	0.053	0.02	1.07	0.08
89	5	100	1	5.472	0.148	0.006	0.004	0.002	0.73	0.05
90	5	100	1	10.749	0.331	0.017	0.025	0.012	0.95	0.08

Run nr	POSITION (Fig.3)	FETCH (m)	RADAR (table)	U10 m/s	U* m/s	DU* m/s	Z0 mm	DZ0 mm	CD10 *1000	DCD10 *1000
91	11	100	1	5.16	0.121	0.007	0	0	0.55	0.05
92	11	100	1	10.807	0.34	0.02	0.034	0.019	0.99	0.09
93	9	100	1	5.042	0.13	0.007	0.002	0.001	0.66	0.06
94	9	100	1	10.567	0.334	0.012	0.034	0.009	1	0.05
329	6	100	6	5.794	0.172	0.015	0.02	0.017	0.89	0.12
330	6	100	6	11.771	0.384	0.017	0.05	0.018	1.06	0.07
331	6	100	6	17.949	0.684	0.037	0.295	0.134	1.45	0.12
332	7	100	6	5.761	0.165	0.011	0.011	0.008	0.83	0.09
333	7	100	6	5.799	0.172	0.006	0.015	0.005	0.88	0.05
334	7	100	6	11.96	0.363	0.022	0.022	0.016	0.92	0.09
335	7	100	6	18.113	0.688	0.036	0.282	0.103	1.44	0.11
336	5	100	6	6.244	0.166	0.009	0.004	0.002	0.71	0.06
337	5	100	6	12.237	0.354	0.025	0.012	0.011	0.84	0.09
338	5	100	6	18.695	0.684	0.05	0.201	0.11	1.34	0.14
339	11	100	6	6.314	0.163	0.011	0.002	0.001	0.66	0.07
340	11	100	6	12.232	0.367	0.021	0.018	0.009	0.9	0.08
341	9	100	6	6.467	0.167	0.009	0.002	0.001	0.66	0.05
342	9	100	6	12.463	0.378	0.02	0.02	0.01	0.92	0.07
345	5	100	0	12.041	0.364	0.013	0.019	0.006	0.91	0.05
346	5	100	0	6.07	0.14	0.004	0	0	0.53	0.03
347	5	100	0	17.968	0.683	0.02	0.272	0.046	1.45	0.05
348	11	100	0	17.366	0.64	0.016	0.195	0.032	1.36	0.04
349	11	40	0	5.854	0.156	0.003	0.003	0.001	0.71	0.02
350	11	40	0	11.04	0.351	0.017	0.037	0.015	1.01	0.07
351	11	40	0	16.511	0.642	0.006	0.341	0.024	1.51	0.02
352	6	40	0	17.079	0.622	0.029	0.179	0.067	1.33	0.08
353	6	40	0	11.235	0.337	0.012	0.017	0.006	0.9	0.05
354	6	40	0	5.735	0.165	0.019	0.013	0.009	0.83	0.13
357	7	40	0	5.427	0.156	0.009	0.01	0.005	0.83	0.06
358	7	40	0	10.851	0.328	0.016	0.02	0.009	0.92	0.07
359	7	40	0	16.534	0.601	0.03	0.174	0.061	1.32	0.09
360	9	40	0	5.346	0.144	0.011	0.005	0.004	0.73	0.09
361	9	40	0	10.79	0.327	0.018	0.021	0.012	0.92	0.08
362	9	40	0	16.331	0.601	0.027	0.198	0.066	1.36	0.08
363	5	40	0	5.247	0.151	0.008	0.01	0.004	0.83	0.06
364	5	40	0	10.801	0.321	0.022	0.017	0.013	0.88	0.09
365	5	40	0	16.385	0.557	0.019	0.079	0.02	1.15	0.06
367	5	25	0	5.372	0.177	0.009	0.059	0.026	1.09	0.09
368	5	25	0	11.011	0.363	0.011	0.055	0.013	1.09	0.05
369	5	25	0	16.288	0.576	0.029	0.129	0.043	1.25	0.09
370	6	25	0	5.282	0.175	0.01	0.06	0.027	1.09	0.08
371	6	25	0	10.376	0.358	0.006	0.062	0.008	1.11	0.02
372	6	25	0	16.095	0.576	0.034	0.157	0.081	1.28	0.13
373	7	25	0	5.076	0.163	0.004	0.039	0.008	1.03	0.03
374	7	25	0	10.546	0.346	0.017	0.055	0.021	1.08	0.08
375	7	25	0	15.976	0.582	0.021	0.175	0.051	1.33	0.07
378	11	25	0	5.324	0.153	0.004	0.009	0.002	0.83	0.03
379	11	25	0	10.436	0.329	0.015	0.034	0.013	1	0.07
380	11	25	0	15.475	0.563	0.017	0.172	0.035	1.33	0.05
381	9	25	0	5.299	0.162	0.01	0.025	0.015	0.94	0.09
382	9	25	0	10.751	0.347	0.016	0.044	0.02	1.04	0.07
383	9	25	0	16.331	0.607	0.019	0.218	0.06	1.38	0.07

APPENDIX D: COEFFICIENTS FOR THE CALCULATION OF $C_{d,10}$, Z_0 AND U_{10} FOR A GIVEN VALUE OF U_{10}.

COEFFICIENTS QUADRATIC FIT
(Y=(A U + B) U + C, WITH Y IS CD10, Z0 OR U*)

	DRAGCOEFFICIENT (CD10)					ROUGHNESS LENGTH (z0)					FRICTION VELOCITY (u*)				
	POS. 5	POS 6.	POS .7	POS. 9	POS. 11	POS. 5	POS. 6	POS. 7	POS. 9	POS. 11	POS. 5	POS. 6	POS. 7	POS. 9	POS. 11
FETCH = 25 M, NO RADAR															
A=	0.002778	0.002386	0.003385	0.003861	0.003175	0.015940	0.014429	0.013790	0.016598	0.006080	0.000676	0.000203	0.000918	0.00115	0.001183
B=	-0.04551	-0.03343	-0.04374	-0.04362	-0.01679	-0.27359	-0.21950	-0.15258	-0.16270	0.164188	0.021910	0.032748	0.019113	0.01551	0.015784
C=	1.254298	1.200026	1.164822	1.062742	0.829383	-1.82050	-2.05660	-2.82500	-3.29278	-5.75700	0.039793	-0.00363	0.042327	0.04758	0.035432
FETCH = 40 M, NO RADAR															
A=	0.003533	0.005364	0.004843	0.004052	0.003148	0.016123	0.031211	0.022767	0.012865	-0.00736	0.001046	0.001542	0.001470	0.00144	0.001463
B=	-0.04769	-0.07830	-0.06224	-0.03048	0.004674	-0.16320	-0.48088	-0.24281	0.056012	0.608863	0.013816	0.005101	0.007783	0.01036	0.012890
C=	0.982986	1.102645	1.025153	0.777132	0.574775	-4.19275	-2.61151	-3.95799	-5.96545	-9.12103	0.049701	0.085022	0.070470	0.04744	0.030416
FETCH = 100 M, WITH RADAR															
A=	0.004476	0.002854	0.006065	8.24E-18	0	0.020328	0.011024	0.026712	-0.06158	-0.05834	0.001585	0.001077	0.001737	-0.0001	4.29E-18
B=	-0.06103	-0.02168	-0.09789	0.043362	0.040554	-0.19237	-0.04034	-0.38875	1.549675	1.453293	0.002085	0.016553	0.000569	0.03624	0.034471
C=	0.916561	0.919820	1.223168	0.379576	0.403941	-5.11287	-4.04840	-2.98825	-13.6611	-13.0648	0.091200	0.039939	0.107666	-0.0651	-0.05465
FETCH = 100 M, WITH RADAR															
A=						0.002243	0.002850	0.003308	1.29E-19	-1.3E-19					
B=						-0.04012	-0.04504	-0.05723	0.003002	0.002704					
C=						0.167069	0.185269	0.233271	-0.01741	-0.01507					

z_0: uitkomst in $\ln(z_0)$ in mm